Non-equilibrium Dynamics in Coupled Bilayer Two-dimensional Bose Gases

En Chang

Christ Church College

University of Oxford

A thesis submitted for the degree of

Doctor of Philosophy

Michaelmas 2025

Acknowledgements

Firstly, I would like to express my sincere gratitude to my supervisor Professor Christopher Foot, for offering me the opportunity to work in the ultracold quantum matter group, for his patient guidance and support over the past four years, and for providing me with the freedom to pursue my research interests.

I feel truly fortunate to have worked with such talented and supportive members of the group. I am deeply grateful to Dr Shinichi Sunami for his patient guidance in helping me understand the experiments and theories of 2D systems. His keen physical intuition and insightful feedback have been of great benefit to my research. I would also like to express my sincere thanks to Dr Abel Beregi for his generous help with the experimental work and for the stimulating discussions on numerical simulations that followed, from which I always learned new techniques. It has been a great pleasure to work with Erik Rydow. With our shared background in theoretical physics, we frequently discussed theoretical problems, and his solid grasp of physics and mathematics has been a constant source of inspiration. In my final year, I also received great support from the new group members, Yao-Chih Kuo and Ziyue Jin. I am confident that they will continue to drive the experiments forward with success. I would also like to thank my theory collaborators, Dr. Vijay Singh in the UAE and Professor Ludwig Mathey in Germany, for the inspiring and productive discussions on coupling-quench physics. I am thankful to the other group members: Dr Elliot Bentine, Dr Kenneth Hughes, Dr Timothy Leese, Jesse Schelfhout and Dr Charu Mishra.

Outside the lab and physics, I would like to thank my friends Dr Kaitao Tang, Dr Jiangrui Qian and Dr Yinxuan Huang for making my life in Oxford enjoyable and fulfilling. Huge thanks to my parents, Wei Chang and Weiping Tang, for their continuous encouragement and support throughout these years. I also thank my parents-in-law, Guowei Qi and Guihua Wang. Last but by no means least, I would like to express my deepest gratitude to my wife, Jiami Qi, for her enduring support, understanding, and companionship, even during the two years we spent apart in different time zones.

Abstract

Non-equilibrium (NEQ) many-body dynamics are ubiquitous, ranging from glassy systems to the emergence of structure in the early universe. Ultracold atomic gases provide an ideal, highly controllable platform for studying these phenomena, and this thesis presents a comprehensive investigation into the NEQ dynamics of coupled bilayer two-dimensional (2D) Bose gases.

In this thesis, we numerically investigate Josephson effects in bilayer 2D superfluids using classical-field simulations. We show that the system exhibits damped Josephson oscillations and macroscopic quantum self-trapping, and we discuss the associated excitations that emerge in the system. We then experimentally study the phase-ordering dynamics following a coupling quench that drives the system from a disordered to an ordered phase, realized using a well-controlled multiple-radio-frequency (MRF) dressed double-well potential. The resulting NEQ dynamics are probed using matter-wave interferometry, which provides direct access to correlation functions and vortex excitations of the relative-phase mode. Our results demonstrate that the system undergoes universal dynamics in the form of diffusion-type coarsening, in excellent agreement with classical-field numerical simulations.

This work broadens the understanding of NEQ and universal dynamics, and the methods presented here serve as a novel and highly tunable approach for exploring a wide range of NEQ dynamics.

Publications

The following publications include work to which I contributed during my DPhil research:

- **E. Chang**, V. P. Singh, A. Beregi, E. Rydow, L. Mathey, C. J. Foot, S. Sunami, "*Coupling-induced universal dynamics in bilayer two-dimensional Bose gases*", arXiv:2510.23600 (2025)
- A. Beregi, **E. Chang**, E. Rydow, C. J. Foot, S. Sunami, "*Universal non-Gaussian order parameter statistics in 2D superfluids*", arXiv:2601.16204 (2026)
- M. Sesodia, S. Sunami, **E. Chang**, E. Rydow, C. J. Foot, A. Beregi, "*CNN-Based vortex detection in atomic 2D Bose gases in the presence of a phononic background*", Machine Learning: Science and Technology **6**, 015067 (2025)
- E. Rydow, V. P. Singh, A. Beregi, **E. Chang**, L. Mathey, C. J. Foot, S. Sunami, "*Observation of a bilayer superfluid with interlayer coherence*", Nature Communications **16**, 7201 (2025)
- S. Sunami, V. P. Singh, E. Rydow, A. Beregi, **E. Chang**, L. Mathey, C. J. Foot, "*Detecting Phase Coherence of 2D Bose Gases via Noise Correlations*", Physical Review Letters **134**, 183407 (2025)

Contents

List of Figures

1 Introduction

The study of quantum many-body systems far from thermal equilibrium represents one of the most vibrant and challenging frontiers in modern physics, our understanding of the dynamical evolution of complex interacting systems remains far less complete. Ultracold atomic gases have emerged as a promising platform for exploring these dynamics, offering remarkable control over system parameters such as dimensionality, interaction strength, and external potentials. This allows for the precise engineering of Hamiltonians and the direct observation of their subsequent time evolution, effectively positioning these systems as "quantum simulators".

Within this landscape, systems confined to two spatial dimensions (2D) hold a special significance. The Mermin-Wagner theorem dictates that continuous symmetries cannot be spontaneously broken at finite temperatures in 2D systems with short-range interactions, precluding conventional long-range order [1]. Instead, 2D systems can exhibit a more subtle form of order, characterized by a topological phase transition first described by Berezinskii, Kosterlitz, and Thouless (BKT) [2, 3]. This transition is mediated by the binding and unbinding of vortex-antivortex pairs. Below the BKT transition temperature, the gas enters a superfluid phase characterized by quasi-long-range order and a power-law decay of correlations, while above it, a proliferation of free vortices destroys this order. The unique nature

of the 2D system and its associated topological defects provides a rich backdrop for investigating non-equilibrium phenomena.

The complexity and richness of 2D systems can be further enhanced by introducing an additional degree of freedom, such as a coupling between two parallel layers. Coupled bilayer 2D Bose gases are paradigmatic systems for studying a variety of quantum phenomena, including Josephson effects [4–8], light-cone dynamics [9], reverse-KZ mechanism [9, 10], and universal rephasing [11]. In equilirbium, the interplay between the intralayer BKT physics and the interlayer Josephson coupling gives rise to a complex phase diagram [12–14].

This thesis explores two key aspects of the dynamics in a coupled bilayer system. First, we investigate the rich phenomenology of Josephson effects that arise from interlayer coupling, focusing on the role of topological excitations and sine–Gordon solitons unique to 2D systems. We then turn to phase-ordering dynamics, examining the system's evolution following a quantum quench implemented via a sudden change in the tunnel-coupling strength. Such a coupling quench explicitly breaks symmetry and drives the system far from equilibrium, forcing it to evolve toward a new steady state. Of particular interest among universal non-equilibrium (NEQ) phenomena are the coarsening dynamics that manifest as a power-law growth of a characteristic coherence length, $L(t) \sim t^{1/z}$, following a quench from a disordered to an ordered phase, characterized by a universal dynamical exponent z [15–20]. This motivates a central question of broad relevance to NEQ physics: can universal coarsening dynamics arise following an explicitly symmetry-breaking quench, and if so, what dynamic exponent governs this behavior in a coupled bilayer system?

To answer these questions, we probe the system's dynamics through a combination of numerical and experimental approaches. We perform numerical investigations by employing the classical-field methods based on Monte Carlo simulations and the Gross–Pitaevskii equation (GPE), which have proven highly effective in describing the dynamics of weakly interacting Bose gases at finite temperature [10, 21–23]. These simulations allow us to directly follow the evolution of correlation functions, the density of topological defects, and the growth of order, thereby enabling a

direct test of the scaling hypothesis and the extraction of critical exponents. At the same time, significant progress in experimental methods for ultracold atomic gases, such as multiple-radiofrequency (MRF) dressed potentials, time-of-flight (TOF) imaging, and matter-wave interferometry, has enabled powerful approaches to studying non-equilibrium dynamics and provided quantitative data for comparison with theoretical predictions.

The remainder of this thesis is organized as follows. Chapter 2 introduces the theoretical framework for describing the coupled bilayer 2D Bose gas, including the model Hamiltonian and the equilibrium phase diagram. Chapter 3 presents the numerical methods used to simulate the system both in and out of equilibrium and reports the numerical investigation of Josephson effects in 2D bilayers. Chapter 4 describes the experimental apparatus employed to realize the tunnel-coupled quasi-2D bilayer gas. Chapter 5 presents the main experimental results on the quench dynamics and phase-ordering kinetics. Finally, Chapter 6 concludes with a summary of the findings and an outlook for future experimental research directions.

2

Theory of Bilayer 2D Bose Gases

Contents

In this chapter, we review the theoretical framework for bilayer weakly interacting two-dimensional (2D) Bose gases. We begin with the 2D XY model, which serves as a low-temperature effective theory for a single-layer 2D Bose gas and for decoupled bilayers. The model is then extended to the coupled XY case, where the system naturally decomposes into symmetric and antisymmetric sectors with distinct

physical behaviour. Finally, we examine bilayer 2D Bose gases and show that interactions suppress density fluctuations, while tunnel coupling gives rise to novel phases beyond the Berezinskii–Kosterlitz–Thouless transition.

2.1 2D XY Model

2.1.1 Spin correlation functions

We consider classical planar spins of unit length, $\mathbf{S}_i = (\cos\theta_i, \sin\theta_i)$, sitting on the sites i of a regular two dimension (2D) square lattice. Only nearest neighbours interact, with ferromagnetic exchange $J > 0$:

$$H_{\mathrm{XY}} = -J \sum_{\langle i,j \rangle} \mathbf{S}_i \cdot \mathbf{S}_j = -J \sum_{\langle i,j \rangle} \cos(\theta_i - \theta_j) \ . \tag{2.1}$$

The Hamiltonian is invariant under the global $U(1)$ shift $\theta_i \to \theta_i + \alpha$. In the low-temperature regime, the dominant excitations are spin waves, which are smooth, wavelike disturbances where the angle difference between any two adjacent spins is small. The local smoothness validates the expansion of $\cos(\theta_i - \theta_j)$ to the quadratic order, and taking the continuum limit yields

$$H_{\mathrm{XY}} \simeq E_0 + \frac{J}{2} \int d^2 r \, |\nabla \theta(\mathbf{r})|^2 \ , \tag{2.2}$$

where E_0 is the constant ferromagnetic ground state energy.[1] According to the Mermin-Wagner theorem, a continuous symmetry cannot be spontaneously broken in systems with short-range interactions at finite temperatures in dimensions $d \leq 2$ [1]. One can show that the average magnetization $\langle S_w \rangle$ in w direction is 0 in the thermodynamic limit at any nonzero temperature [24]. Consequently, there is no conventional long-range-order (LRO) low temperature ordered phase in 2D XY model; that is, its spin correlation function does not approach a non-zero constant as the distance $|i - j| \to \infty$.

[1] For now, we restrict our analysis to smooth angle fields (i.e., spin waves), which are free from singularities.

The spin-spin correlation function, $g(r)$, which measures the average alignment between spins separated by a vector $\mathbf{r}$, is defined in the continuum limit as

$$g(r) = \langle \mathbf{S}(0) \cdot \mathbf{S}(\mathbf{r}) \rangle = \langle e^{i[\theta(\boldsymbol{r}) - \theta(0)]} \rangle = \frac{\mathrm{tr}\left[e^{i(\theta(\boldsymbol{r}) - \theta(0))} e^{-\beta H}\right]}{\mathrm{tr}\left[e^{-\beta H}\right]} \,. \tag{2.3}$$

By expressing the angle field $\theta(\mathbf{r})$ as a sum over its Fourier modes $\theta_{\mathbf{k}}$,

$$\theta(\boldsymbol{r}) = \frac{1}{4\pi^2} \int \theta(\boldsymbol{k}) e^{i\boldsymbol{k}\cdot\boldsymbol{r}} d^2k \,, \tag{2.4}$$

one can show that the correlation function under spin-wave approximation has the form

$$\begin{aligned} g(r) &= \exp\left(-\frac{k_B T}{4\pi^2 J} \int \frac{1 - \cos(\boldsymbol{k}\cdot\boldsymbol{r})}{k^2} d^2k\right) \\ &= \exp\left(-\frac{k_B T}{2\pi J} \int_0^{\pi/a} dk \frac{1 - J_0(kr)}{k}\right) \\ &= \exp\left(-\frac{k_B T}{2\pi J} I(r)\right) \,, \end{aligned} \tag{2.5}$$

where J_0 is the zeroth-order Bessel function and we have introduced a high wave number cutoff $k_{\mathrm{cutoff}} = \pi/a$, where a is the associated microscopic length scale. We then let $u = kr$ and decompose the integral $I(r)$ into three parts [24]

$$\begin{aligned} I(r) &= \int_0^{\pi/a} dk \frac{1 - J_0(kr)}{k} \\ &= \int_1^{\pi r/a} \frac{du}{u} + \int_0^1 \frac{1 - J_0(u)}{u} du - \int_1^{\pi r/a} \frac{J_0(u)}{u} du \\ &= \ln\left(\frac{\pi r}{a}\right) + \gamma + O\left((\frac{\pi r}{a})^{-3/2}\right) \,, \end{aligned} \tag{2.6}$$

where

$$\gamma = \int_0^1 \frac{1 - J_0(u)}{u} du - \int_1^\infty \frac{J_0(u)}{u} du \approx -0.116 \,. \tag{2.7}$$

For long distance $r \gg a$, we can approximate $I(r) \approx \ln(\pi r/a)$ and,

$$g(r) \approx \exp\left(-\frac{k_B T}{2\pi J} \ln \frac{\pi r}{a}\right) = \left(\frac{\pi r}{a}\right)^{\frac{-k_B T}{2\pi J}} = \left(\frac{\pi r}{a}\right)^{-\eta(T)} \,. \tag{2.8}$$

We find that the decay of the spin correlation function exhibits an algebraic form with exponent $\eta(T)$ at long distances, indicative of quasi-long-range order (QLRO).

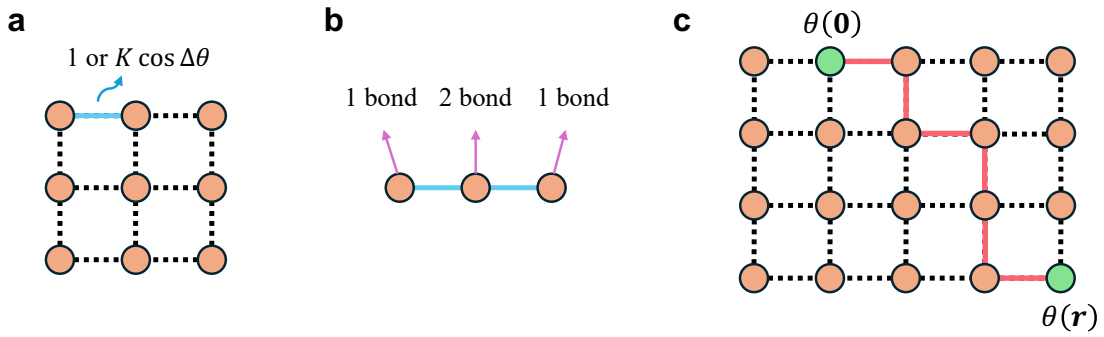

Figure 2.1: Graphical rules for the high-temperature expansion of the XY model. (**a**) Bond insertion: each nearest neighbour edge contributes either a factor 1 or $K\cos(\theta_i-\theta_j)$. (**b**) Sites with different number of bonds. (**c**) The lowest-order nonzero graph connecting θ_0 and $\theta_{\mathbf{r}}$ is the self-avoiding path linking the two sites (highlighted by red bonds), each contribute a $K/2$ to the integral.

We now examine the spin–spin correlation in the high-temperature regime. To evaluate the correlation function, we first perform a high-temperature expansion of the partition function

$$\mathcal{Z}=\mathrm{tr}\left[e^{-\beta H}\right]=\int_0^{2\pi}\prod_i\frac{d\theta_i}{2\pi}\prod_{\langle ij\rangle}\left[1+K\cos\left(\theta_i-\theta_j\right)+\mathcal{O}\left(K^2\right)\right]\,, \tag{2.9}$$

with $K=\beta J\to 0$ in the high temperature limit. Each bond on the lattice contributes a factor or either 1 or $K\cos(\theta_i-\theta_j)$ to the integral. Since $\int_0^{2\pi}\mathrm{d}\theta_i\cos\left(\theta_i-\theta_j\right)/2\pi=0$, all terms that are linear in K disappear after performing the integrations. Moreover, one can verify that any graph containing an odd number of bonds contributes zero to the integration, so only even powers of K survives. This implies that only the closed loop can survive for the partition function under high temperature expansion [25].

The spin-spin correlation function is calculated by

$$g(r)=\langle\mathbf{S}(0)\cdot\mathbf{S}(\mathbf{r})\rangle=\frac{1}{\mathcal{Z}}\int_0^{2\pi}\prod_i\frac{d\theta_i}{2\pi}\cos\left(\theta_0-\theta_{\mathbf{r}}\right)\prod_{\langle ij\rangle}\left[1+K\cos\left(\theta_i-\theta_j\right)+\mathcal{O}\left(K^2\right)\right]\,. \tag{2.10}$$

We first consider a site j at which two bonds impinge, one connecting to site i and the other to site k, its integral evaluates to $\int_0^{2\pi}\mathrm{d}\theta_j\cos\left(\theta_i-\theta_j\right)\cos\left(\theta_j-\theta_k\right)/2\pi=\frac{1}{2}\cos\left(\theta_i-\theta_k\right)$. This demonstrates that the integral which contributes nonzero factor has to be a closed loop, or a open path connecting θ_0 and $\theta_{\mathbf{r}}$. To the lowest nontrivial

order, the only surviving contribution to the numerator arises from the shortest self-avoiding path connecting θ_0 and $\theta_{\mathbf{r}}$, yielding a factor of $(K/2)^r$, as shown in Figure 2.1c. The high-temperature expansion of the partition function $\mathcal{Z}$ begins at order K^0, its reciprocal contributes only a constant at this order. Therefore, the spin-spin correlation in high temperature is

$$g(r) \approx \left(\frac{K}{2}\right)^r = e^{-r/\ell} \,, \tag{2.11}$$

where $\ell = 1/\ln(2/K)$ is the correlation length. This indicates that, at high temperatures, the spin-spin correlation function decays exponentially rather than following a power law. The distinct functional forms of the spin correlation function at low and high temperatures imply the existence of a finite temperature phase transition in the 2D XY model.

2.1.2 Berezinskii–Kosterlitz–Thouless transition

The qualitative change from exponential to algebraic correlations in the two–dimensional XY model is not a conventional symmetry–breaking transition as stated by the Mermin-Wagner theorem, but a *topological* one, first proposed by Berezinskii, Kosterlitz and Thouless [2, 3]. Its essential ingredients are topological defects in the phase field $\theta(\mathbf{r})$, which in the continuum limit satisfies the Laplace equation, $\nabla^2\theta(\boldsymbol{r}) = 0$.

Apart from the trivial, ferromagnetically ordered solution, $\theta(\mathbf{r}) = \text{const}$, this equation admits a class of non-trivial solutions known as *vortices*. These are topological defects characterised by a core region where the order parameter must vanish, surrounded by a far-field region where the phase varies slowly. The defining feature of a vortex is that the phase field $\theta(\mathbf{r})$ is multi-valued; a circuit along any closed contour Γ enclosing the vortex core results in a net change in the phase that is an integer multiple of 2π:

$$\oint_\Gamma \nabla\theta(\mathbf{r}) \cdot d\mathbf{l} = 2\pi n$$

where $n \in \mathbb{Z}$ is an integer known as the *winding number* or *topological charge*. A positive integer corresponds to a vortex, while a negative integer corresponds to

an antivortex. The integer quantisation is a necessary condition to ensure that the physical order parameter, $\vec{s}(\mathbf{r}) = (\cos\theta(\mathbf{r}), \sin\theta(\mathbf{r}))$, remains single-valued upon traversing the contour. A configuration containing a vortex cannot be continuously deformed into the uniformly ordered ground state (where $n = 0$), since the winding number is a discrete integer.

To understand the role of vortices in driving the transition, we can employ the free energy argument [26]. The energy of a single vortex with winding number n can be estimated from the Hamiltonian (see Eq. (2.2)). The phase gradient for such vortex is $\nabla\theta(\mathbf{r}) = (n/r)\hat{\boldsymbol{\theta}}$, leading to vortex energy[2]

$$E_{\mathrm{v}} = \frac{J}{2}\int d^2r(\nabla\theta)^2 = \pi J n^2 \ln\left(\frac{L}{\xi}\right) , \tag{2.12}$$

where L is the linear dimension of the system and ξ is a short-distance cutoff corresponding to the vortex core size, so that single vortex is considered to have an area of $\pi\xi^2$. This logarithmic divergence with system size suggests that an isolated vortex has an infinite energy cost in the thermodynamic limit ($L \to \infty$). At finite temperature, however, this energy cost is opposed by the configurational entropy of the vortex. The number of possible locations for the vortex core is approximately $(L/\xi)^2$, yielding an entropy $S_{\mathrm{v}} = 2k_B \ln(L/\xi)$. The resulting free energy for a single vortex is

$$F_{\mathrm{v}} = E_{\mathrm{v}} - TS_{\mathrm{v}} = \left(\pi J n^2 - 2k_B T\right)\ln\left(\frac{L}{\xi}\right) . \tag{2.13}$$

If we only consider the elementary excitations with lowest energy ($n = \pm 1$), this free energy changes sign at a critical temperature,

$$T_{\mathrm{KT}} = \frac{\pi J}{2k_B} . \tag{2.14}$$

For $T > T_{\mathrm{KT}}$, the entropic term dominates, making $F_v < 0$ and favouring the proliferation of free vortices (see Figure 2.2), which in turn disorders the system and leads to the exponential decay of correlations.

[2]Here we calculate the long-distance contribution to the vortex energy and introduce a distance cutoff. For this purpose, the continuum Hamiltonian is employed, as it correctly captures the behavior of the phase field far from the vortex core. The total vortex energy consists of this long-distance contribution together with a core energy (a constant), but the long-distance term dominates since it diverges with the system size.

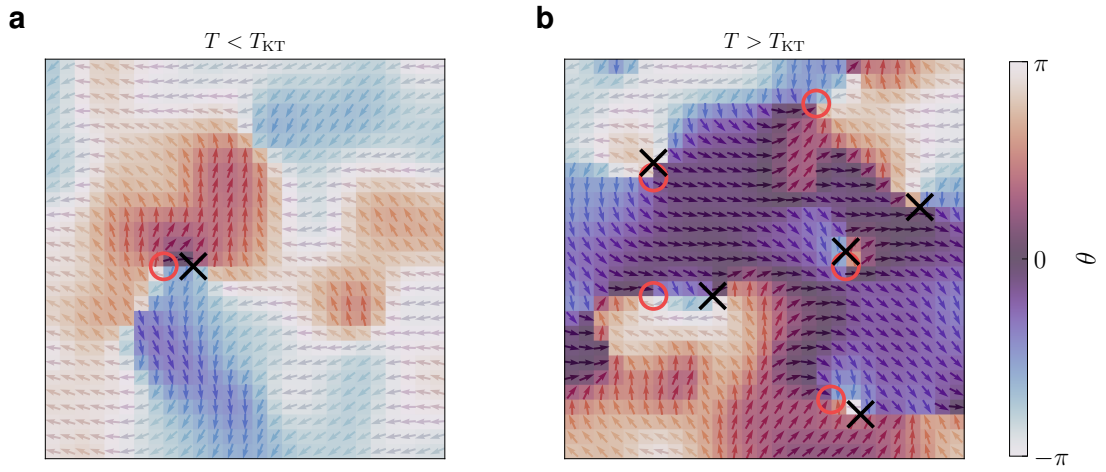

Figure 2.2: Illustration of topological defects in 2D XY model. Spin field on a square lattice (arrows) with the local azimuthal angle θ encoded by the adjacent color bar (ranging from $-\pi$ to π). (**a**) $T < T_{\mathrm{KT}}$: in the low-temperature phase, only tightly bound vortex–antivortex pairs are present (vortices marked by red circles, antivortices by black crosses) (**b**) $T > T_{\mathrm{KT}}$: above the BKT transition free vortices proliferate, as indicated by the multiple isolated defects.

The infinite energy of an isolated vortex implies that it is not possible to generate a single free vortex in the system in thermodynamic limit. However, it does not prohibit the vortices from being created in pairs of opposite charge, $(n, -n)$. The distortion field from such a vortex-antivortex pair decays rapidly with distance, and its interaction energy depends not on the system size L, but on the pair separation r, one can show that [24]

$$E_{\mathrm{pair}} = \pi J \left(n_1 + n_2\right)^2 \ln\left(L/\xi\right) + 2\pi J n_1 n_2 \ln\left(\xi/r\right) = 2\pi J \ln\left(r/\xi\right) \ , \tag{2.15}$$

where we have assumed $n_1 = 1$ and $n_2 = -1$. This energy is finite so bound vortex-antivortex pairs can be thermally excited at any temperature. The low-temperature phase is therefore not a vortex-free state, but rather a dilute gas of tightly bound pairs, as $E_{\mathrm{pair}} \propto \ln r$. These 'dipoles' do not destroy the quasi-long-range order of the system. The mechanism of the BKT transition is understood as being *unbinding* or *binding* of vortices. As temperature increases, the mean separation of these thermally excited pairs grows. At T_{KT}, the thermal energy overcomes logarithmic attraction and the pairs dissociate. This leads to a proliferation of free vortices and antivortices that screen the interactions, driving the system into the disordered

phase. This mechanism provides a qualitative picture for the topological phase transition in the 2D XY model, distinguishing it from conventional phase transitions based on spontaneous symmetry breaking.

2.1.3 Renormalisation group analysis

The free energy argument provides a compelling and qualitative picture, but a full understanding of the critical properties and nature of the phases requires the use of the renormalisation group (RG).

The RG analysis hinges on a duality mapping that transforms the statistical problem of interacting spins into that of a 2D Coulomb gas, where the vortices of the XY model become charged particles [3, 26]. By analysing the flow of the effective parameters of this Coulomb gas under a change of scale, we can precisely characterise the low-temperature phase, the high-temperature phase, and the universal properties of the transition that separates them. We begin with separating the spin-wave and vortex degrees of freedom. The spin angle field, $\theta(\mathbf{r})$, is decomposed into a smooth, curl-free component for spin waves, $\theta_{sw}(\mathbf{r})$, and a singular, divergence-free component for vortices, $\theta_v(\mathbf{r})$.

We first decompose the continuum Hamiltonian described in Eq. (2.2) into two independent parts: $H = H_{\mathrm{sw}} + H_{\mathrm{v}}$.

$$\begin{aligned} H_{\mathrm{XY}} &= H_{\mathrm{sw}} + H_{\mathrm{v}} \\ &= \frac{J}{2}\int d^2r\ |\nabla\theta_{\mathrm{sw}}(\mathbf{r})|^2 + \frac{J}{2}\int d^2r\ |\nabla\theta_{\mathrm{v}}(\mathbf{r})|^2\ . \end{aligned} \tag{2.16}$$

The spin-wave component, H_{sw}, governs the algebraic correlations in the low-temperature phase (see Section 2.1.1), whereas the vortex component, H_{v}, can be shown to take the form [25]

$$H_{\mathrm{v}} = E_{\mathrm{c}}\sum_i n_i^2 - 4\pi^2 J\sum_{i<j} n_i\, n_j\, G(\mathbf{r}_i - \mathbf{r}_j)\ , \tag{2.17}$$

with integer vorticities $n_i \in \mathbb{Z}$. Here, E_{c} denotes the vortex core energy and $G(\mathbf{r}) = \ln|\mathbf{r}|/(2\pi)$ is the two-dimensional Green's function of the Laplacian. Consequently, the full partition function factorizes as

$$\mathcal{Z} = \mathcal{Z}_{\mathrm{sw}}\,\mathcal{Z}_{\mathrm{v}}\ . \tag{2.18}$$

Restricting to elementary vortex excitations with $n_i = \pm 1$,[3] one obtains [25]

$$\mathcal{Z}_{\rm v} = \sum_{N=0}^{\infty} \frac{y^{2N}}{(N!)^2} \int \Big(\prod_{i=1}^{2N} d^2 r_i \Big) \exp\Big[4\pi^2 K \sum_{i<j} n_i n_j \, G(\mathbf{r}_i - \mathbf{r}_j) \Big] \,, \tag{2.19}$$

where the vortex fugacity is defined by $y = \exp(-E_{\rm c}/k_B T)$ and $K = \beta J$. To ensure a finite energy in the thermodynamic limit, the neutrality condition $\sum_i n_i = 0$ must be imposed, implying that vortices are created in neutral vortex–antivortex pairs. One may consider a configuration consisting of N_v vortices and antivortices and estimate the corresponding partition function in terms of an effective action $S_{\rm eff} = -\ln \mathcal{Z}_{\rm v}$, which takes the form [27]

$$\begin{aligned} S_{\rm eff} &\sim 2N_v \ln N_v + N_v \left(2\pi K \ln \frac{l_v}{\xi} + 2S_c \right) - 2N_v \ln \frac{L^2}{\xi^2} \\ &= L^2 \frac{2}{l_v^2} (\pi K - 2) \, \ln \frac{l_v \, e^{S_c/(\pi K - 2)}}{\xi} \,, \end{aligned} \tag{2.20}$$

where L denotes the linear system size, $l_v = L/\sqrt{N_v}$ is the mean vortex separation, and $S_c = -\ln y$ is the vortex core action. The equilibrium value of the mean separation l_v is obtained by minimizing $S_{\rm eff}$ with respect to l_v.

In the limit $S_c \gg 1$, this minimization shows that for $K > 2/\pi$ the effective action is minimized by $l_v \to \infty$, corresponding to a phase with suppressed free vortices, whereas for $K < 2/\pi$ the action admits a minimum at finite l_v, signaling the proliferation of vortices. The critical value $K_c = 2/\pi$ is the BKT critical temperature, is consistent with the discussion in Section 2.1.2 and will be recovered again from the RG analysis presented below.

Since the spin-wave sector reduces to a Gaussian functional integral that is analytically solvable, the phase transition necessarily arises from the topological (vortex) sector. In fact, $\mathcal{Z}_{\rm v}$ is equivalent to the partition function of a two-dimensional neutral Coulomb plasma comprising $2N$ unit charges [25, 28]. Applying the RG procedure then reveals how the equivalent effective Coulomb-gas interactions evolve under successive rescaling of the length scale. One finds that the effective interaction between two external charges located at $\mathbf{r}$ and $\mathbf{r}'$ can be expressed as [25]:

$$H_{\rm eff}\,(\mathbf{r} - \mathbf{r}') \simeq 4\pi^2 K_{\rm eff} G\,(\mathbf{r} - \mathbf{r}') \,, \tag{2.21}$$

[3] Higher-winding vortices are energetically suppressed and thus negligible.

where

$$K_{\text{eff}} = K - 4\pi^3 K^2 y^2 \int_1^\infty x^{3-2\pi K} dx + \mathcal{O}\left(y^4\right) . \tag{2.22}$$

Inverting equation (2.22) yields [4]

$$K_{\text{eff}}^{-1} = K^{-1} + 4\pi^3 y^2 \int_1^\infty x^{3-2\pi K} dx + \mathcal{O}\left(y^4\right) . \tag{2.23}$$

Then we introduce a infinitesimal small cutoff b and split the integral into tow parts, we get

$$\begin{aligned} K_{\text{eff}}^{-1} &= K^{-1} + 4\pi^3 y^2 \Big(\int_1^b x^{3-2\pi K} dx + \int_b^\infty x^{3-2\pi K} dx \Big) + \mathcal{O}(y^4) \\ &= \tilde{K}^{-1} + 4\pi^3 y^2 \int_b^\infty x^{3-2\pi K} dx + \mathcal{O}(y^4) \quad \Big(\tilde{K}^{-1} = K^{-1} + 4\pi^3 y^2 \int_1^b x^{3-2\pi K} dx \Big) \\ &= \tilde{K}^{-1} + 4\pi^3 b^{4-2\pi K} y^2 \int_1^\infty x^{3-2\pi K} dx + \mathcal{O}(y^4) \quad (\text{rescaling } x \to x/b) \\ &= \tilde{K}^{-1} + 4\pi^3 \tilde{y}^2 \int_1^\infty x^{3-2\pi \tilde{K}} dx + \mathcal{O}(y^4) , \quad (\text{use } 3 - 2\pi\tilde{K} = 3 - 2\pi K + \mathcal{O}(y^2)) \end{aligned} \tag{2.24}$$

where the final expression recovers the form of Eq. (2.23) but with the rescaled parameters, $\tilde{K}^{-1} = K^{-1} + 4\pi^3 y^2 \int_1^b x^{3-2\pi K} dx + \mathcal{O}\left(y^4\right)$ and $\tilde{y} = b^{2-\pi K} y$. By applying the transformation in Eq. (2.24) iteratively, we successively integrates out fluctuations at length scales below the cutoff b which coarse grains the system. This sequence of operations induces RG flow of the parameters whose self-similar character underlies the universality of the continuous phase transition [29].

The flow equations for the inverse interaction strength and the fugacity are obtained by considering $b = e^l \simeq 1 + l$, with $l \ll 1$, such that the integration range reduces as $\int_1^b \simeq \int_1^{1+l}$. One then finds

$$\frac{\tilde{K}^{-1} - K^{-1}}{l} = 4\pi^3 y^2 , \tag{2.25a}$$

$$\frac{\tilde{y} - y}{l} = \left(2 - \pi K\right) y . \tag{2.25b}$$

Taking the limit $l \to 0$, these finite-difference relations yield the differential RG flow equations

$$\frac{dK^{-1}}{dl} = 4\pi^3 y^2 , \tag{2.26a}$$

$$\frac{dy}{dl} = \left(2 - \pi K\right) y . \tag{2.26b}$$

[4] Here we assume small vortex fugacity y.

We find that K^{-1} increases monotonically. Eq. (2.26b) identifies a line of marginal stability at $K = 2/\pi$ (equivalent to $k_B T_{\mathrm{KT}} = \pi J/2$ derived by the free-energy argument in Section 2.1.2): when $K > 2/\pi$, the factor $(2 - \pi K)$ is negative, causing y to decay as $l \to \infty$; conversely, when $K < 2/\pi$, $(2 - \pi K)$ is positive and y grows.

Setting $x = K^{-1} - \pi/2$ and expanding Eq. (2.26) in the vicinity of $x = 0$, we find

$$\frac{dx}{d\ell} = 4\pi^3 y^2 \,, \tag{2.27a}$$

$$\frac{dy}{d\ell} = \frac{4}{\pi} xy \,. \tag{2.27b}$$

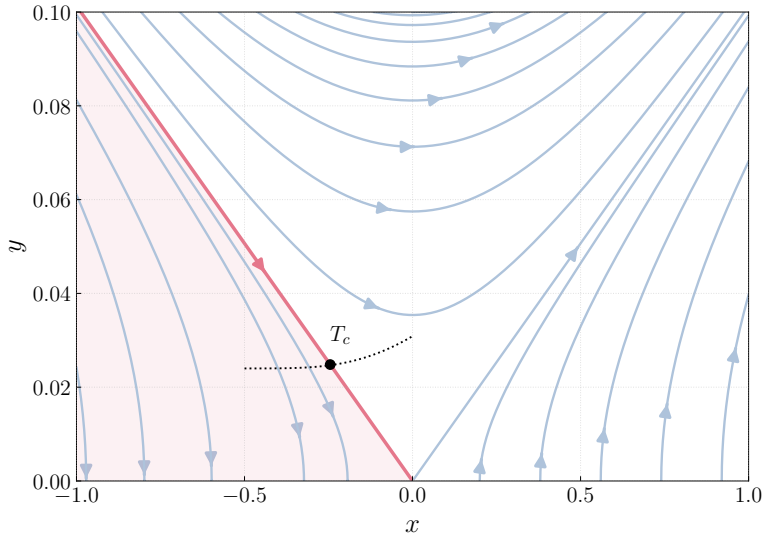

Figure 2.3: Renormalization group analysis of 2D XY model. RG flow in the (x, y) plane for the 2D XY model. The red line denotes the separatrix dividing flows attracted to the $y = 0$ fixed point (shaded region) from those flowing to infinite fugacity, $y \to \infty$. The dashed line indicates an example system crossing the phase boundary at the critical temperature T_c.

Figure 2.3 depicts the RG flow in the (x, y) plane. A clear separatrix (highlighted in red) divides two qualitatively distinct regimes:

- **Below** the separatrix, RG flows are driven to the fixed points at $y = 0$.
- **Above** the separatrix, the fugacity y is renormalised to ∞.

In the language of the XY model, the regime below the separatrix corresponds to the low-temperature phase, in which vortex–antivortex pairs remain bound and the

vortex fugacity y flows to 0 (which means it is an irrelevant perturbation under RG). Above the separatrix, free vortices proliferate, leading to the destruction of QLRO.

To derive the equation of this separatrix, we observe from the flow equations that $dy/dx = x/\pi^4 y$, which implies $x^2 - \pi^4 y^2 = c$, where c is a constant. Choosing the trajectory through the origin sets $c = 0$, yielding $x = \pm\pi^2 y$. The physically relevant separatrix corresponds to the negative branch, $x = -\pi^2 y$, indicates a nonzero fugacity (i.e., finite vortex core energy) lowers the transition temperature. To first order in the fugacity y, the BKT critical temperature is given by

$$T_{\mathrm{c}} = \frac{J}{k_B}\left(\frac{\pi}{2} - \pi^2 y\right) . \tag{2.28}$$

The origin of universality in the BKT transition is evident from the structure of the RG flow. The RG flow reveals that the critical separatrix terminates at an unstable fixed point at the origin, $(x, y) = (0, 0)$, at which any infinitesimal perturbation drives the system into one of the two stable macroscopic phases. The convergence of all critical systems to this one point imposes a universal condition on the renormalised stiffness at the transition, $K_{\mathrm{KT}} = 2/\pi$. From this universal relation, the value of the algebraic exponent of correlation function (see Eq. (2.8)) is uniquely determined at criticality to be $\eta_c = 1/(2\pi K_{\mathrm{KT}}) = 1/4$, establishing an upper bound for the exponent in the QLRO phase, $\eta \leq 1/4$.[5]

2.2 Coupled 2D XY Model

2.2.1 Bilayer XY Hamiltonian

We have introduced the 2D XY model and the celebrated BKT transition, we now consider two single-layer XY models which are coupled by interlayer coupling. The coupled 2D XY model describes two layers of XY spins with interactions both within each layer and between the layers. The total Hamiltonian for such a

[5]We note that the spin-wave derivation of the correlation function, Eq. (2.8), inherently ignores vortex excitations. This corresponds to the vortex-free subspace $y = 0$, in the RG flow diagram, which contains the line of stable fixed points describing the QLRO phase.

system can be expressed as the sum of the Hamiltonians for the individual layers and an interaction term between them

$$H = H_{\mathrm{a}} + H_{\mathrm{b}} + H_{\mathrm{ab}} \ , \tag{2.29a}$$

$$H_{\mathrm{k}} = -J \sum_{\langle i,j \rangle_{\mathrm{k}}} \cos(\theta_{i,\mathrm{k}} - \theta_{j,\mathrm{k}}) \ , \tag{2.29b}$$

$$H_{\mathrm{ab}} = -\Omega \sum_{i} \cos(\theta_{i,\mathrm{a}} - \theta_{i,\mathrm{b}}) \ , \tag{2.29c}$$

where k can be either a or b, denoting layer a and layer b. The terms H_{a} and H_{b} represent the standard intralayer XY interactions within each respective layer. The ferromagnetic coupling strength $J > 0$ is assumed to be the same for both layers (i.e., two identical layers). The interlayer coupling is described by H_{ab}. This term couples spins at the same site i in the two different layers, with $\Omega \geq 0$ being the strength of the interlayer coupling strength. This type of interaction is also referred to as a linear tunnel coupling. The coupled XY Hamiltonian still preserves $U(1)$ symmetry, but now requires simultaneous global rotation of both layers, $\theta_{i,\mathrm{a}} \to \theta_{i,\mathrm{a}} + \alpha$ and $\theta_{i,\mathrm{b}} \to \theta_{i,\mathrm{b}} + \alpha$. To understand the impact of the coupling on the system, we examine two limiting cases:

1. **Decoupled limit ($\Omega = 0$):** When the interlayer coupling is zero, the Hamiltonian describes two independent 2D XY models. Each layer undergoes a separate BKT transition at critical temperature $T_{\mathrm{c}} = T_{\mathrm{KT}}$.

2. **Strong coupling limit ($\Omega \to \infty$):** In the limit of infinitely strong coupling, the spins in the two layers are forced to align perfectly to minimize the energy, such that $\theta_{i,\mathrm{a}} = \theta_{i,\mathrm{b}}$, for all sites i. This makes $H_{\mathrm{a}} = H_{\mathrm{b}}$, and because H_{ab} is merely a constant, we get $H = 2H_{\mathrm{a}}$. The model effectively reduces to a single-layer 2D XY model with a doubled intralayer coupling strength of $2J$, resulting in a doubling of the critical BKT temperature $T_{\mathrm{c}} = 2T_{\mathrm{KT}}$.

We find that in the strong coupling limit the phase-locking term H_{ab} doubles the critical temperature. It is therefore natural to ask whether T_{c} undergoes a crossover from the decoupled single-layer critical temperature T_{KT} to $2T_{\mathrm{KT}}$ as the

interlayer coupling is increased. Indeed, several theoretical studies including effective models have reported that the critical temperature undergoes such a continuous crossover [12, 13, 30–32], and it has recently been experimentally observed in a tunnel-coupled 2D Bose gas system [14].

2.2.2 Antisymmetric and symmetric mode decomposition

It is convenient to decompose the bilayer system into antisymmetric and symmetric degrees of freedom. We define the relative (antisymmetric) phase $\varphi_{\mathrm{rel},i} = \theta_{i,\mathrm{a}} - \theta_{i,\mathrm{b}}$ and the common (symmetric) phase $\varphi_{\mathrm{com},i} = \theta_{i,\mathrm{a}} + \theta_{i,\mathrm{b}}$. The bilayer Hamiltonian can then be written as

$$H = -2J \sum_{\langle i,j \rangle} \cos\left(\frac{\varphi_{\mathrm{rel},i} - \varphi_{\mathrm{rel},j}}{2}\right) \cos\left(\frac{\varphi_{\mathrm{com},i} - \varphi_{\mathrm{com},j}}{2}\right) - \Omega \sum_i \cos(\varphi_{\mathrm{rel},i}) \ . \quad (2.30)$$

In the continuum limit, this Hamiltonian can be rewritten as

$$H \simeq \frac{J}{4} \int d^2r \, |\nabla \varphi_{\mathrm{rel}}(\mathbf{r})|^2 + \frac{J}{4} \int d^2r \, |\nabla \varphi_{\mathrm{com}}(\mathbf{r})|^2 - \Omega \int d^2r \cos(\varphi_{\mathrm{rel}}(\mathbf{r})) \ . \quad (2.31)$$

From this form, we can deduce the behavior in two limiting cases. For zero interlayer coupling, $\Omega = 0$, the Hamiltonian decouples into two independent XY models for the relative and common modes. Since these modes possess identical stiffness, they undergo a BKT transition simultaneously. In the strong-coupling limit, $\Omega \to \infty$, the energy is again minimized by locking the relative phase to $\varphi_{\mathrm{rel}} = 0$. The common phase then can be written as $\varphi_{\mathrm{com}} = 2\theta_a$, effectively reduces the Hamiltonian to a XY model with a doubled intralayer coupling strength of $J \to 2J$, implying a doubled critical BKT temperature. For finite interlayer coupling, the shift in the critical temperature in the common mode is identical to that of each individual layer. This is because the system only holds single $U(1)$ symmetry, $\theta_{\mathrm{a}} \to \theta_{\mathrm{a}} + \alpha$ and $\theta_{\mathrm{b}} \to \theta_{\mathrm{b}} + \alpha$. Therefore, they undergo a single, shared BKT transition.

The behaviour of the relative phase, however, is qualitatively different. For any finite interlayer coupling, $\Omega \neq 0$, the coupling term $-\Omega \cos(\varphi_{\mathrm{rel}})$ introduces a preferred value of $\varphi_{\mathrm{rel}} = 0$. This term explicitly breaks the continuous $U(1)$ rotational symmetry of the relative phase. Consequently, the relative phase no

longer undergoes a BKT transition. Instead, the system is expected to develop true LRO at low temperatures, corresponding to a non-zero expectation value of the order parameter $\langle e^{i\varphi_{\rm rel}}\rangle$.

2.2.3 Correlation functions in bilayer XY model

In the limit of vanishing interlayer coupling ($\Omega = 0$), each layer behaves as an independent 2D XY model. The single-layer correlation function is then given by (see Section 2.1.1)

$$g(r) = \left\langle e^{i[\theta(\mathbf{r})-\theta(0)]}\right\rangle = e^{-\frac{1}{2}\left\langle[\theta(\mathbf{r})-\theta(0)]^2\right\rangle} \propto \begin{cases} r^{-\eta}, & T < T_{\rm KT} \quad \left(\eta \le \frac{1}{4}\right) , \\ \exp\left(-r/\ell\right), & T > T_{\rm KT} . \end{cases} \tag{2.32}$$

Here we have used the Gaussian identity $\left\langle e^{iX}\right\rangle = e^{-\langle X^2\rangle/2}$ for zero-mean Gaussian random variable X. For the common mode, its correlation function is

$$\begin{aligned} g_{\rm com}(r) &= \left\langle e^{i[\varphi_{\rm com}(\mathbf{r})-\varphi_{\rm com}(0)]}\right\rangle \\ &= \left\langle e^{i[\theta_{\rm a}(\mathbf{r})-\theta_{\rm a}(0)]}\right\rangle \left\langle e^{i[\theta_{\rm b}(\mathbf{r})-\theta_{\rm b}(0)]}\right\rangle \\ &= g^2(r) , \end{aligned} \tag{2.33}$$

where we have used the fact that the fields $\theta_a(\boldsymbol{r})$ and $\theta_b(\boldsymbol{r})$ are statistically independent in the absence of interlayer coupling. We find the common-mode correlations decay as the square of the single-layer correlations, implying that $\eta_{\rm com,c} = 2\eta_{\rm c} = 1/2$. Similarly, one finds that the relative mode behaves in exactly the same way, $g_{\rm rel}(r) = g^2(r)$.

In the limit of strong interlayer coupling ($\Omega \to \infty$), the single-layer correlation function remains identical to that of the decoupled case, since the RG flow fixes the universal exponent at $\eta_{\rm c} = 1/4$.[6] The common mode correlation function

[6]Under RG, one always obtains the universal condition $K_{\rm KT} = 2/\pi$ (see Section 2.1.3), irrespective of the bare stiffness J. In the infinite-coupling limit each layer's effective stiffness doubles ($J \to 2J$), which raises the critical temperature to $T_{\rm c} = 2T_{\rm KT}$. The universal exponent remains $\eta_{\rm c} = -2k_{\rm B}T_{\rm KT}/4\pi J = 1/4$.

takes the form

$$\begin{aligned} g_{\rm com}(r) &= \left\langle e^{i[\varphi_{\rm com}(\mathbf{r})-\varphi_{\rm com}(0)]} \right\rangle \\ &= \left\langle e^{i[2\theta_{\rm a}(\mathbf{r})-2\theta_{\rm a}(0)]} \right\rangle \\ &= e^{-\frac{1}{2}\left\langle [2\theta_{\rm a}(\mathbf{r})-2\theta_{\rm a}(0)]^2 \right\rangle} \\ &= e^{-2\left\langle [\theta_{\rm a}(\mathbf{r})-\theta_{\rm a}(0)]^2 \right\rangle} \\ &= g^4(r) \ , \end{aligned} \tag{2.34}$$

from which one can immediately read off the critical exponent for the common mode $\eta_{{\rm com},c} = 4\eta_{\rm c} = 1$. The correlation function of relative mode under the strong interlayer coupling limit is just $g_{\rm rel}(r) = 1$ as all relative phases are locked to $\varphi_{\rm rel} = 0$.

For finite interlayer coupling ($\Omega \neq 0$), the relative-mode correlation function takes the approximate form, $g_{\rm rel}(r) \sim C + Ae^{-r/\ell}$, where ℓ is related to the correlation length of the phase-locked state, C is the long-distance constant offset, and A is a nonuniversal amplitude and normalized such that $C + A = 1$ [9]. Consequently, the relative phase exhibits true long-range order, $\lim_{r\to\infty} g_{\rm rel}(r) = C$. Meanwhile, one can show that the common correlation retains its strong-coupling form, $g_{\rm com}(r) = g^4(r)$ [32].

2.2.4 BKT paired phase

A "BKT-paired phase" has been proposed in the coupled XY model, in which correlations of the common mode decay algebraically while single-layer correlations decay exponentially [31, 33]. However, a recent study demonstrates that this phase cannot occur with the two-body interlayer coupling introduced in Section 2.2.1. We have seen that the common phase and single layer phase should share the same BKT transition based on a symmetry argument. One can further show that $g_{\rm com}(r) \leq g(r)$ in the strong coupling limit [32]. The realization of the BKT paired phase requires a four-body coupling term [32], as opposed to the conventional linear (first-order) Josephson coupling

$$\begin{aligned} H_{\rm ab}^{\text{4-body}} &= -\Omega \sum_{\langle ij \rangle} \cos\left(\theta_{i,a} + \theta_{i,b} - \theta_{j,a} - \theta_{j,b}\right) \\ &= -\Omega \sum_{\langle ij \rangle} \cos\left(\varphi_{{\rm com},i} - \varphi_{{\rm com},j}\right) \ . \end{aligned} \tag{2.35}$$

This four-body interaction endows the system with a $U(1) \times U(1)$ symmetry, corresponding to independent phase shifts in each layer, $\theta_{\mathrm{a}} \to \theta_{\mathrm{a}} + \alpha$ and $\theta_{\mathrm{b}} \to \theta_{\mathrm{b}} + \beta$. As a result, the symmetry of the common phase can be independent of that of either individual layer, though not independent of both simultaneously. The existence of two distinct lines of BKT phase transitions is permitted.

It is worth noting that the four-body interlayer coupling shifts the critical temperature of a single layer up to a maximum of $T_{\mathrm{c}} = 2T_{\mathrm{KT}}$, analogous to the effect of the two-body interlayer coupling. This can be seen by writing the Hamiltonian 2.29a as

$$H = -2J \sum_{\langle i,j \rangle} \cos\left(\frac{\varphi_{\mathrm{rel},i} - \varphi_{\mathrm{rel},j}}{2}\right) \cos\left(\frac{\varphi_{\mathrm{com},i} - \varphi_{\mathrm{com},j}}{2}\right) - \Omega \sum_{\langle ij \rangle} \cos(\varphi_{\mathrm{com},i} - \varphi_{\mathrm{com},j}) \ . \tag{2.36}$$

In the strong-coupling limit, the common phase is ordered, so that $\theta_{i,a} + \theta_{i,b} \approx \theta_{j,a} + \theta_{j,b}$ for neighboring sites. The Hamiltonian then reduces to

$$\begin{aligned} H &\approx -2J \sum_{\langle i,j \rangle} \cos\left(\frac{\varphi_{\mathrm{rel},i} - \varphi_{\mathrm{rel},j}}{2}\right) \\ &= -2J \sum_{\langle i,j \rangle} \cos\left(\frac{\theta_{i,a} - \theta_{i,b} - \theta_{j,a} + \theta_{j,b}}{2}\right) \\ &\approx -2J \sum_{\langle i,j \rangle} \cos\left(\frac{2\theta_{i,a} - 2\theta_{j,a}}{2}\right) \\ &= -2J \sum_{\langle i,j \rangle} \cos(\theta_{i,a} - \theta_{j,a}) \ . \end{aligned} \tag{2.37}$$

Therefore, the system maps onto the two-dimensional XY model of a single layer with doubled intralayer interaction, corresponding to a critical temperature that is twice the usual Kosterlitz–Thouless value.

2.3 Bilayer 2D Bose Gases

2.3.1 Absence of condensation in uniform ideal 2D Bose gases

The behavior of quantum gases is fundamentally tied to the dimensionality of the system in which they are confined. While the three-dimensional (3D) ideal Bose

gas famously exhibits a phase transition into a Bose-Einstein Condensate (BEC) below a critical temperature, the situation in two dimensions (2D) is markedly different. For a uniform, non-interacting 2D Bose gas in the thermodynamic limit, a true BEC does not form at any non-zero temperature.

This prohibition is a direct consequence of the single-particle density of states $g(\epsilon)$, which describes the number of states $g(\epsilon)d\epsilon$ between the energy interval ϵ and $\epsilon + d\epsilon$. In 3D, $g(\epsilon) \propto \epsilon^{1/2}$, meaning the number of available states decreases at low energies. This leads to the saturation of the excited states as the temperature is lowered, forcing excess particles into the ground state to form a condensate. In contrast, the density of states for a free particle in 2D is constant, $g(\epsilon) = mL^2/(2\pi\hbar^2)$, where m is the particle mass and L^2 is the area of the system. If there is no condensation, the total number of particles N is given by

$$N = \int_0^\infty \frac{g(\epsilon)}{e^{\beta(\epsilon-\mu)} - 1} d\epsilon \,, \tag{2.38}$$

where $\beta = 1/(k_B T)$ and the chemical potential $\mu \leq 0$ (assume the ground state energy $\epsilon_{\min} = 0$). For the 2D case, this gives

$$N = \frac{mL^2}{2\pi\hbar^2} \int_0^\infty \frac{1}{e^{\beta(\epsilon-\mu)} - 1} d\epsilon = -\frac{L^2}{\lambda_{\text{th}}^2} \ln\left(1 - e^{\beta\mu}\right) \,, \tag{2.39}$$

where $\lambda_{\text{th}} = h/\sqrt{2\pi m k_B T}$ is the thermal de Broglie wavelength. Rearranging for the 2D phase-space density (PSD), $\mathcal{D} = n\lambda_{\text{th}}^2$, where $n = N/L^2$ is the 2D density, we get

$$\mathcal{D} = -\ln(1 - Z) \,, \tag{2.40}$$

where $Z = e^{\beta\mu}$ is the fugacity. This equation always has a valid solution for any finite phase-space density with a corresponding negative chemical potential. Unlike in 3D, the excited states never saturate, and thus a macroscopic occupation of the ground state is not required to accommodate all particles, although the ground state is macroscopically occupied at zero temperature. Consequently, a BEC transition does not occur in a uniform ideal 2D Bose gas at any finite temperature.

2.3.2 Condensation in finite systems and harmonic traps

The conclusion that a 2D ideal Bose gas cannot condense is strictly valid only for a uniform system in the thermodynamic limit. Experimental systems are necessarily finite and often subjected to external trapping potentials. These conditions can restore the possibility of a condensation.

For an ideal gas confined to a finite box of area L^2, the continuous energy spectrum is replaced by discrete energy levels. This introduces a finite energy gap between the ground state and the first excited state. In this system there is no sharp phase transition in the formal sense but a crossover to a condensed state occurs when the PSD $\mathcal{D}$ becomes large enough that the correlation length of the gas exceeds the system size L. This happens at a size-dependent critical PSD, $\mathcal{D}_{\mathrm{c}} \approx \ln(4\pi L^2/\lambda_{\mathrm{th}}^2)$ [34], at which point a significant fraction of particles begins to occupy the ground state, forming a condensate.

A more profound change occurs for a gas that is confined in a 2D harmonic potential $V(r) = \frac{1}{2}m\omega_r^2 r^2$, with radial trapping frequency $\omega_r = 2\pi f_r$. The trapping potential fundamentally alters the single-particle density of states. For a 2D harmonic oscillator, the density of states is proportional to energy, $g(\epsilon) = \epsilon/(\hbar\omega_r)^2$, rather than being constant. For this linear dependence the number of available states vanishes as $\epsilon \to 0$, so the behavior is analogous to that of a uniform 3D gas, where the density of states also decreases at low energies. This feature once again allows for the saturation of excited states. The maximum number of particles, N_c, that can occupy the excited states at a given finite temperature is given by

$$N_{\mathrm{c}}(T) = \int_0^\infty \frac{g(\epsilon)}{e^{\beta\epsilon} - 1} d\epsilon = \frac{\pi^2}{6}\left(\frac{k_B T}{\hbar\omega_r}\right)^2 . \tag{2.41}$$

The non-zero critical temperature for the condensation, T_c, is then defined as $N = N_{\mathrm{c}}$, and leads to

$$k_B T_{\mathrm{c}} = \hbar\omega_r \sqrt{\frac{6N}{\pi^2}} \approx 0.78\hbar\omega_{\mathrm{r}}\sqrt{N} . \tag{2.42}$$

Remarkably, this transition persists even in the thermodynamic limit (defined for a trapped gas as $N \to \infty$ and $\omega_r \to 0$ while keeping $N\omega_r^2$ constant [34]). Therefore,

the presence of a harmonic trap restores a conventional BEC transition to the ideal 2D Bose gas, a phenomenon absent in the uniform case.

2.3.3 Interaction in 2D Bose gases

So far we have considered the ideal Bose gas, without any interaction between atoms. The introduction of repulsive interactions between particles fundamentally alters the low-temperature behavior of the 2D Bose gas. At the low temperatures relevant for quantum gases, the effective interaction strength between atoms is given by $U = 4\pi\hbar^2 a_s/m$, where a_s is the 3D s-wave scattering length [35]. The 3D mean-field interaction energy is given by

$$E_{\mathrm{int,3D}} = \frac{U}{2}\int n_{\mathrm{3D}}^2(\mathbf{r})d^3r \ . \tag{2.43}$$

In the quasi-2D experimental implementations [36–42], atoms are normally tightly confined in one dimension (z-direction). This freezes the dynamics in the z-direction, but the confinement length $a_z = \sqrt{\hbar/m\omega_{\mathrm{z}}}$ is still much larger than the 3D scattering length ($a_s \sim 5$ nm for ^{87}Rb atoms), so that the collisions remain 3D events. By integrating out the frozen z-dimension (assuming a Gaussian density profile), the interaction energy of the gas can be expressed in an effective 2D form

$$E_{\mathrm{int,2D}} = \frac{g}{2}\int n(\mathbf{r})^2 d^2r \ , \tag{2.44}$$

where $n(r)$ is the local 2D density, and g is the effective 2D interaction strength. For a gas harmonically confined in the z-direction, the interaction strength is given by [43]

$$g = U\int dz\rho(z) \sim \frac{\sqrt{8\pi}a_s}{\ell_0}\frac{\hbar^2}{m} = \frac{\hbar^2\tilde{g}}{m} \ , \tag{2.45}$$

where $\tilde{g}$ is the dimensionless interaction strength. This dimensionless nature of the interaction strength is a unique feature of the 2D Bose gas. It implies that the relative importance of interaction energy versus kinetic energy is independent of the gas density or intrinsic length scale, a property known as scale invariance. This is in contrast to the 3D case where this ratio depends on $n_{\mathrm{3D}}a_{\mathrm{s}}^3$.

2.3.4 Bogoliubov analysis and suppression of density fluctuations

While interactions do not induce a conventional BEC in a uniform system, they are crucial for the emergence of superfluidity in a 2D system, as they can suppress density fluctuations when the interaction is repulsive. We have seen that the interaction energy is proportional to $\int n(\mathbf{r})^2 d^2r = L^2 \langle n^2(\mathbf{r})\rangle$. To minimize this energy at a fixed average density $\langle n(\mathbf{r})\rangle$, the system must minimize the variance of the density, $(\Delta n)^2 = \langle n^2(\mathbf{r})\rangle - \langle n(\mathbf{r})\rangle^2$, which quantifies the magnitude of density fluctuations.

To see this more clearly, we consider the classical field Hamiltonian for a gas with two-body contact interactions

$$H = \int d^2r \left[\frac{\hbar^2}{2m}|\nabla\psi(\mathbf{r})|^2 + \frac{g}{2}|\psi(\mathbf{r})|^4\right] , \tag{2.46}$$

where the classical Bose field $\psi(\mathbf{r})$ can be written in a density-phase representation, $\psi(\mathbf{r}) = \sqrt{n(\mathbf{r})}e^{i\phi(\mathbf{r})}$. When temperature is near $T = 0$, we can assume that thermal fluctuations in the density are small, and write the local density as a small deviation $\rho(\mathbf{r})$ from the mean density n, such that $|\psi(\mathbf{r})|^2 = n(1 + 2\delta\rho(\mathbf{r}))$, with $\rho \ll 1$. Substituting this into the Hamiltonian and keeping terms up to second order in the fluctuations, the energy of the system separates into two distinct parts

$$H \approx \frac{\hbar^2 n}{2m}\int(\nabla\phi(\mathbf{r}))^2 d^2r + \int\left[\frac{\hbar^2 n}{2m}(\nabla\delta\rho(\mathbf{r}))^2 + 2gn^2\delta\rho^2(\mathbf{r})\right]d^2r , \tag{2.47}$$

where the first term depends only on gradients of the phase, and has the same form as the 2D XY model continuum Hamiltonian (see Eq. (2.2)). The second term, which describes the energy of density fluctuations $\delta\rho(\mathbf{r})$, contains the term $2gn^2\delta\rho^2(\mathbf{r})$, indicating that any deviation from the uniform density ($\rho \neq 0$) has an energy cost proportional to $2gn^2$. To obtain a quantitative measure of the density fluctuations, one performs a Bogoliubov analysis [34, 44]. This analysis of the system's modes yields the ratio between the Fourier amplitudes of density and phase fluctuations, $\rho_{\boldsymbol{k}}$ and $\phi_{\boldsymbol{k}}$,

$$\frac{\langle|\rho_{\mathbf{k}}|^2\rangle}{\langle|\phi_{\mathbf{k}}|^2\rangle} = \frac{\hbar^2k^2/2m}{\hbar^2k^2/2m + 2gn} . \tag{2.48}$$

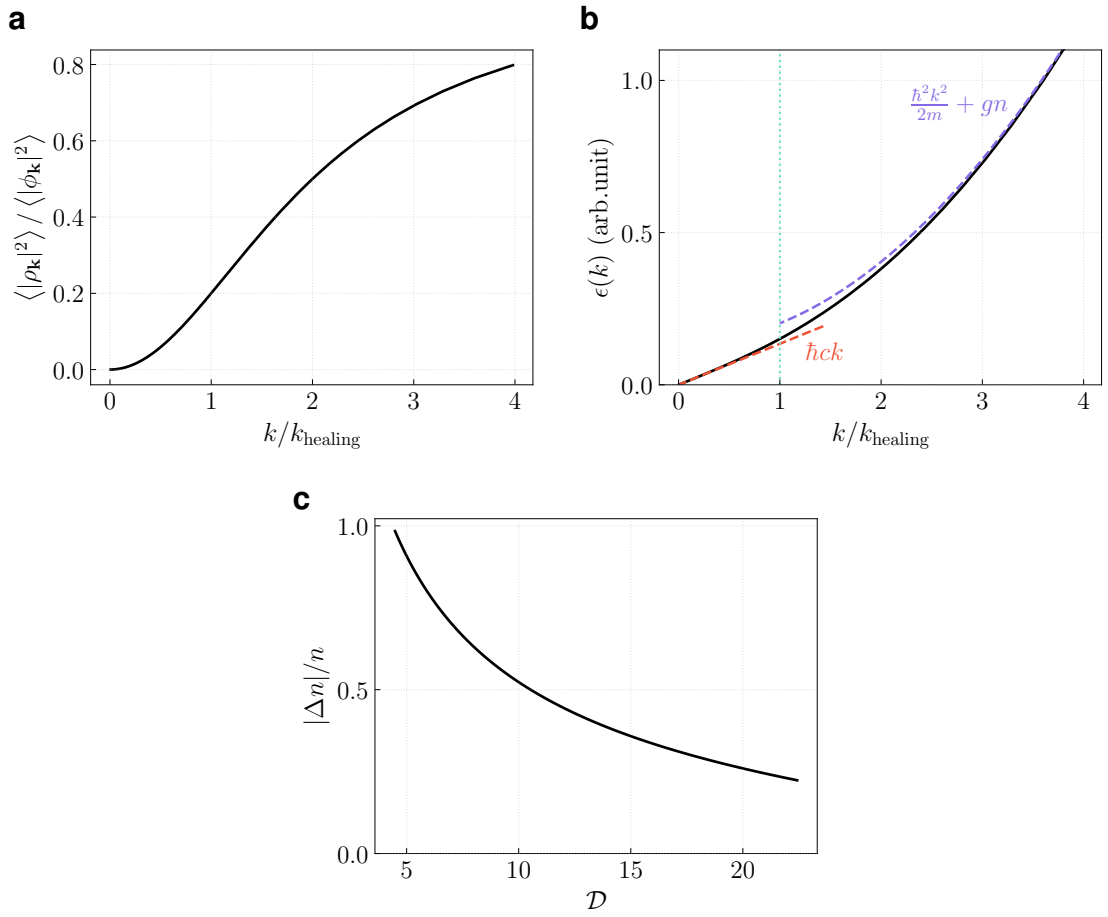

Figure 2.4: Bogoliubov analysis of 2D Bose gas. (**a**) The ratio of Fourier amplitudes of density and phase fluctuations approaches to 0 when $k \ll k_{\text{healing}}$, the x-axis is rescaled by $k_{\text{healing}} \sim 1/\xi$. (**b**) Bogoliubov excitation spectrum of 2D Bose gas. The black solid curve shows the dispersion from Eq. (2.49). The red dashed line indicates the linear, phononic approximation for wavelengths $\lambda \gg \xi$; the purple dashed line indicates the quadratic, free-particle–like approximation for $\lambda \ll \xi$. The blue dotted line denotes $k = k_{\text{healing}}$. (**c**) Relative density fluctuations are suppressed as the PSD increases. For the calculation we use $\tilde{g} = 0.08$ and $n \approx 22\ \mu m^{-2}$, representative of typical experimental parameters.

We observe that the ratio approaches zero for small k (see Figure 2.4a), indicating that long-wavelength excitations are predominantly governed by phase fluctuations and the density fluctuations are suppressed. The analysis also yields the dispersion relation for the elementary excitations

$$\epsilon_k = \sqrt{\frac{\hbar^2 k^2}{2m}\left(\frac{\hbar^2 k^2}{2m} + 2gn\right)}\,. \tag{2.49}$$

This relation interpolates between two important physical regimes. In the low-

momentum limit ($k \to 0$), the dispersion is linear, $\epsilon_{\mathrm{k}} \approx \hbar c k$, where $c = \sqrt{gn/m}$ is the speed of sound. This indicates that the long-wavelength excitations are collective, sound-like modes (phonons). In the high-momentum limit, the dispersion becomes like that of a free particle, $\epsilon_{\mathrm{k}} \approx \hbar^2 k^2/2m + gn$. In the crossover regime it is useful to define a characteristic length scale, the healing length ξ,[7] by

$$\xi = \frac{\hbar}{\sqrt{mgn}} = \frac{1}{\sqrt{\tilde{g}n}} \, . \tag{2.50}$$

Furthermore, the relative density fluctuations can be estimated by integrating over all density modes

$$\frac{\Delta n^2}{n^2} \approx \frac{2}{n\lambda_{\mathrm{th}}^2} \ln\left(\frac{k_B T}{2gn}\right) \, . \tag{2.51}$$

For a degenerate gas with high PSD, $\mathcal{D} = n\lambda_{\mathrm{th}}^2 \gg 1$, the prefactor $2/\mathcal{D}$ is small, and thus the relative density fluctuations are strongly suppressed, as shown in Figure 2.4c.

2.3.5 Mapping between 2D Bose gases and the 2D XY model

We have seen that for $k < k_{\mathrm{healing}}$, the dominant long-wavelength excitations in a 2D Bose gas are phonons in the phase mode. In this regime, density fluctuations are strongly suppressed, the long-distance behavior is thus well described by an effective low-temperature, phase-only Hamiltonian

$$H = \frac{\hbar^2 n_{\mathrm{s}}}{2m} \int (\nabla \phi(\mathbf{r}))^2 d^2 r \, . \tag{2.52}$$

Here we heuristically introduce the superfluid density $n_{\mathrm{s}} \leq n$ to account for the effects of residual density fluctuations (which are never entirely suppressed at any finite temperature) as well as short-distance physics [34, 45]. We observe that the resulting Hamiltonian has the same form as the continuum limit of the 2D XY model (Eq. (2.2)), implying that the 2D Bose gas can be mapped onto the 2D XY model in the low-temperature regime. Consequently, one naturally expects a BKT transition to occur in the phase of the 2D Bose gas when the temperature is sufficiently low.

[7] Alternatively, the healing length can be defined by equating the kinetic energy per particle to the interaction energy, yielding an expression $\xi = \frac{\hbar}{\sqrt{2mgn}}$ [35], differing by $1/\sqrt{2}$

Consider the superfluid component $\psi(\mathbf{r}) = \sqrt{n_\mathrm{s}}\, e^{i\phi(\mathbf{r})}$ with uniform density, governed by the Hamiltonian in Eq. (2.52). The first-order correlation function is then

$$g_1(\mathbf{r}, \mathbf{r}') = \langle \psi^*(\mathbf{r})\psi(\mathbf{r}')\rangle = n_\mathrm{s} \left\langle e^{\,i[\phi(\mathbf{r})-\phi(\mathbf{r}')]} \right\rangle . \tag{2.53}$$

By mapping to the 2D XY model, we find the QLRO correlation

$$g_1(\mathbf{r}, \mathbf{r}') \;\propto\; n_\mathrm{s}\, |\mathbf{r}-\mathbf{r}'|^{-\eta(T)} , \tag{2.54}$$

for $|\mathbf{r}-\mathbf{r}'| \gg \xi$, with the temperature-dependent exponent

$$\eta(T) = \frac{m k_B T}{2\pi\hbar^2 n_\mathrm{s}} = \frac{1}{n_\mathrm{s}\,\lambda_\mathrm{th}^2} = \frac{1}{\mathcal{D}_\mathrm{s}} , \tag{2.55}$$

where $\mathcal{D}_\mathrm{s} = n_\mathrm{s}\,\lambda_\mathrm{th}^2$ is the superfluid PSD. As we have already shown in Section 2.1.3, the critical exponent at the BKT transition takes the universal value $\eta(T_c) = 1/4$. This implies the universal relation

$$n_\mathrm{s}(T_c) = \frac{2 m k_B T_\mathrm{c}}{\pi\hbar^2} , \tag{2.56}$$

meaning that the superfluid density cannot fall below this value at the transition. This discontinuity is the Nelson-Kosterlitz *universal jump* of the superfluid density in the vicinity of the BKT critical point [46].

For temperatures $T > T_\mathrm{c}$, but with density fluctuations still suppressed, vortex–antivortex pairs in the phase field unbind and destroy the quasi–long-range order, as discussed in Section 2.1.2. In a 2D Bose gas, the vortex core size is set by the healing length ξ, producing a density dip of this size. To quantitatively examine how a vortex in the phase field affects the density profile, it is useful to start from Eq. (2.46) and express the order parameter as $\psi(\mathbf{r}) = f(\mathbf{r})\, e^{i\phi_\mathrm{v}(\mathbf{r})}$, where $\phi_\mathrm{v}(\mathbf{r})$ denotes the phase field associated with a vortex. We then obtain

$$E = \int d^2 r \left[\frac{\hbar^2}{2m} (\nabla f)^2 + \frac{\hbar^2}{2m}\frac{f^2}{r^2} + \frac{g}{2} f^4 \right] . \tag{2.57}$$

Here we have used $\nabla\phi_\mathrm{v}(\mathbf{r}) = \frac{1}{r}\,\hat{\boldsymbol{\theta}}$. The equation for $f(r)$ is then derived from the variational principle $\delta(E-\mu N) = 0$. This yields, assuming rotational symmetry (which is natural for a vortex),

$$-\frac{\hbar^2}{2m}\left[\frac{1}{r}\frac{\partial}{\partial r}\left(r\frac{\partial f}{\partial r}\right)\right] + \frac{\hbar^2 f}{2m r^2} + g f^3 = \mu f . \tag{2.58}$$

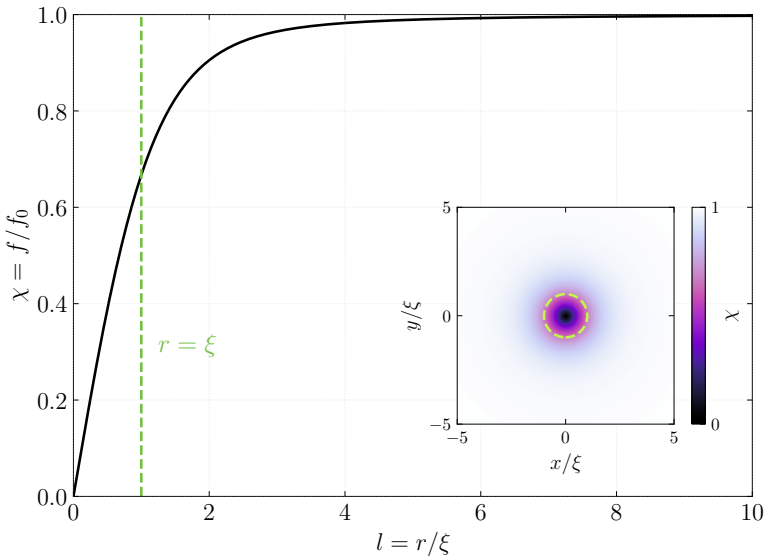

Figure 2.5: Density dip of a single vortex. Numerical solution of Eq. (2.58) showing the normalized density χ as a function of the scaled radius l. The density vanishes at the vortex core and approaches the asymptotic value f_0 for $r \gg \xi$. The green dashed line marks the healing length ξ. Inset: density of the vortex in 2D. The green dashed circle indicates a radius equal to the healing length, illustrating the core size in the 2D profile.

We have so far assumed that density fluctuations are strongly suppressed, and we have already shown that this assumption holds within the healing length. In this context, we introduce the dimensionless radial coordinate $l = r/\xi$ and the normalized density profile $\chi = f/f_0$, where f_0 denotes the equilibrium density far from the vortex core, together with the relation $\hbar^2/(m\xi^2) \simeq ng = f_0^2 g = \mu$. In terms of these scaled variables, Eq. (2.58) takes the form [35]

$$-\frac{1}{l}\frac{d}{dl}\left(l\frac{d\chi}{dl}\right) + \frac{\chi}{l^2} + 2\chi^3 - 2\chi = 0\,. \tag{2.59}$$

The result is shown in Figure 2.5, and we can see the vortex in phase produces a density dip with size $\sim \xi$.

2.3.6 Local correlation approximation in harmonic traps

The algebraic decay of correlations is a hallmark of the superfluid phase in a uniform 2D system, but experimental systems are typically confined in harmonic traps, leading to an inhomogeneous density profile. To account for this, the standard Local Density Approximation (LDA) can be extended to the correlation properties

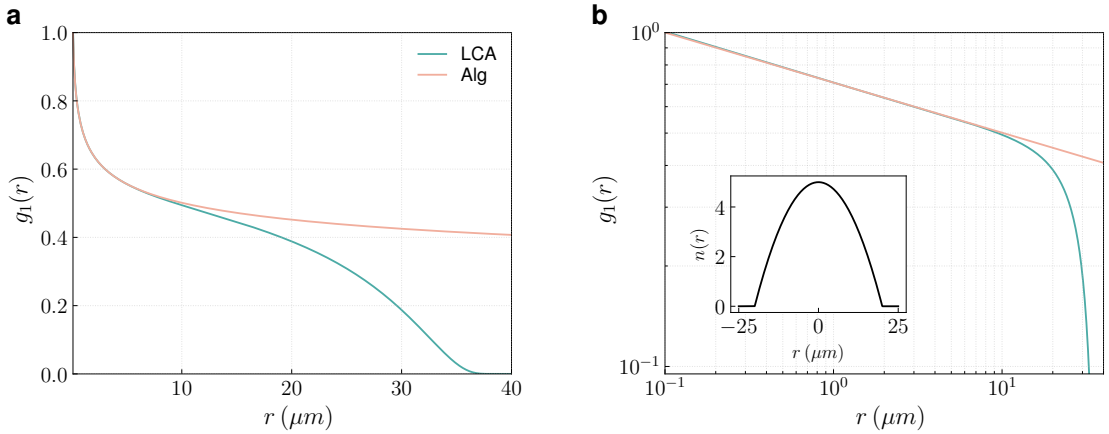

Figure 2.6: Local correlation approximation. First-order phase correlation function for a uniform gas (ALG) with $\eta = 0.15$ and for an inhomogeneous gas treated within the local correlation approximation (LCA) with central exponent $\eta_0 = 0.15$, shown on (**a**) linear and (**b**) log-log scales. Inset: Thomas–Fermi density profile in a harmonic trap, used in the LCA calculation of the correlation function.

themselves in what is known as the *Local Correlation Approximation* (LCA) [47]. The key idea is to replace the uniform algebraic exponent η with a local, position-dependent exponent that is modulated by the spatially varying density. Therefore, the inhomogeneous algebraic exponent is given by

$$\eta\left(\boldsymbol{r}, \boldsymbol{r}'\right) = \eta_0 \frac{n_0}{\sqrt{n(\boldsymbol{r}) n\left(\boldsymbol{r}'\right)}}\ , \tag{2.60}$$

where n_0 and η_0 are the local density and algebraic exponent at the center of the harmonic trap. This approximation captures the essential physics in the low-density regions near the edges of the cloud where the correlations decay more rapidly and to lower values than in the uniform gas (see Figure 2.6). Thus the LCA provides a useful framework for interpreting correlation measurements in trapped 2D Bose gases.

2.3.7 Tunnel-coupled bilayer 2D Bose gas

We now turn our attention to a system composed of two parallel, tunnel-coupled 2D Bose gases. The layers interact via a Josephson-type coupling that facilitates particle

exchange. The total classical field Hamiltonian for this bilayer system is given by:

$$\begin{aligned} H &= H_1 + H_2 + H_{12} \ , \\ H_a &= \int d^2\mathbf{r} \left[\frac{\hbar^2}{2m} |\nabla \psi_a(\mathbf{r})|^2 + \frac{g}{2} |\psi_a(\mathbf{r})|^4 \right] \ , \\ H_{12} &= -J_\perp \int d^2\mathbf{r} \left[\psi_1^*(\mathbf{r}) \psi_2(\mathbf{r}) + \psi_2^*(\mathbf{r}) \psi_1(\mathbf{r}) \right] \ . \end{aligned} \tag{2.61}$$

To establish a mapping between this bilayer Bose gas and the coupled 2D XY model, it is convenient to reconsider the low-energy effective theory. As seen in Section 2.3.5, the Hamiltonians H_a describe the physics of a standard XY model for each layer. The coupling term, H_{12}, can be simplified by adopting the density-phase representation for the fields, $\psi_a(\mathbf{r}) = \sqrt{n_a(\mathbf{r})} e^{i\phi_a(\mathbf{r})}$. In the regime of strongly suppressed density fluctuations, where the density in each layer can be approximated as a constant, $n_a(\mathbf{r}) \approx n$, the coupling Hamiltonian reduces to

$$H_{12} \approx -2nJ_\perp \int d^2r \cos\left(\phi_1(\mathbf{r}) - \phi_2(\mathbf{r})\right) \ , \tag{2.62}$$

here we have assumed both layers have the same density. This explicitly shows that the low-energy physics of the tunnelling interaction is governed by the relative phase between the two condensates, and energetically favors phase difference of zero (phase-locking). Combining the low-energy effective Hamiltonians for each layer with the interlayer coupling term, we arrive at the total effective Hamiltonian for the bilayer system

$$\begin{aligned} H &\approx \frac{\hbar^2 n}{2m} \int (\nabla \phi_1(\mathbf{r}))^2 d^2r + \frac{\hbar^2 n}{2m} \int (\nabla \phi_2(\mathbf{r}))^2 d^2r - 2nJ_\perp \int d^2r \cos\left(\phi_1(\mathbf{r}) - \phi_2(\mathbf{r})\right) \\ &= \frac{\hbar^2 n}{4m} \int (\nabla \theta(\mathbf{r}))^2 d^2r + \frac{\hbar^2 n}{4m} \int (\nabla \varphi(\mathbf{r}))^2 d^2r - 2nJ_\perp \int d^2r \cos\left(\theta(\mathbf{r})\right) \ , \end{aligned} \tag{2.63}$$

where we have defined the relative phase $\theta(\mathbf{r}) = \phi_1(\mathbf{r}) - \phi_2(\mathbf{r})$ and common phase $\varphi(\mathbf{r}) = \phi_1(\mathbf{r}) + \phi_2(\mathbf{r})$. We can see that it is mathematically equivalent to the continuum Hamiltonian for the coupled 2D XY model, as previously shown in Eq. (2.31). This equivalence demonstrates that, in the low-energy limit, the bilayer 2D Bose gas is a physical realization of the coupled 2D XY model.

To quantify the influence of a finite interlayer coupling on both the symmetric and antisymmetric modes, we numerically integrate the renormalization-group

equations originally introduced in Ref [13, 30]. These flow equations are derived from the Sine–Gordon formulation of two coupled 2D superfluids, which provides an effective description of the bilayer XY model. The RG equations are given by

$$\begin{aligned}
\frac{\mathrm{d}J_\perp}{\mathrm{d}l} &= \left(2 - \frac{T}{2\pi J_\mathrm{a}}\right) J_\perp \,, \\
\frac{\mathrm{d}A_\mathrm{s}}{\mathrm{d}l} &= \left(2 - 2\pi\frac{J_\mathrm{s}}{T}\right) A_\mathrm{s} + \alpha_3 \frac{A_1^2\,(J_\mathrm{a} - J_\mathrm{s})}{2T^2} \,, \\
\frac{\mathrm{d}A_\mathrm{a}}{\mathrm{d}l} &= \left(2 - 2\pi\frac{J_\mathrm{a}}{T}\right) A_\mathrm{a} + \alpha_3 \frac{A_1^2\,(J_\mathrm{s} - J_\mathrm{a})}{2T^2} \,, \\
\frac{\mathrm{d}A_1}{\mathrm{d}l} &= \left[2 - \frac{\pi\,(J_\mathrm{s} + J_\mathrm{a})}{2T} + \alpha_3 \frac{A_\mathrm{s}J_\mathrm{s} + A_\mathrm{a}J_\mathrm{a}}{T^2}\right] A_1 \,, \\
\frac{\mathrm{d}J_\mathrm{a}}{\mathrm{d}l} &= \alpha_2 \left[\frac{J_\perp^2}{4\pi^4 J_\mathrm{a}} - 4\frac{A_\mathrm{a}^2}{T^4} J_\mathrm{a}^3 - \frac{A_1^2}{2T^4}\,(J_\mathrm{s} + J_\mathrm{a})\,J_\mathrm{a}^2\right] \,, \\
\frac{\mathrm{d}J_\mathrm{s}}{\mathrm{d}l} &= -\alpha_2 \left[2\frac{A_\mathrm{s}^2}{T^4} J_\mathrm{s}^2 + \frac{A_1^2}{4T^4}\,(J_\mathrm{s} + J_\mathrm{a})\,J_\mathrm{s}\right] 2J_\mathrm{s} \,.
\end{aligned} \tag{2.64}$$

$J_{\mathrm{s/a}} = J \pm J_\mathrm{int}$ is the stiffness of symmetric (common) and antisymmetric (relative) modes, where J_int quantifies the energy splitting between these modes. Such a splitting naturally arises from density–density contact interactions in the bilayer Bose gas. The phase diagram can be obtained by numerically integrating the RG equations [13, 14], and the result is shown in Figure 2.7. This analysis reveals three distinct phases:

- **Normal:** Both the common and relative sectors are in the disordered phase.
- **Antisymmetric Superfluid (ASF):** The relative sector is ordered (superfluid), while the common sector remains disordered.
- **BSF Bilayer Superfluid (BSF):** Both the common and relative sectors are in the ordered (superfluid) phase.

A recent experiment has confirmed the existence of the BSF phase [14], whereas the ASF phase remains unexplored due to the limited range of coupling strengths accessible.

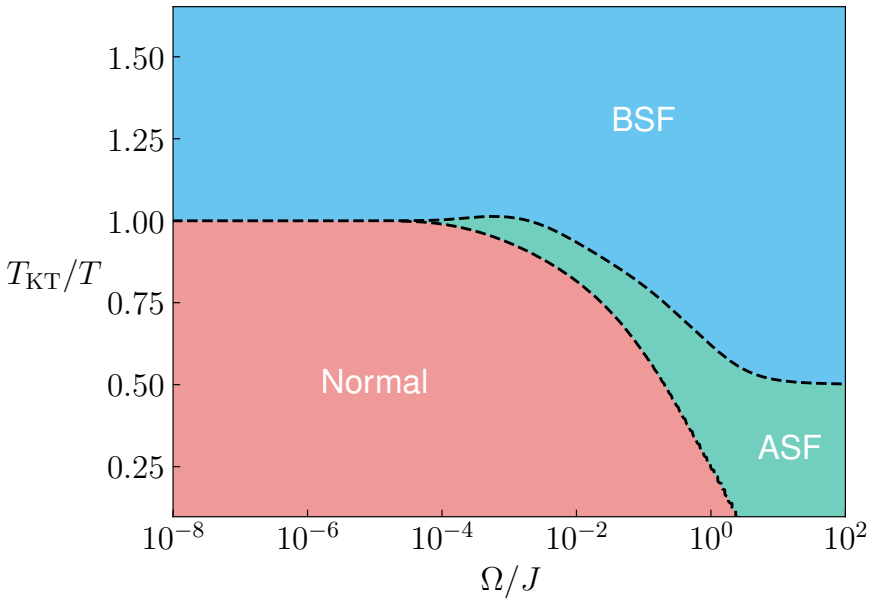

Figure 2.7: Phase Diagram for coupled bilayer 2D Bose gas. The three phases are obtained from the renormalization group (RG) equations given in Eq. (2.64). The red region denotes the normal phase, in which both the relative and common sectors are disordered. The green region corresponds to the atomic superfluid (ASF) phase, where only the relative sector is ordered, while the blue region indicates the paired (bond) superfluid (BSF) phase, in which both sectors are ordered. Both axes are expressed in dimensionless variables: T_{KT}/T and Ω/J, where $\Omega = 2J_{\perp}$ denotes the interlayer coupling strength, equivalent to the coupling in the 2D XY model (see Eq. (2.31)), and $J = 2T_{\mathrm{KT}}/\pi$ is the phase stiffness of each individual layer. The critical temperature for common phase is reduced by a factor of two compared to the decoupled case when $\Omega/J \gg 1$, in agreement with theoretical expectations. The horizontal axis is shown on a logarithmic scale.

3

Numerical Simulation of Bilayer 2D Bose Gases

Contents

In this chapter, we focus on the numerical techniques employed to investigate bilayer two-dimensional Bose gases. The stochastic Ornstein–Uhlenbeck framework is first introduced as a tool for modeling a single 2D Bose gas, and we show

how it can be adapted to describe the relative phase of tunnel-coupled bilayers at low temperature. We then turn to Monte Carlo methods within the classical-field approximation, which allow us to explore equilibrium properties of coupled bilayers with both two-body and four-body interlayer interactions. In the final part of the chapter,we present a method that combines Monte Carlo sampling with the Gross–Pitaevskii equations to simulate nonequilibrium dynamics at finite temperature, which we apply to investigate Josephson effects in two dimensions, revealing nontrivial behavior.[1]

3.1 Stochastic Process Modeling of 2D Bose Gases

3.1.1 Stochastic Ornstein-Uhlenbeck process

The Ornstein–Uhlenbeck (OU) process is one of the most widely studied continuous-time stochastic processes, originally introduced to model the velocity of a Brownian particle subject to friction [50]. The general form of an OU process for a variable $x(t)$ is given by

$$\frac{d}{dt}x(t) = -\kappa\, x(t) + \sigma N(0,1)\ , \tag{3.1}$$

where $N(0,1)$ denotes Gaussian white noise with zero mean and unit variance, uncorrelated at different times. The parameters κ and σ characterize the deterministic relaxation rate and the strength of the stochastic forcing, respectively. Much is known about OU processes; for example, if the mean of $x(t)$ is zero, the autocorrelation function decays exponentially as

$$\langle x(0)x(t)\rangle = \frac{\sigma^2}{2\kappa}\, e^{-\kappa t}\ , \qquad t > 0\ , \tag{3.2}$$

illustrating the characteristic timescale of memory loss in the system. Therefore, an OU process can be employed to model a system by determining the parameters κ and σ such that Eq. (3.2) accurately reproduces the correlation function of the physical quantity of interest.

[1] Both the Monte Carlo and Gross–Pitaevskii equation solvers are implemented in `Rust` to optimize CPU performance [48]. In addition, GPU-accelerated versions of both solvers are implemented in `C++`, optimized for CUDA-based execution [49].

These values of the two OU parameters are then used to generate an ensemble of $x(t)$ profiles using the exact updating formula [51]

$$x(t+\Delta t) = x(t)e^{-\kappa\Delta t} + \sqrt{\frac{\sigma^2}{2\kappa}\left[1-e^{-2\kappa\Delta t}\right]}\, N(0,1)\ . \tag{3.3}$$

3.1.2 Stochastic description of two coupled 1D Bose gases

It is well established that Ornstein–Uhlenbeck stochastic processes provide an effective description of phase fluctuations in one-dimensional (1D) quasicondensates at finite temperature. In this regime, density fluctuations are strongly suppressed by interactions, and the dominant excitations are long-wavelength phase modes, which can be modeled as Gaussian random fields with exponentially decaying correlations. Both theoretical analyses and experiments on tunnel-coupled 1D Bose gases have demonstrated that the relative phase evolution along the longitudinal direction can be mapped onto an OU process, where the spatial coordinate z plays the role of time in the OU updates, and the characteristic correlation length is set by the interplay between thermal fluctuations and tunnel coupling [52, 53].

The classical field Hamiltonian for the two tunnel-coupled 1D condensates is [54]

$$H = \int dz \left[\sum_{j=1}^{2}\left(\frac{\hbar^2}{2m}\frac{\partial\psi_j^*}{\partial z}\frac{\partial\psi_j}{\partial z} + g\psi_j^*\psi_j^*\psi_j\psi_j\right) - \hbar J_{\rm c}\left(\psi_1^*\psi_2 + \psi_2^*\psi_1\right)\right]. \tag{3.4}$$

In the density-phase representation the macroscopic wave functions of the two condensates can be written as

$$\psi_j(z) = \sqrt{n}_j e^{-i\phi_j(r)}, \quad j = 1,2\ . \tag{3.5}$$

Neglecting density fluctuations at low temperature, as they are suppressed by the contact interaction term, and expanding around small phase fluctuations, the Hamiltonian in Eq. 3.4 can be linearised and expressed in terms of the symmetric and antisymmetric components of the relative phase, $\varphi(z) = [\phi_1(z) + \phi_2(z)]/2$ and $\theta(z) = \phi_1(z) - \phi_2(z)$. The linearised Hamiltonian is [54]

$$H_{\rm lin} = \int dz \left[\frac{\hbar^2 n_{\rm 1D}}{m}\left(\frac{\partial\varphi}{\partial z}\right)^2 + \frac{\hbar^2 n_{\rm 1D}}{4m}\left(\frac{\partial\theta}{\partial z}\right)^2 + \hbar J_{\rm c} n_{\rm 1D}\theta^2\right]. \tag{3.6}$$

Discretizing the linearised Hamiltonian for the antisymmetric sector on a lattice of M sites with spacing Δz gives

$$H_{\mathrm{a}} = \sum_{j=1}^{M} \frac{\hbar^2 n_{1\mathrm{D}}}{4m\Delta z} \left(\theta_j - \theta_{j+1}\right)^2 + \hbar J_{\mathrm{c}} n_{1\mathrm{D}} \Delta z \, \theta_j^2 \,, \tag{3.7}$$

where periodic boundary conditions are imposed. The phase correlations of the antisymmetric component (i.e., the relative phase) can then be shown to decay as [55]

$$\langle \theta(0)\, \theta(z) \rangle = \frac{k_B T}{2 n_{1\mathrm{D}} \hbar^2} \sqrt{\frac{\hbar m}{J_{\mathrm{c}}}}\, e^{-2|z|\sqrt{m J_{\mathrm{c}}/\hbar}} \,. \tag{3.8}$$

By comparison with Eq. (3.2), one can identify the effective OU parameters as $\sigma^2/2 = m k_B T/(\hbar^2 n_{1\mathrm{D}})$ and $\kappa = 2\sqrt{m J_{\mathrm{c}}/\hbar}$. These expressions provide the input for generating relative-phase profiles of coupled 1D condensates within the OU stochastic framework (see Eq. (3.3)).

3.1.3 Stochastic description of 2D Bose Gases

The extension of the Ornstein–Uhlenbeck description to two dimensions was first formulated by Igor Mazets [56], starting from the linearised 2D Hamiltonian in the superfluid phase. Neglecting density fluctuations, the field operator can be written as $\psi(\mathbf{r}) \simeq \sqrt{n_{2\mathrm{D}}(\mathbf{r})}\, e^{-i\phi(\mathbf{r})}$, and the linearised Hamiltonian is given by

$$H = \frac{\hbar^2}{2m} \int d^2 r \, n_{2\mathrm{D}} \left(\nabla \phi\right)^2 \,, \tag{3.9}$$

where ∇ is the 2D gradient operator in the (x, y) plane. Discretizing this Hamiltonian on a $(2M+1) \times (2M+1)$ lattice with spacing Δs leads to the partition function [56]

$$\mathcal{Z} = \text{const.} \prod_{l_x=-M}^{M} \prod_{l_y=-M}^{M} \int d\phi_{l_x,l_y} \exp\Bigg\{ -\frac{\epsilon}{2} \omega_{l_x,l_y} \times \Big[\left(\phi_{l_x,l_y} - \phi_{l_x,l_y-1}\right)^2 + \left(\phi_{l_x,l_y} - \phi_{l_x-1,l_y}\right)^2 \Big] \Bigg\} \,, \tag{3.10}$$

where $\omega_{l_x,l_y} = n_{2\mathrm{D}}(l_x \Delta s, l_y \Delta s)/n_{2\mathrm{D}}(0,0)$ encodes the normalized density distribution, and $\epsilon = \hbar^2 n_{2\mathrm{D}}(0,0)/(m k_B T)$ is a dimensionless fluctuation parameter. Periodic boundary conditions are assumed, and the density is taken to vary slowly along

the x direction over the grid spacing Δs so that $\omega_{l_x,l_y}/\omega_{l_x,0} \approx \omega_{l_x-1,l_y}/\omega_{l_x-1,0}$. We rewrite the expression by introducing $R_{l_x,l_y} = \omega_{l_x,l_y}/\omega_{l_x,0}$ and write

$$\begin{aligned}&\sum_{l_x}\sum_{l_y} -\frac{\epsilon}{2}\omega_{l_x,l_y} \times \left[(\phi_{l_x,l_y} - \phi_{l_x,l_y-1})^2 + (\phi_{l_x,l_y} - \phi_{l_x-1,l_y})^2\right] \\ =&\sum_{l_x}\sum_{l_y} -\frac{\epsilon_{l_x}}{2}R_{l_x,l_y} \times \left[(\phi_{l_x,l_y} - \phi_{l_x,l_y-1})^2 + (\phi_{l_x,l_y} - \phi_{l_x-1,l_y})^2\right] \ ,\end{aligned} \tag{3.11}$$

where $\epsilon_{l_x} = \epsilon \times \omega_{l_x,0}$. It is useful to express the sums using matrix notation

$$\begin{aligned}&\textstyle\sum_{l_y=-M}^{M} R_{l_x,l_y}(\phi_{l_x,l_y} - \phi_{l_x,l_y-1})^2 \\ &= R_{l_x,-M}(\phi_{l_x,-M}^2 + 2\phi_{l_x,-M}\phi_{l_x,M} + \phi_{l_x,M}^2) \\ &\qquad + R_{l_x,-M+1}(\phi_{l_x,-M+1}^2 + 2\phi_{l_x,-M+1}\phi_{l_x,-M} + \phi_{l_x,-M}^2) \\ &\qquad + \cdots \\ &= \begin{pmatrix} \phi_{l_x,-M} \\ \phi_{l_x,-M+1} \\ \phi_{l_x,-M+2} \\ \vdots \\ \phi_{l_x,M} \end{pmatrix}^T \begin{pmatrix} R_{l_x,-M}+R_{l_x,-M+1} & -R_{l_x,-M+1} & 0 & \cdots & 0 & -R_{l_x,M} \\ -R_{l_x,-M+1} & R_{l_x,-M+1}+R_{l_x,-M+2} & -R_{l_x,-M+2} & \cdots & 0 & 0 \\ 0 & -R_{l_x,-M+2} & \ddots & \ddots & \vdots & \vdots \\ \vdots & \vdots & \ddots & \ddots & -R_{l_x,M-1} & 0 \\ 0 & 0 & \cdots & -R_{l_x,M-1} & R_{l_x,M-1}+R_{l_x,M} & -R_{l_x,M} \\ -R_{l_x,M} & 0 & \cdots & 0 & -R_{l_x,M} & R_{l_x,M}+R_{l_x,-M} \end{pmatrix} \begin{pmatrix} \phi_{l_x,-M} \\ \phi_{l_x,-M+1} \\ \phi_{l_x,-M+2} \\ \vdots \\ \phi_{l_x,M} \end{pmatrix} \\ &= \boldsymbol{\phi}_{l_x}^T \boldsymbol{M}_{l_x} \boldsymbol{\phi}_{l_x} \ ,\end{aligned} \tag{3.12}$$

where $\boldsymbol{M}_{l_x}$ is a symmetric tridiagonal matrix with additional corner elements arising from the periodic boundary conditions. Its eigendecomposition can be written as

$$\boldsymbol{M}_{l_x} = \boldsymbol{V}_{l_x} \boldsymbol{J}_{l_x} \boldsymbol{V}_{l_x}^T \ , \tag{3.13}$$

where $\boldsymbol{J}_{l_x}$ is diagonal matrix and $\boldsymbol{V}_{l_x}$ is orthogonal matrix. In this basis, we can introduce the transformed vector $\boldsymbol{A}_{l_x} = \boldsymbol{V}_{l_x}^T \boldsymbol{\varphi}_{l_x}$, the quadratic form in Eq. (3.12) then becomes

$$\boldsymbol{\varphi}_{l_x}^T \boldsymbol{M}_{l_x} \boldsymbol{\varphi}_{l_x} = \boldsymbol{\varphi}_{l_x}^T \boldsymbol{V}_{l_x} \boldsymbol{J}_{l_x} \boldsymbol{V}_{l_x}^T \boldsymbol{\varphi}_{l_x} = \boldsymbol{A}_{l_x}^T \boldsymbol{J}_{l_x} \boldsymbol{A}_{l_x} \ , \tag{3.14}$$

with the inverse relation $\boldsymbol{\varphi}_{l_x} = \boldsymbol{V}_{l_x} \boldsymbol{A}_{l_x}$.

Diagonalisation factorises the partition function in Eq. (3.10) to

$$Z = \text{const.} \prod_{j=0}^{2M} Z_j \ , \tag{3.15}$$

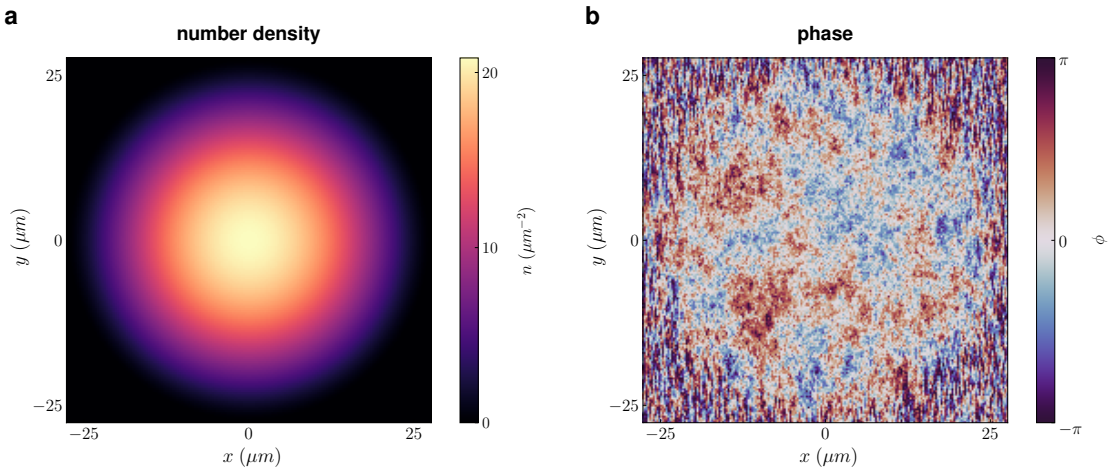

Figure 3.1: 2D phase generation via Ornstein–Uhlenbeck process. (**a**) Two-dimensional Thomas–Fermi density distribution on a $(2M+1)\times(2M+1)$ grid. (**b**) A typical two-dimensional phase profile generated using the stochastic OU process.

which is the product of contributions from each of the modes j, given by

$$Z_j = \prod_{l_x=-M}^{M} \int dA_{l_x,j}\ \exp\left[-\frac{\epsilon_{l_x}}{2}\Big(A_{l_x-1,j} - A_{l_x,j}\Big)^2 - \frac{\epsilon_{l_x} J_{l_x,j}}{2}\, A_{l_x,j}^2\right]. \tag{3.16}$$

Interestingly, this expression has the same structure as the discretised 1D Hamiltonian in Eq. (3.7). By direct analogy with the 1D mapping,[2] we therefore arrive at the iterative update rule for $A_{l_x,j}$

$$A_{l_x,j} = A_{l_x-1,j}\, e^{-\sqrt{J_{l_x,j}}} + \sqrt{\frac{1-e^{-2\sqrt{J_{l_x,j}}}}{2\,\epsilon_{l_x}\sqrt{J_{l_x,j}}}}\, N(0,1)\ . \tag{3.17}$$

The central line $l_x = 0$ can be initialized by

$$\left\langle A_{l_x,j}^2 \right\rangle = \frac{1}{2\,\epsilon_{l_x}\sqrt{J_{l_x,j}}}\ , \tag{3.18}$$

which is consistent with the OU correlation function in Eq. (3.2). Starting from this initialization, the recursive update Eq. (3.17) generates the full 2D phase profile. Finally, the inverse transformation $\boldsymbol{\varphi}_{l_x} = \boldsymbol{V}_{l_x}\boldsymbol{A}_{l_x}$ recovers the physical phase fields.

We find that the generation of 2D phase profiles using the OU stochastic process depends explicitly on the underlying density distribution. For any prescribed density

[2] An insightful way to view this mapping between 2D and 1D is to regard the 2D cloud as a collection of coupled 1D systems. This perspective is reflected in the mapping $J_{l_x,j} \propto J_{\mathrm{c,1D}}(\Delta z)^2$, which captures the effective coupling between neighboring 1D chains.

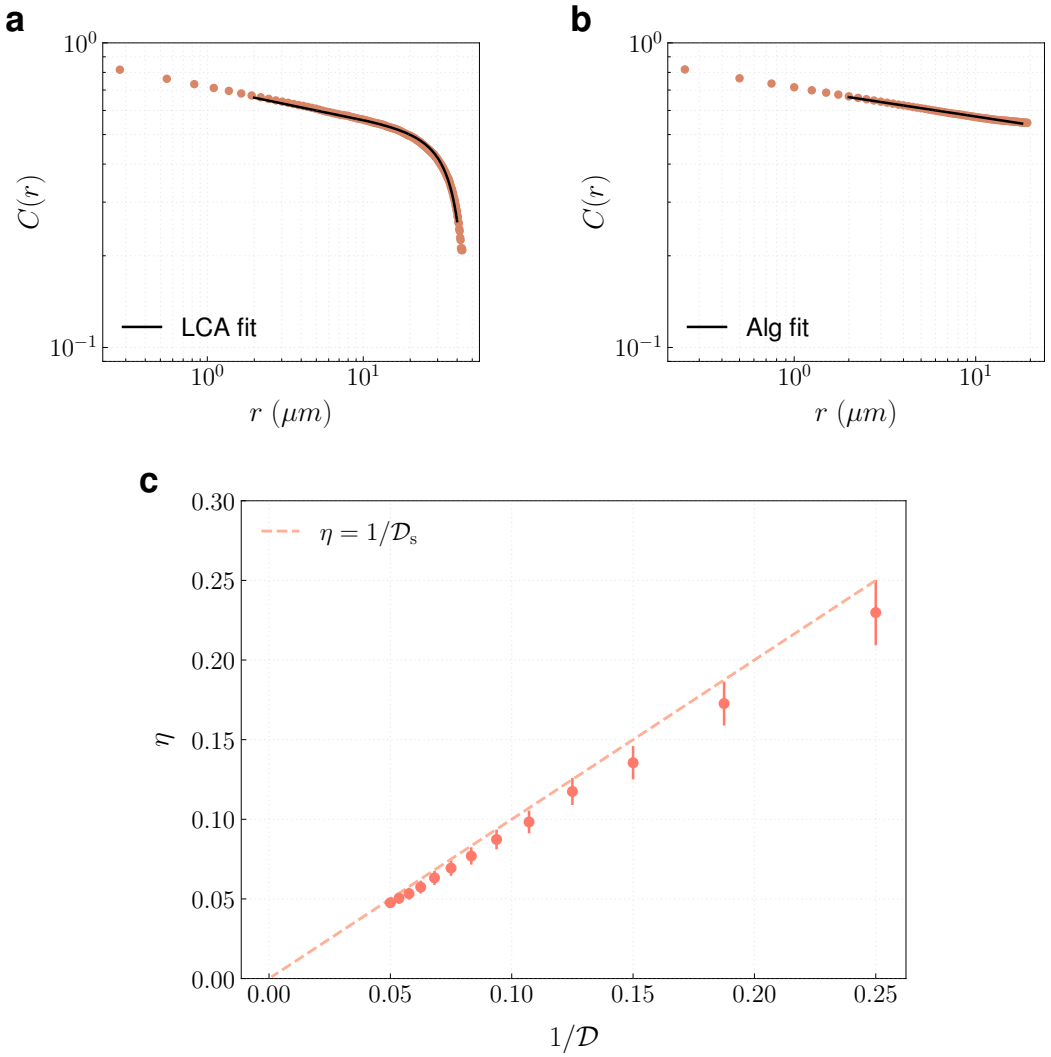

Figure 3.2: Phase correlation function analysis of the Ornstein–Uhlenbeck process. (**a**) Phase correlation function $C(r)$ obtained from 2000 OU generated phase profiles using a Thomas–Fermi (TF) density distribution. The solid line shows a local correlation approximation (LCA) fit based on the TF profile. (**b**) Phase correlation function $C(r)$ obtained from 2000 OU generated phase profiles with a uniform density distribution. The solid line corresponds to a power-law (algebraic) fit. (**c**) Each marker (with error bars) is extracted from 2000 OU generated phase profiles with uniform density. The dashed line indicates the expected relation between the superfluid exponent η and the reciprocal of the superfluid phase-space density $\mathcal{D}_s$.

profile, the corresponding phase configuration can be constructed efficiently. The OU approach is substantially faster than alternative numerical methods, such as the classical-field Monte Carlo (MC) technique which we will discuss later. However, it is important to remember that stochastic OU method omits density fluctuations that persist even in the superfluid phase of a weakly interacting 2D system, and

it cannot simulate vortices because the linearised (Gaussian) Hamiltonian used to derive the updates is not able to describe the vortex core. Therefore, this stochastic approach is unable to capture the BKT transition, the phase correlation function is always algebraic for a homogeneous system.

Figure 3.1 shows a typical two-dimensional phase profile generated via the OU method for a Thomas–Fermi density distribution. In Figure 3.2, we present the phase correlation function,

$$C(r) = \left\langle \exp\left[i\Big(\phi(\mathbf{r}) - \phi(\mathbf{r}')\Big)\right]\right\rangle \ , \quad r = |\mathbf{r} - \mathbf{r}'| \ , \tag{3.19}$$

obtained by averaging over 2000 independently generated OU phase profiles for both homogeneous and inhomogeneous gases. By varying the PSD through changes in the atom number while keeping the temperature fixed, we find that the correlation function follows

$$C(r) \propto r^{-1/(2\pi\epsilon)} = r^{-mk_BT/(2\pi\hbar^2 n_{2\mathrm{D}})} \ , \tag{3.20}$$

as expected for a two-dimensional superfluid. Comparing the exponent with Eq. (2.55) shows that $n_{2\mathrm{D}} = n_{\mathrm{s}}$ in the OU simulations, which follows naturally from the correspondence between the linearised Hamiltonian in Eq. (3.9) and the Hamiltonian in Eq. (2.52). This identification is evidenced by the agreement between $\eta(\mathcal{D})$ from simulations and the prediction $\eta = 1/\mathcal{D}_{\mathrm{s}}$, as shown in Figure 3.2c.

3.1.4 Stochastic description of tunnel-coupled 2D Bose Gases

Here we demonstrate that the Ornstein–Uhlenbeck stochastic description of a 2D Bose gas can be naturally extended to account for the relative phase fluctuations of a tunnel-coupled 2D system. In close analogy with the 1D tunnel-coupled case (see Eq. (3.6)), the linearised Hamiltonian for the relative sector reads

$$H_{\mathrm{lin}} = \int d^2r \left[\frac{\hbar^2 n_{2\mathrm{D}}}{4m} \left(\nabla\theta\right)^2 + \hbar J_{\mathrm{c}} n_{2\mathrm{D}} \theta^2 \right] \ , \tag{3.21}$$

where the coupling term arises from expanding $\cos(\theta)$ to quadratic order. Upon discretisation, the corresponding partition function takes the form

$$\mathcal{Z} = \text{const.} \prod_{l_x=-M}^{M} \prod_{l_y=-M}^{M} \int d\theta_{l_x,l_y} \exp\Bigg\{ -\frac{\epsilon}{4}\,\omega_{l_x,l_y}\Big[(\theta_{l_x,l_y}-\theta_{l_x,l_y-1})^2 + (\theta_{l_x,l_y}-\theta_{l_x-1,l_y})^2 - \frac{4m\Delta s^2}{\hbar} J_{\mathrm{c}}\,\theta_{l_x,l_y}^2\Big]\Bigg\}\,. \tag{3.22}$$

After diagonalisation, we obtain the partition function factorises into independent contributions from each mode j,

$$Z_j = \prod_{l_x=-M}^{M} \int dA_{l_x,j}\ \exp\left[-\frac{\epsilon_{l_x}}{4}\Big(A_{l_x-1,j}-A_{l_x,j}\Big)^2 - \frac{\epsilon_{l_x}}{4}\left(J_{l_x,j}+\frac{4m\Delta s^2}{\hbar}J_{\mathrm{c}}\right)A_{l_x,j}^2\right]. \tag{3.23}$$

A direct comparison with Eq. (3.16) yields the iterative update rule

$$A_{l_x,j} \;=\; A_{l_x-1,j}\,e^{-\sqrt{J'_{l_x,j}}} + \sqrt{\frac{1-e^{-2\sqrt{J'_{l_x,j}}}}{2\,\epsilon'_{l_x}\sqrt{J'_{l_x,j}}}}\,\mathcal{N}(0,1)\,, \tag{3.24}$$

with effective parameters

$$J'_{l_x,j} = J_{l_x,j} + \frac{4m}{\hbar}\,\Delta s^2 J_{\mathrm{c}}\,, \qquad \epsilon'_{l_x} = \frac{\epsilon_{l_x}}{2}\,. \tag{3.25}$$

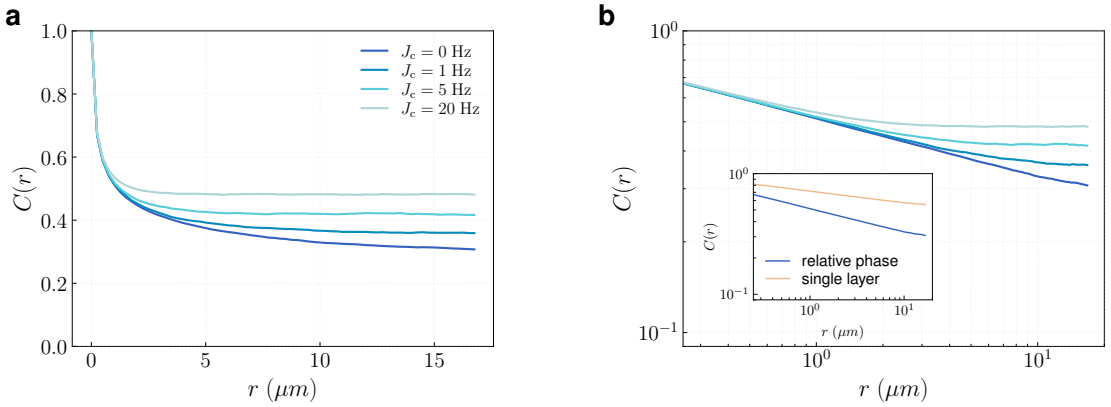

Figure 3.3: Coupled gas phase correlations from Ornstein–Uhlenbeck simulations. (**a**) Phase correlation function of the relative phase at phase-space density $\mathcal{D} = 10$ for different interlayer coupling strengths J_{c} in a uniform system. (**b**) Same data shown on a log–log scale. The inset compares the correlation functions of the single-layer phase and the relative phase in the decoupled case.

We now find that the update rule depends explicitly on the lattice spacing Δs, similar to the 1D case. In the absence of interlayer coupling ($J_c = 0$), the update rule reduces to Eq. (3.17), but with $\epsilon'_{l_x} = \epsilon_{l_x}/2$. This modification arises because we are considering the relative phase, for which the correlation function satisfies $C_{\text{rel}}(r) = C^2_{\text{layer}}(r)$ (see Section 2.2.3).

The simulation results are shown in Figure 3.3. For finite interlayer coupling ($J_c \neq 0$), the correlation function initially decays algebraically before saturating at a finite value, indicating that interlayer coupling establishes long-range order (LRO) in the relative phase, as expected for a uniform system.

We note that the existence of vortices is again not captured by the OU method. In addition, the OU simulation is used to simulate the phase fluctuation so that the global phase is not well simulated, it always returns a phase profile with $\langle\theta\rangle \approx 0$. Therefore, it is not valid to check the phase distribution with the OU method.

3.2 Classical-Field Monte Carlo Simulations

Although the stochastic Ornstein–Uhlenbeck process provides a fast method for simulating phase fluctuations in 2D, it neglects density fluctuations and the thermal component of the system, and it cannot capture vortex excitations. To investigate the system's properties, particularly the BKT transition, we thus need to turn to other numerical methods. Among these, Classical-Field Monte Carlo (MC) simulations provide a powerful and well-established approach. This method is particularly effective for determining thermodynamic quantities and was instrumental in the early theoretical predictions of the critical phase-space density, $\mathcal{D}_c$, for the BKT transition in a weakly-interacting 2D Bose gas [57]. The core of this approach lies in the classical-field approximation, where the bosonic field operators, $\hat{\Psi}(\mathbf{r})$, in the many-body Hamiltonian are replaced by complex numbers, $\psi(\mathbf{r})$. This is a valid approximation in the regime of high occupation numbers where quantum fluctuations are suppressed. In this section, we focus on classical-field MC simulations based on the Metropolis algorithm, first introduced by Metropolis et al. in 1953 [58].

We show that this approach successfully captures a wide range of fundamental properties of the bilayer 2D Bose gas.

3.2.1 BKT transition in 2D Bose gases

Within the classical-field approximation, the system is governed by the Hamiltonian

$$H = \int d^2r \left[\frac{\hbar^2}{2m} |\nabla\psi(\mathbf{r})|^2 + \frac{g}{2}|\psi(\mathbf{r})|^4 + V(\mathbf{r})|\psi(\mathbf{r})|^2 \right] , \tag{3.26}$$

where $V(\mathbf{r})$ denotes the external trapping potential. To facilitate Monte Carlo simulations, the kinetic term can be rewritten using Green's identity, yielding

$$H = \int d^2r \left[-\frac{\hbar^2}{2m} \psi^*(\mathbf{r})\nabla^2\psi(\mathbf{r}) + \frac{g}{2}|\psi(\mathbf{r})|^4 + V(\mathbf{r})|\psi(\mathbf{r})|^2 \right] . \tag{3.27}$$

The Hamiltonian is discretised on a two–dimensional square lattice and written in grand-canonical form

$$H = -J_{\mathrm{h}} \sum_{i \neq j} w_{i,j} \psi_i^* \psi_j + \frac{U}{2} \sum_i n_i^2 + \sum_i (V_i - \mu)\, n_i \ , \tag{3.28}$$

where $\psi_i \in \mathbb{C}$ is the order-parameter field at site i. $J_{\mathrm{h}} = \hbar^2/(2ml^2)$ is the hopping energy and $U = g/l^2$ is the repulsive interaction energy, where m is the mass and l is the discretization length; $n_i = |\psi_i|^2$ is the local density. The interaction $g = \tilde{g}\hbar^2/m$ is given in terms of the dimensionless parameter $\tilde{g} = \sqrt{8\pi}a_{\mathrm{s}}/\ell_{\mathrm{z}}$, where m is the mass, a_{s} is the s-wave scattering length and $\ell_{\mathrm{z}} = \sqrt{\hbar/(m\omega_{\mathrm{z}})}$ is the harmonic oscillator length in the axial direction. $w_{i,j} = w_{j,i}$ are the symmetric stencil weights of the discrete Laplacian, the central contribution $w_{i,i}\psi_i^*\psi_i = w_{i,i}\, n_i$ is absorbed into the chemical potential μ. If we employ the 5-point Laplacian (see Figure 3.4a), Eq. (3.28) reduces to the well-known discrete Bose–Hubbard form,

$$H = -J_{\mathrm{h}} \sum_{\langle i,j \rangle} \Big(\psi_i^*\, \psi_j + \psi_j^*\, \psi_i \Big) + \frac{U}{2} \sum_i n_i^2 + \sum_i \Big(V_i - \mu \Big)\, n_i \ , \tag{3.29}$$

where the sum $\langle i, j \rangle$ runs over all nearest-neighbor pairs on the square lattice. However, the standard 5-point finite-difference approximation to the Laplacian is anisotropic: its leading truncation error is $\mathcal{O}(l^2)$ and is direction dependent, involving only fourth derivatives aligned with the x and y axes, consequently it

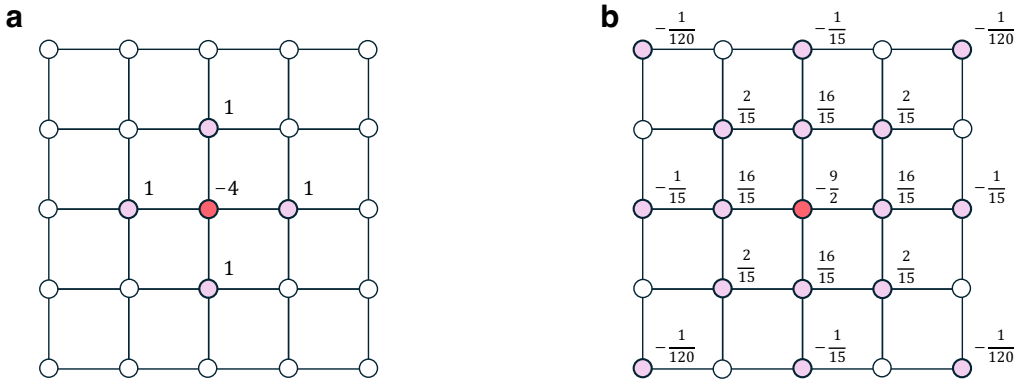

Figure 3.4: 5-point and 25-point finite-difference Laplacian stencils. (**a**) 5-point stencil. (**b**) 25-point stencil. Filled circles mark the stencil locations with nonzero coefficients. The central marker (red) denotes the target lattice site i.

breaks rotational invariance. Therefore, for the simulations presented in this thesis we employ a 25–point isotropic stencil whose leading truncation error is $\mathcal{O}(l^4)$, the stencil coefficients [59] are plotted in Figure 3.4b.

To simulate the equilibrium states of ψ, we consider a square lattice of 200×200 sites with a discretization length of $0.25\,\mu$m. V_i is chosen such that the simulated system yields a square, homogeneous density profile with a size of $49\,\mu$m. In approaching the continuum limit, the lattice spacing l is chosen to be smaller than or comparable to both the healing length and the thermal de Broglie wavelength, $\lambda = h/\sqrt{2\pi m k_{\mathrm{B}} T}$, where T is the temperature, k_{B} the Boltzmann constant, and h Planck's constant [44]. Sampling is performed within the grand-canonical ensemble at temperature T and chemical potential μ using a classical Metropolis algorithm. To match experimental conditions, we set $T = 30\,\mathrm{nK}$, $\tilde{g} = 0.098$ (corresponding to an axial trapping frequency $\omega_{\mathrm{z}} \sim 1.6\,\mathrm{kHz}$), and use the atomic mass of ^{87}Rb. We perform 7×10^5 update steps per site to thermalise the system, after which field configurations are sampled with an additional 5000 updates per site between successive samples in order to reduce autocorrelations in the generated states.[3]

[3]It is well known that the Metropolis algorithm suffers from critical slowing down near the BKT transition point [60]. Consequently, a large number of updates is required to sufficiently reduce autocorrelations between successive samples. Typically, 5000 updates per site are already sufficient to characterize the fluctuation properties of the system, although they are not enough

During the updates, the acceptance rate is maintained at approximately 30% by tuning the standard deviation σ of the proposal normal distribution at each step. The chemical potential μ is varied to control the total atom number N, thereby tuning the phase-space density $\mathcal{D} = n\lambda_{\mathrm{th}}^2$.

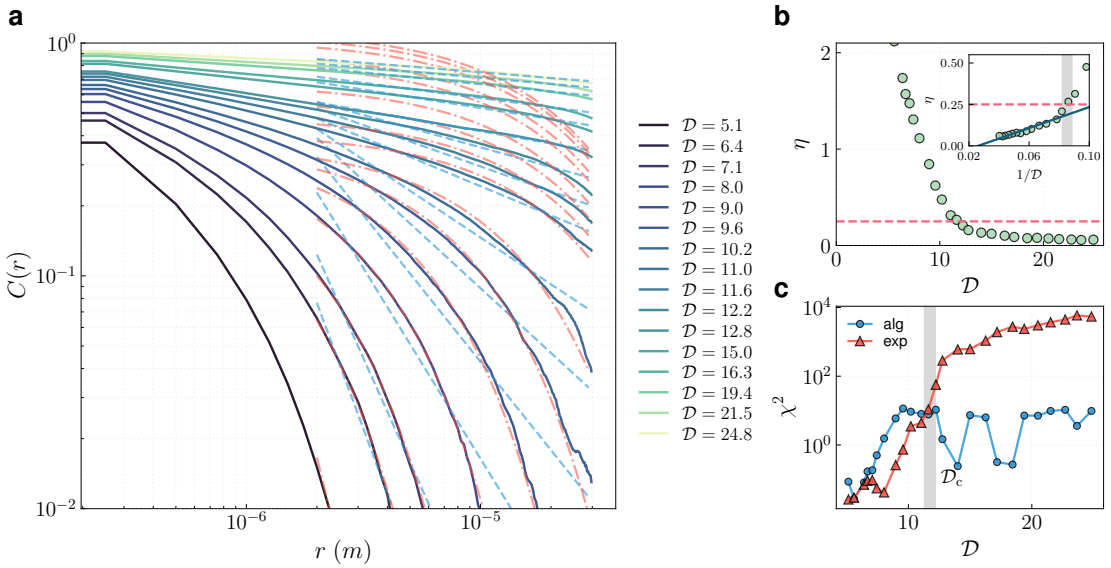

Figure 3.5: Phase correlation function and BKT transition. (**a**) Representative phase correlation functions $C(r)$ at different PSDs. Each dataset is fitted with an exponential model $y = ae^{-r/r_0}$ (red dash-dotted line) and an algebraic model $y = ar^{-\eta}$ (blue dashed line). (**b**) Extracted values of η as a function of PSD. The horizontal red dashed line marks $\eta_c = 0.25$, the universal critical exponent of the BKT transition. The inset shows the same data plotted against the reciprocal variable $1/\mathcal{D}$, where the blue solid line is a linear fit consistent with the Nelson–Kosterlitz relation $\eta \propto 1/\mathcal{D}$ in the thermodynamic limit. The black shaded area indicates the estimated critical PSD, $\mathcal{D}_c$, determined from the χ^2 analysis. (**c**) χ^2 statistics for exponential and algebraic fits, with the critical PSD $\mathcal{D}_c$ extracted from the crossover point.

We generate 200 samples and compute the phase of each field ψ, from which the phase correlation function $C(r)$ is obtained. The results are shown in Figure 3.5. The correlation function exhibits a clear transition from exponential to algebraic behavior, as confirmed by the χ^2 analysis, yielding a critical phase-space density of $\mathcal{D}_c \approx 11.8$. The superfluid exponent η, extracted from algebraic fits, shows good agreement with theoretical predictions and remains below 0.25 in the superfluid phase and shows linear relationship. We note that finite-size effects can reduce the

for complete decorrelation between samples.

critical value of η_c and broaden the transition region. η_c is expected to exhibit a logarithmic dependence on the system size L [61], given by

$$\eta_c\left(L/\xi\right) = \frac{\eta_c\left(L \to \infty\right)}{1 + \frac{1}{2}\frac{1}{\ln(L/\xi)+C}}\,, \tag{3.30}$$

where the length scale is normalized to the healing length ξ, and C is a non-universal parameter. In our finite-size simulations, the estimated critical superfluid exponent yields $\eta_c \approx 0.185$, in good agreement with previous results obtained for trapped finite-size systems [23, 62, 63].

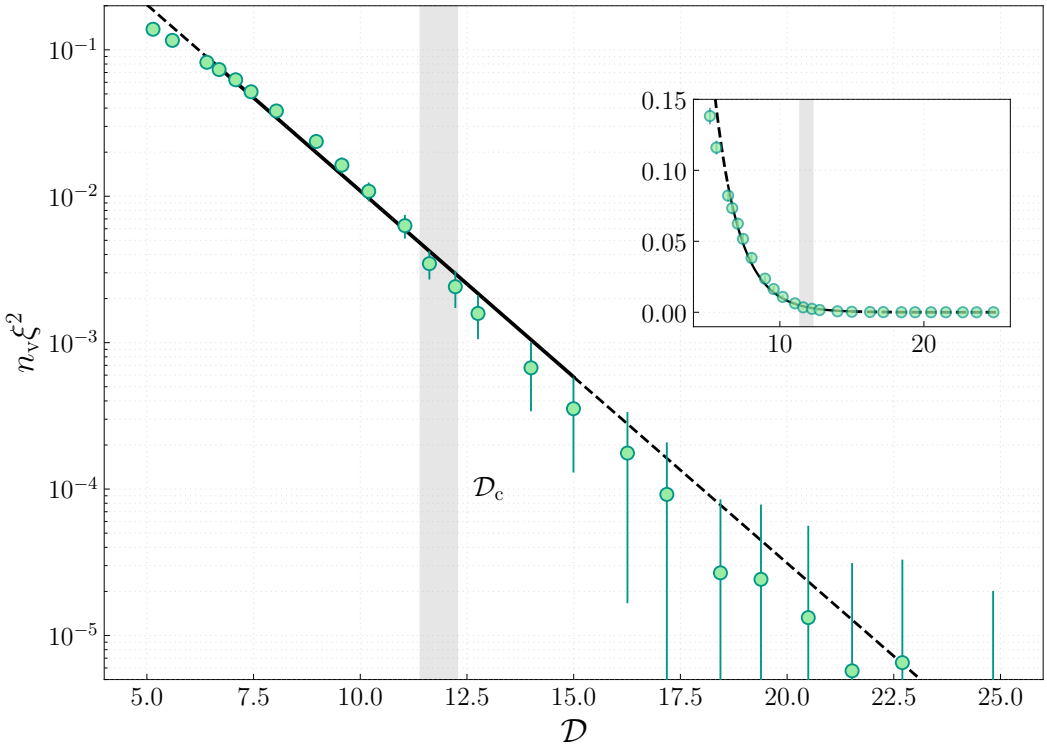

Figure 3.6: Vortex scaling across the BKT transition. Dimensionless vortex density $n_v\xi^2$ obtained from Monte Carlo simulations as a function of the phase-space density $\mathcal{D}$. The vertical axis is plotted on a logarithmic scale. The black line represents an exponential fit of the form $f(\mathcal{D}) = A\exp\left(-\gamma\mathcal{D}\right)$, with the solid segment indicating the fitting range. The inset shows the same data plotted on a linear scale.

Since the BKT transition is driven by the unbinding of vortex–antivortex pairs, increasing the temperature leads to the appearance of free vortices, whereas lowering the temperature favors their binding into pairs. Consequently, the density of free vortices is expected to decrease and eventually vanish as the phase-space density (PSD) increases.

In the simulations, vortices are identified by calculating the winding number of the phase around each plaquette (2×2) of the lattice. A circulation of $+2\pi$ is counted as a vortex, while a circulation of -2π is counted as an antivortex. Before counting the vortices, the fields are coarse grained by applying a Gaussian filter with width $\sigma = 1\,\mu$m, which effectively removes tightly bound vortex–antivortex pairs separated by distances smaller than σ [64]. The remained vortices are considered as free vortices, and the vortex density is then obtained by averaging over 200 samples for each PSD. The results are presented in Figure 3.6. We find that the vortex density decays exponentially, with $\gamma = 0.57(2)$, which is in close agreement with the value 0.56(5) reported in previous experiments [23, 62, 65].

3.2.2 Tunnel-coupled bilayer 2D Bose gases

We now turn to the bilayer two-dimensional Bose gas with Josephson tunneling between the layers. The system consists of two subsystems (labeled $a = 1, 2$) and is described by the discrete Hamiltonian

$$H = H_1 + H_2 + H_{12} \,, \tag{3.31}$$

with

$$H_a = -J_\mathrm{h} \sum_{i \neq j} w_{i,\,j}\, \psi^*_{a,\,i} \psi_{a,\,j} + \frac{U}{2} \sum_i n^2_{a,\,i} + \sum_i \left(V_i - \mu\right) n_{a,\,i} \,, \tag{3.32}$$

and

$$H_{12} = -J_\mathrm{c} \sum_i \left(\psi^*_{1,i} \psi_{2,i} + \psi^*_{2,i} \psi_{1,i} \right) \,, \tag{3.33}$$

where J_c denotes the Josephson coupling strength.

As discussed in Secs. 2.2.1 and 2.3.7, it is convenient to introduce the relative phase $\theta = \phi_1 - \phi_2$ and the common phase $\varphi = \phi_1 + \phi_2$. The simulations are performed in a $47\,\mu$m sized square box potential with discretization length of $0.5\,\mu$m using the same method described previously, with the coupling strength J_c varied from 10^{-6} to 100 Hz. The temperature is set to 50 nK and the dimensionless interaction strength to $\tilde{g} = 0.084$, in order to match the parameters used in Ref. [14]. A total of 150 samples is generated for the analysis.

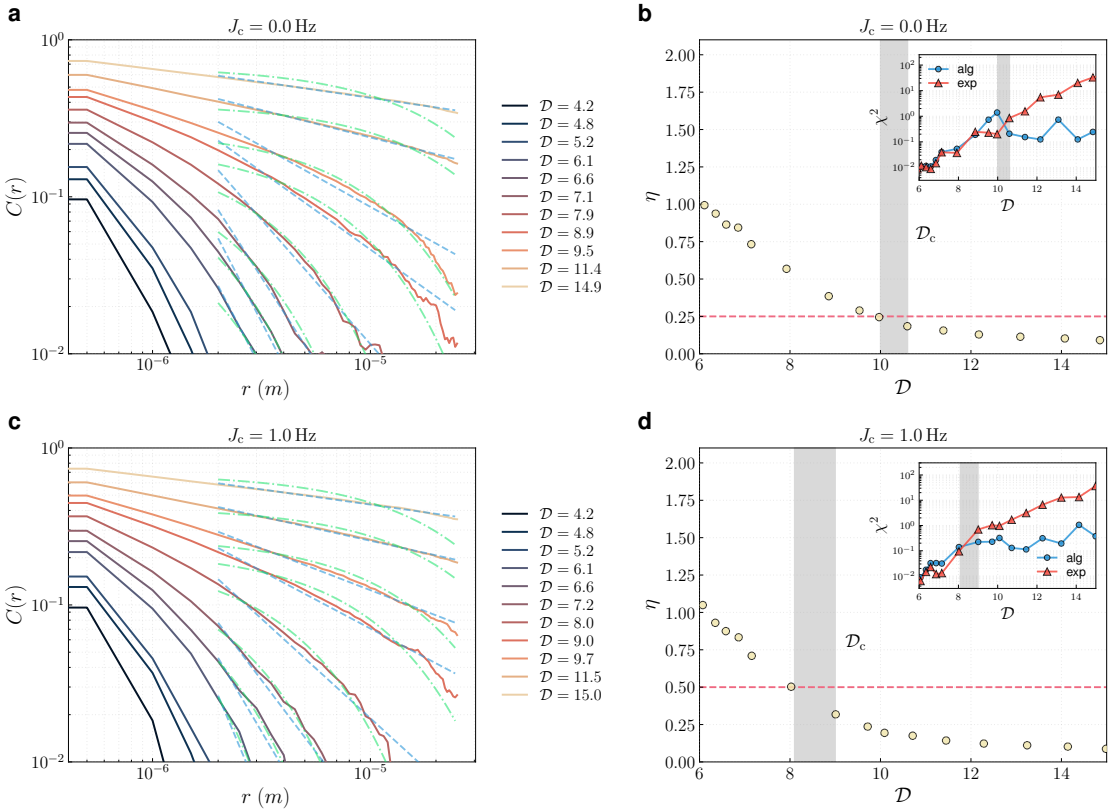

Figure 3.7: Correlation function of common phase in coupled bilayer. (**a**,**c**) Representative phase correlation functions of common phase $C(r)$ at different PSDs with two Josephson coupling strengths. Each dataset is fitted with an exponential model $y = ae^{-2r/r_0}$ (green dash-dotted line) and an algebraic model $y = ar^{-2\eta}$ (blue dashed line). (**b**,**d**) Extracted values of η as a function of PSD. The red dashed line marks $\eta = 0.25$ for decoupled fields, and $\eta = 0.5$ for coupled fields. The inset shows χ^2 statistics for exponential and algebraic fits, with the critical PSD $\mathcal{D}_c$ extracted from the crossover point. The overlap of the χ^2 test values for the algebraic and exponential models at low PSDs arises because the correlation function decays to zero very rapidly. As a result, there are too few data points for a reliable fit, and noise near zero further affects the fitting accuracy.

We evaluate the phase correlation functions of both the relative and common phases. We find that the common-phase correlations evolve from exponential decay to algebraic decay (see Figure 3.7), which is the hallmark of the BKT transition. The critical point of the transition, however, is shifted by the interlayer coupling strength. For $J_c = 1\,\text{Hz}$, the critical PSD decreases from $D_c \approx 10.4$ in the decoupled case to $D_c \approx 8.5$. The correlation function is fitted with $y = ar^{-2\eta}$ rather than the single-layer form $y = ar^{-\eta}$, since in the decoupled bilayer case the correlation functions of both the common and relative phases are squared (see Section 2.2.3).

As expected from the coupled two-dimensional XY model, the critical exponent η_c is doubled in the coupled bilayer. In Figure 3.7c and Figure 3.7d, we indicate the critical exponent predicted in the thermodynamic limit by red dashed line, though the estimated value is slightly smaller due to finite-size effects.

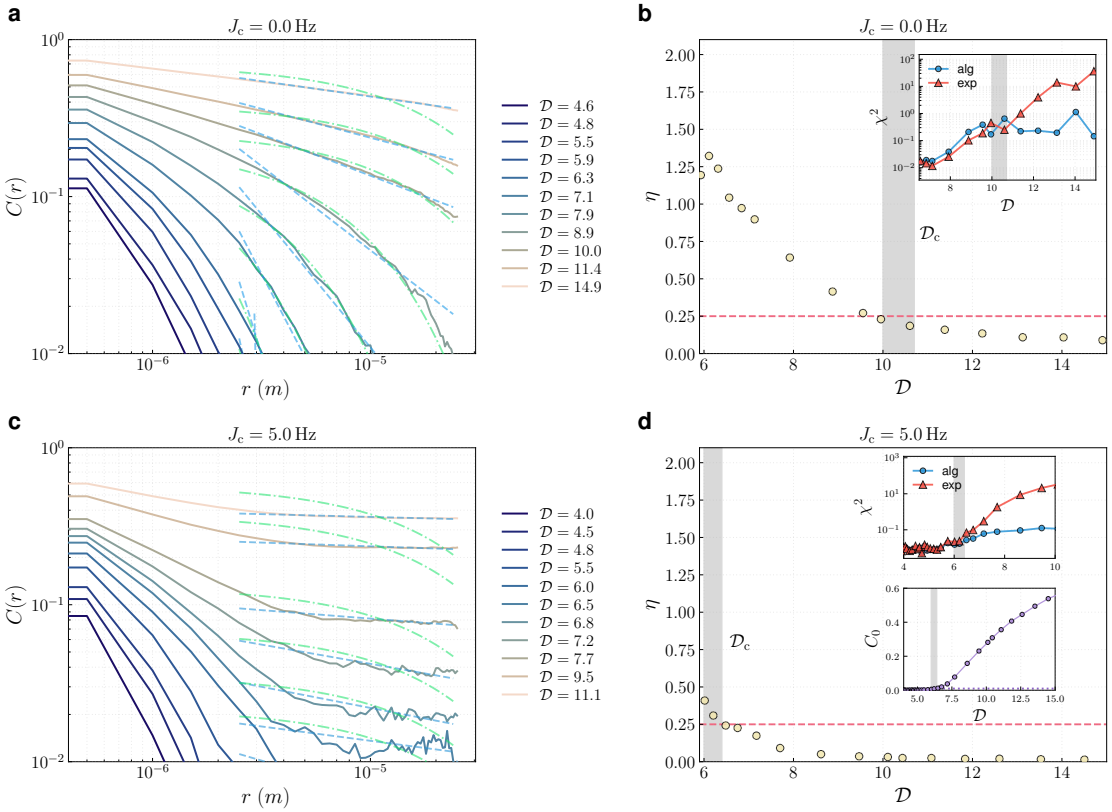

Figure 3.8: Correlation function of relative phase in coupled bilayer.(**a**,**c**) Representative phase correlation functions of relative phase $C(r)$ at different PSDs with two various Josephson coupling strengths. Each dataset is fitted with an exponential model $y = ae^{-2r/r_0}$ (green dash-dotted line) and an algebraic model $y = ar^{-2\eta}$ (blue dashed line). (**b**) Extracted values of η as a function of PSD. The red dashed line marks $\eta = 0.25$, and the inset shows χ^2 statistics for exponential and algebraic fits. (**d**) Extracted values of η as a function of PSD. One inset shows the χ^2 statistics for exponential and algebraic fits, from which the critical PSD $\mathcal{D}_c$ is extracted at the crossover point. The other inset shows the fitted values of C_0, obtained from the model $y = ae^{-2r/r_0} + C_0$.

In contrast, the relative-phase correlations in the coupled bilayer transition from exponential decay to LRO, as shown in Figure 3.8c. For consistency, we continue to apply both algebraic and exponential fits to the correlation functions for two main reasons. First, this approach remains valid even when the true behavior corresponds to LRO. In such cases, the initial power-law decay part and the long-distance tail

of the correlation function is more accurately described by an algebraic form than by an exponential one. Second, in inhomogeneous systems such as harmonically trapped gases, LRO is difficult to observe in the weak-coupling regime, and the correlation functions instead exhibit effective power-law decay. Moreover, the exponent η extracted from the algebraic fits still provides an effective measure of the degree of order in the system. We also employ an alternative method to distinguish between exponential decay and LRO. We fit the correlation function with the model $y = ae^{-2r/r_0} + C_0$, which provides an approximate description of LRO. In this framework, LRO is signaled by a nonzero C_0. The results are shown in the inset of Figure 3.8d. We find C_0 remains zero at low PSD and begins to increase beyond the critical point, marking the transition from exponential decay to LRO.

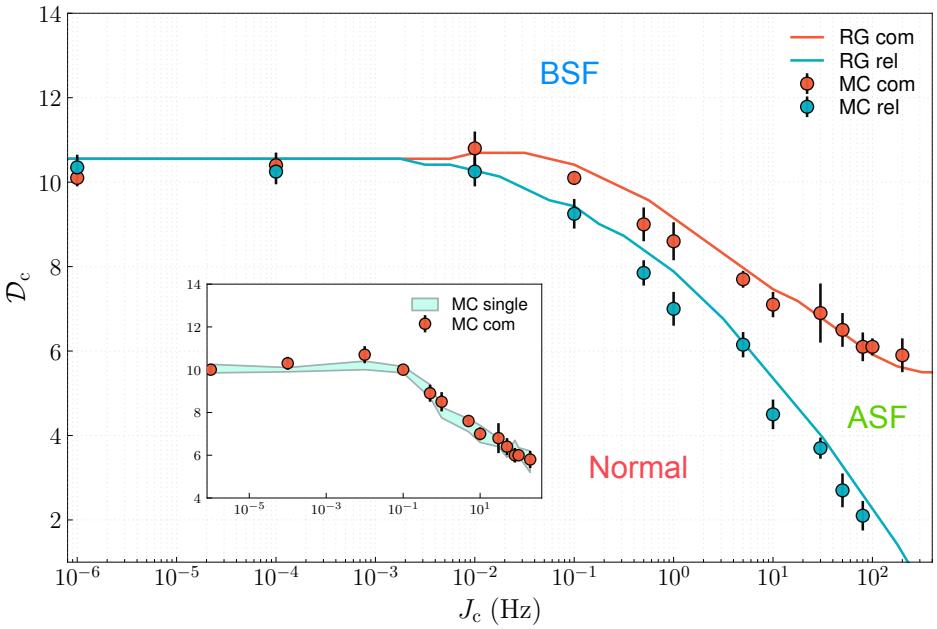

Figure 3.9: Phase diagram of coupled bilayer 2D Bose gas (MC). The critical points of the relative and common phases extracted from the χ^2 analysis are compared with the RG predictions (see Section 2.3.7). The horizontal axis is plotted on a logarithmic scale with base 10. The inset shows the critical points of the single layer (shaded area, with the width indicating the standard error) and of the common phase (markers with error bars).

In Figure 3.9, we present the extracted critical PSD D_c of the common and relative phases as a function of the interlayer coupling strength. These results are compared with the renormalization-group analysis, using initial conditions chosen

to match the experimental parameters reported in Ref. [14]. We note that the agreement is also consistent with the experimental data of Ref. [14], which will be discussed in detail in Erik Rydow's thesis [66]. The Monte Carlo results clearly reveal the ASF phase, characterized by long-range order in the relative phase while the common phase remains disordered. The common phase and the single-layer phase follow the same transition line, as shown in the inset.

As the common phase undergoes the well-known BKT transition, it is understood to be driven by the binding and unbinding of vortex–antivortex pairs, as discussed for the single-layer case. In contrast, whether the relative phase undergoes a genuine phase transition, and if so, what type of transition it represents. In the coupled two-dimensional XY model description, the relative mode can be written in the continuum limit as

$$H_{\mathrm{rel}} = \frac{J}{4} \int d^2r \ (\nabla\theta(\mathbf{r}))^2 - \Omega \int d^2r \ \cos(\theta(\mathbf{r})) \ , \tag{3.34}$$

where the variables are defined in Sec. 2.2.1. This Hamiltonian can be regarded as an XY model subject to a symmetry-breaking field represented by the term $-\Omega \int d^2r \ \cos(\theta(\mathbf{r}))$. In the famous JKKN paper, José et al. performed a perturbative RG analysis of this system and found that no stable fixed point exists [67]. This result was interpreted as implying the absence of a true phase transition in such a system and the absence of vortex unbinding, since the symmetry-breaking field is always relevant, regardless of its strength. However, subsequent rigorous RG analyses demonstrated that vortices can in fact undergo a binding–unbinding process even in the presence of such a symmetry-breaking field, giving rise to three distinct vortex phases [68–70]:

- **Linearly confined phase:** The vortex and antivortex are bound with a linear potential (strings or domain walls) identical to a kink soliton of the sine-Gordon model.
- **Logarithmically confined phase:** The vortex and antivortex are bound with a logarithmic potential.

- **Deconfined phase:** Unbound vortex and antivortex (free vortices).

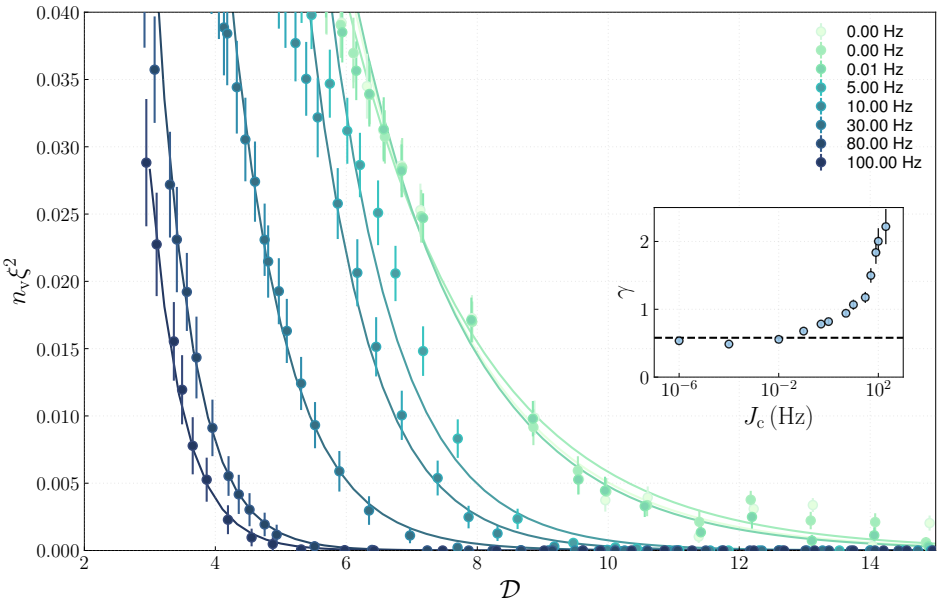

Figure 3.10: Vortices in the relative phase. Representative dimensionless vortex density $n_v\xi^2$ of the relative phase, obtained from Monte Carlo simulations as a function of the phase-space density $\mathcal{D}$ for different interlayer coupling strengths J_c. The solid lines represent exponential fits using the model $y = Ae^{-\gamma\mathcal{D}}$, with the fitted values of γ at each J_c shown in the inset. The dashed line in the inset indicates $\gamma = 0.57$, as previously reported for the single-layer BKT transition.

The system can evolve from a deconfined phase to a linearly confined phase either by lowering the PSD (or temperature) or by increasing the strength of the symmetry-breaking field. The transition between these phases are found to be a continuous but not a conventional thermodynamic phase transition, but can be identified by the qualitative change on transport properties, correlation functions and $I - V$ curve in bilayer superconductors [69, 70].

During the analysis of MC simulated fields, we apply a Gaussian filter with $\sigma = 1.5\,\mu$m, chosen to be comparable to both the healing length and the imaging resolution of the experimental setup used in this thesis and in Ref. [14]. Vortices are then counted at different PSDs and interlayer coupling strengths J_c. Results are plotted in Figure 3.10, we find that the dimensionless free-vortex density decreases exponentially with increasing PSD for all nonzero values of J_c, with the decay rate depending on the coupling strength. At the same time, the vortex density is further

suppressed as the coupling strength increases. These results suggest that vortex binding persists in the relative phase and plays an important role in driving the change of the correlation function from exponential decay to LRO.[4]

3.2.3 BKT paired phase in bilayer 2D Bose gases

As discussed in Sec. 2.2.4 and shown by the Monte Carlo results in Figure 3.9, a first-order (two-body) Josephson coupling is insufficient to generate the BKT paired phase; instead, a four-body interlayer coupling is required. To investigate this scenario, we perform MC simulations of the bilayer two-dimensional Bose gas with a four-body Josephson coupling to examine whether the BKT paired phase emerges. We adapt the discrete Hamiltonian for the tunnel-coupled bilayer, but with a modified Josephson coupling term

$$H = H_1 + H_2 + H'_{12} \,, \tag{3.35}$$

with

$$H_a = -J_\mathrm{h} \sum_{i \neq j} w_{i,\,j}\, \psi^*_{a,\,i} \psi_{a,\,j} + \frac{U}{2} \sum_i n^2_{a,\,i} + \sum_i \left(V_i - \mu\right) n_{a,\,i} \,, \tag{3.36}$$

and

$$H'_{12} = -J_\mathrm{c} \sum_{\langle ij \rangle} \frac{\left(\psi_{1,\,i}\, \psi_{2,\,i}\, \psi^*_{1,\,j}\, \psi^*_{2,\,j} + \psi^*_{1,\,i}\, \psi^*_{2,\,i}\, \psi_{1,\,j}\, \psi_{2,\,j}\right)}{\sqrt{n_{1,\,i}\, n_{2,\,i}}} \,, \tag{3.37}$$

where H'_{12} denotes a four-body interlayer coupling, and $\langle ij \rangle$ denotes nearest neighbors. The simulations are carried out in a circular potential of radius $24\,\mu$m with a discretization length of $0.5\,\mu$m. The interlayer coupling strength J_c is varied from 10^{-6} to 100 Hz. The temperature is fixed at 30 nK and the dimensionless interaction strength at $\tilde{g} = 0.084$.

In Figure 3.11, we show the correlation functions at different PSDs for $J_\mathrm{c} \approx 70\,\mathrm{Hz}$, comparing the single-layer and common phases. We find that the critical PSD $\mathcal{D}_\mathrm{c}$ of the common phase is smaller than that of the single layer, which is indicative

[4] It is worth noting that the transition has also been proposed to be first order in Ref. [13] However, within the RG framework employed there, it is difficult to unambiguously distinguish a strong crossover from a genuine first-order transition.

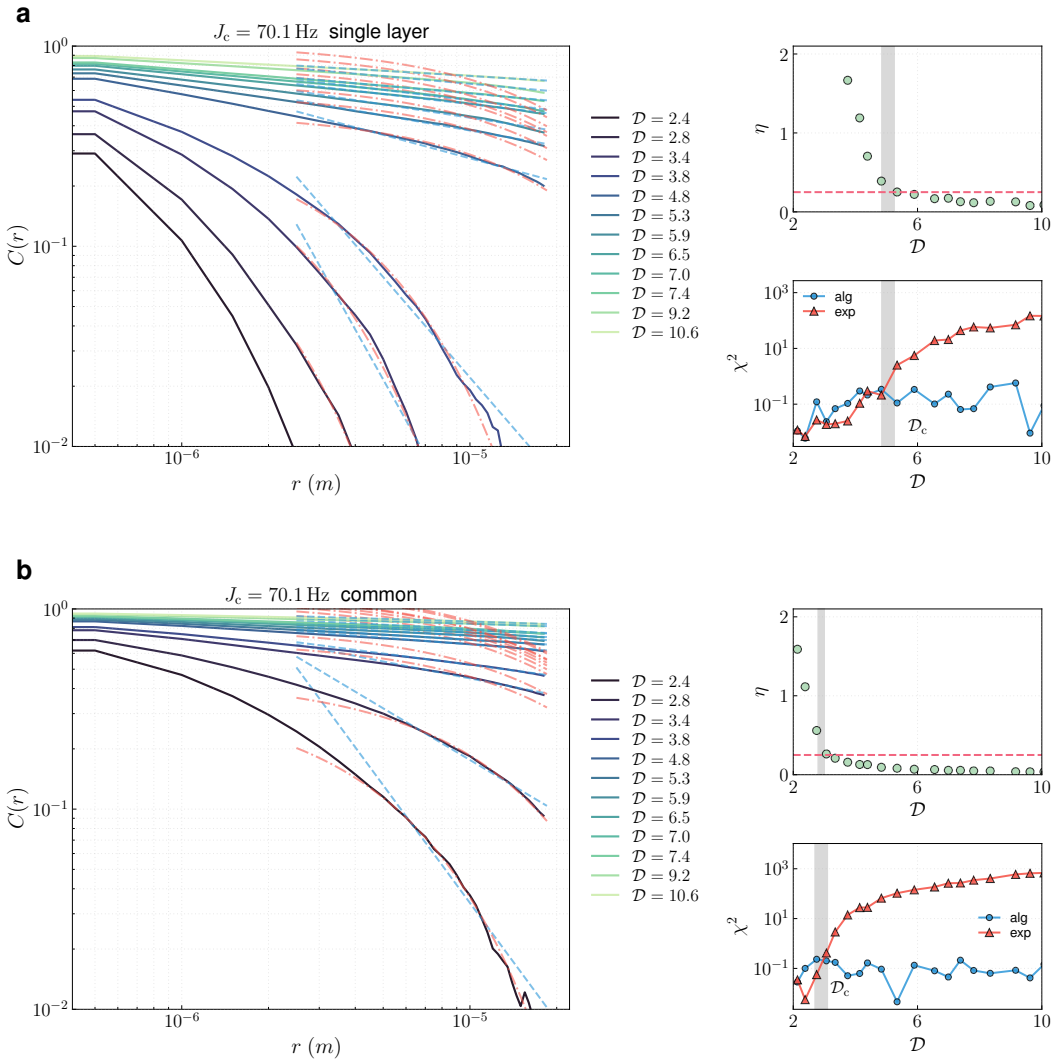

Figure 3.11: Phase correlation function in BKT paired phase. (**a**,**b**) Representative phase correlation functions $C(r)$ of the single-layer and common phases at different PSDs with $J_c \approx 70.1$ Hz. Each correlation function is fitted with an exponential model $y = ae^{-r/r_0}$ (red dash-dotted line) and an algebraic model $y = ar^{-\eta}$ (blue dashed line). The extracted values of η are shown as a function of PSD, with the red dashed line indicating $\eta = 0.25$. The critical PSD $\mathcal{D}_c$ is determined from the crossover point of the χ^2 analysis.

of the emergence of a *BKT paired phase*. For both the single-layer and common-phase correlation functions, the transition retains the characteristic change from exponential to algebraic decay, the hallmark of the BKT transition. Notably, fitting both correlation functions with the algebraic form $y = ar^{-\eta}$ yields critical exponents close to $\eta_c = 0.25$, in contrast to the value $\eta_c = 0.5$ expected for the common phase in the decoupled case. This implies a breakdown of $g_{\text{com}}(r) \propto g^2(r)$. It is interesting

to note that the critical superfluid exponent of the common phase coincides with the conventional BKT critical value. A tentative explanation is that, in the strong four-body coupling limit, the low-energy effective Hamiltonian is dominated by

$$H \approx -2nJ_{\mathrm{c}} \sum_{\langle ij \rangle} \cos(\phi_{a,i} + \phi_{b,i} - \phi_{a,j} - \phi_{b,j}) = -2nJ_{\mathrm{c}} \sum_{\langle ij \rangle} \cos(\varphi_{\mathrm{com},i} - \varphi_{\mathrm{com},j}) \ , \tag{3.38}$$

which is identical in form to Eq. (2.35), as expected. This corresponds directly to the two-dimensional XY model, expressed in terms of the common-phase variable $\varphi_{\mathrm{com}} = \phi_1 + \phi_2$. At the same time, the common phase can be regarded as an independent variable with its own symmetry, and thus undergoes a BKT transition with the universal critical exponent $\eta_{\mathrm{c}} = 0.25$.

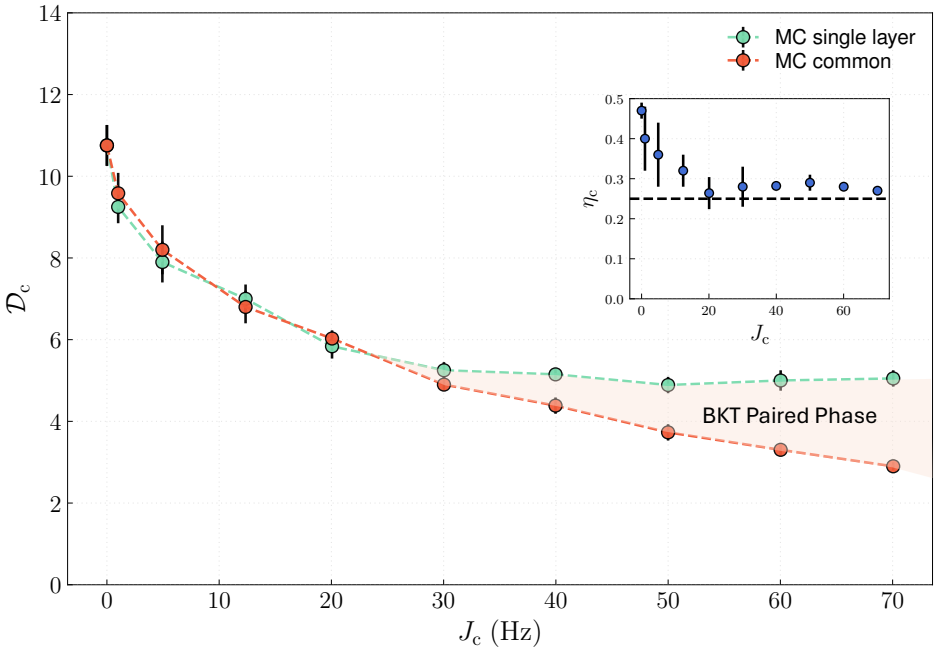

Figure 3.12: Phase diagram of BKT paired phase. The critical points of the single-layer and common phases extracted from the χ^2 analysis. $\mathcal{D}$ greater than the critical point corresponds to the ordered phase, while smaller $\mathcal{D}$ corresponds to the disordered phase. The shaded region denotes the BKT paired phase. The inset shows the estimated critical superfluid exponent η_{c} of the common phase at various coupling strengths.

We extract the critical points of the single-layer and common phases, as shown in Figure 3.12. A BKT paired phase emerges for $J_{\mathrm{c}} \gtrsim 30\,\mathrm{Hz}$, indicated by the clear separation of the two transition lines. The critical exponent η_{c} exhibits a

dependence on the coupling strength, decreasing from 0.5 (expected in the decoupled case when fitting with the model $y = ar^{-\eta}$) to 0.25 as the coupling increases. This behavior is consistent with Monte Carlo results for the coupled XY model with four-body interactions [32]. The critical points of the single layer also decrease with increasing coupling, but eventually saturate at a plateau of approximately half the $\mathcal{D}_c$ of the decoupled case, similar to the behavior of a tunnel-coupled bilayer, as expected (see Section 2.2.4).

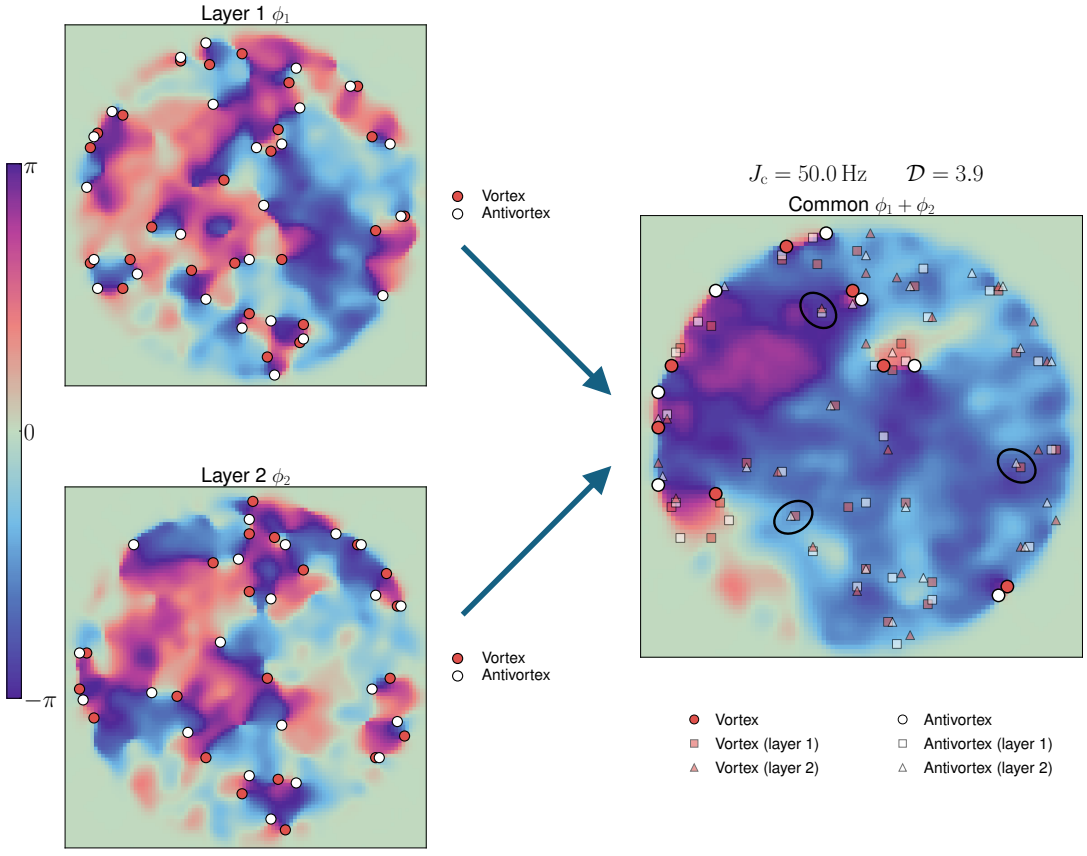

Figure 3.13: Phase profile and paired vortices. Phase profiles of the single-layer and common phases with detected vortices (red filled circles) and antivortices (white filled circles). Vortices identified in the single layers are overlaid as transparent markers on the common-phase profile. Black circles highlight examples of vortex–antivortex pairs formed across different layers. The phase outside the cloud is manually set to 0.

To investigate the physics of the BKT paired phase, we analyze the phase profiles within this regime. A Gaussian filter with width $\sigma = 1\,\mu$m is applied to remove tightly bound vortex–antivortex pairs. An example is shown in Figure 3.13. In the single-layer phase, the profiles exhibit the expected disordered behavior with

many free vortices. By contrast, the common phase exhibits superfluid, with only very few free vortices detected. For comparison with the single layer, we project the vortices detected in both layers onto the common phase. We find that vortices and antivortices in different layers bind together, so that although each individual layer remains disordered, the four-body coupling generates vortex–antivortex pairs in the common-phase field, leaving it ordered. This is in contrast to the two-body coupling, which locks vortices of the same sign across layers, whereas the four-body mechanism gives rise to the BKT paired phase.

3.3 Dynamical Simulations of a Bilayer 2D Bose Gases

Building on the classical-field Monte Carlo simulations, we extend the study to investigate the dynamics of the bilayer system. The time evolution of the bosonic fields is governed by the tunnel-coupled Gross–Pitaevskii equations (GPEs),

$$i\hbar\frac{\partial\psi_1}{\partial t} = \left(-\frac{\hbar^2}{2m}\nabla^2 + V(r) + g|\psi_1|^2\right)\psi_1 - J_c\psi_2 \,, \tag{3.39}$$

$$i\hbar\frac{\partial\psi_2}{\partial t} = \left(-\frac{\hbar^2}{2m}\nabla^2 + V(r) + g|\psi_2|^2\right)\psi_2 - J_c\psi_1 \,, \tag{3.40}$$

where $\psi_{i=1,2}$ denotes the fields in layers 1 and 2, J_c is the interlayer coupling strength. To simulate the time evolution, the fields are propagated according to the above equations of motion, with initial states provided by MC simulations. The equations of motion are solved numerically using a fifth-order *Runge–Kutta method* (RKM), rather than the split-step method commonly employed for solving the GPEs, in order to avoid spectral aliasing during the time evolution. In particular, we employ the Cash–Karp scheme, implemented with a fixed timestep rather than its usual adaptive form [71]. We again apply a 25-point Laplacian during the integration to suppress anisotropic effects in the dynamics.

This dynamical simulation method is applied to study universal coupling-quench dynamics, which will be discussed in Chapter 5 and compared with experimental

data. As a first step, we investigate Josephson oscillations in a tunnel-coupled two-dimensional bilayer at finite temperature, a phenomenon that has been extensively studied and is essential for understanding out-of-equilibrium dynamics in coupled bilayer systems [4–8, 72]. However, experimental observations and numerical studies in two-dimensional bilayer bosonic systems are still lacking. The simulations presented here therefore provide a valuable starting point prior to performing experiments, which are planned for our new experimental apparatus [63].

3.3.1 Josephson effects in tunnel-coupled 2D bilayer Bose gases

The foundational concepts were first developed in the context of superconductivity by Brian Josephson in 1962 [73]. He predicted that a supercurrent of Cooper pairs could tunnel through a thin insulating barrier separating two superconductors, driven not by an applied voltage but by the difference in the macroscopic quantum phases of the two superconducting wavefunctions. This phenomenon is now known as the Josephson effect.

The underlying principles are not limited to superconductors and have also been observed in other superfluids, such as helium-3 [74], as well as in Bose–Einstein condensates. With the advent of ultracold atomic gases, the bosonic Josephson junction (BJJ) emerged as a highly controllable and versatile analogue [4–8, 75]. A BJJ is typically realized by two weakly coupled Bose–Einstein condensates (BECs), often confined in a double-well potential.

3.3.1.1 The two-mode model

To describe the dynamics of a BJJ trapped in a double well potential, a common and effective approach is the two-mode model (TMM) [76, 77]. This model simplifies the complexity of the many-body system by assuming that at sufficiently low energies, the atoms only occupy the two lowest energy modes of the double-well potential, and the barrier height is sufficiently higher than the chemical potential of each well.

These modes correspond to two eigenstates, the symmetric ground state, $\psi_{\rm s}(\mathbf{r})$, and the anti-symmetric first excited state, $\psi_{\rm a}(\mathbf{r})$. Then we define the field operator

$$\hat{\Psi} = \psi_{\rm s}(\mathbf{r})\hat{a}_{\rm s} + \psi_{\rm a}(\mathbf{r})\hat{a}_{\rm a} \ , \tag{3.41}$$

where, $\hat{a}^\dagger_{\rm s,a}$ are creation operators associated with symmetric and antisymmetric mode. A more intuitive basis can be constructed from linear combinations of symmetric and anti-symmetric operators, corresponding to the atoms localized in the left (L) and right (R) wells

$$\hat{a}^\dagger_{\rm L} = \frac{\hat{a}^\dagger_{\rm s} + \hat{a}^\dagger_{\rm a}}{\sqrt{2}} \ , \quad \hat{a}^\dagger_{\rm R} = \frac{\hat{a}^\dagger_{\rm s} - \hat{a}^\dagger_{\rm a}}{\sqrt{2}} \ , \tag{3.42}$$

where $\hat{a}^\dagger_{\rm L,R}$ and $\hat{a}_{\rm L,R}$ are the creation and annihilation operators for an atom in the left or right well. This basis leads to the two-site Bose-Hubbard two-mode Hamiltonian [62, 78, 79]:

$$\hat{H}_{\rm TMM} = -J_{\rm c}(\hat{a}^\dagger_{\rm L}\hat{a}_{\rm R} + \hat{a}^\dagger_{\rm R}\hat{a}_{\rm L}) + \frac{U}{2}\left[\hat{n}_{\rm L}(\hat{n}_{\rm L}-1) + \hat{n}_{\rm R}(\hat{n}_{\rm R}-1)\right] + \Delta(\hat{n}_{\rm R} - \hat{n}_{\rm L}) \ , \tag{3.43}$$

where $\hat{n}_{\rm L,R} = \hat{a}^\dagger_{\rm L,R}\hat{a}_{\rm L,R}$ are the respective number operators. The model is characterised by three key energy scales:

- **Tunnelling Energy ($J_{\rm c}$):** This parameter quantifies the rate of single-particle tunneling through the barrier between the two wells, determined by the overlap of the left and right wavefunctions.

- **On-site Interaction Energy (U):** This describes the mean-field interaction energy between atoms within the same well.

- **Potential Asymmetry (Δ):** This accounts for any energy difference between the potential minima of the two wells.

In the limit of a large number of atoms, a mean-field treatment can be applied by replacing the operators with complex numbers: $\hat{a}_{\rm L,R} \to \sqrt{N_{\rm L,R}}e^{i\phi_{\rm L,R}}$. The dynamics

of the system can then be described by two canonically conjugate variables: the fractional population imbalance, $z(t)$, and the relative phase, $\theta(t)$.

$$z(t) = \frac{N_{\mathrm{L}}(t) - N_{\mathrm{R}}(t)}{N_{\mathrm{T}}} \,, \tag{3.44}$$

$$\theta(t) = \phi_{\mathrm{L}}(t) - \phi_{\mathrm{R}}(t) \,, \tag{3.45}$$

where $N_{\mathrm{T}} = N_{\mathrm{L}} + N_{\mathrm{R}}$ is the total, conserved number of atoms. The classical equations of motion derived from the Hamiltonian in Eq. (3.43), using $\dot{z} = -\frac{\partial H}{\partial \phi}$ and $\dot{\phi} = \frac{\partial H}{\partial z}$, are given by [76, 79]:

$$\frac{dz}{dt} = -\frac{2J_{\mathrm{c}}}{\hbar}\sqrt{1-z^2}\sin(\theta) \,, \tag{3.46}$$

$$\frac{d\theta}{dt} = \frac{\Delta}{\hbar} + \frac{UN_{\mathrm{T}}}{\hbar}z + \frac{2J_{\mathrm{c}}}{\hbar}\frac{z}{\sqrt{1-z^2}}\cos(\theta) \,. \tag{3.47}$$

These equations describe a rich variety of dynamical behaviours and are analogous to the motion of a non-rigid pendulum, where z corresponds to the angular momentum and θ to the tilt angle.

The behaviour of the system is largely determined by the ratio of the interaction energy to the tunnelling energy, $\Lambda = UN_{\mathrm{T}}/(2J_{\mathrm{c}})$, and the initial conditions (z_0, θ_0). If we consider the interacting gas, two primary dynamical regimes exist.

Josephson (plasma) oscillations

For small initial population imbalances and $\Lambda \sim 1 > 1/N_{\mathrm{T}}$ [79, 80], the system exhibits approximately sinusoidal oscillations of both population and phase around the equilibrium point $(z = 0, \theta = 0)$, as shown in Figure 3.14a. This corresponds to the pendulum swinging back and forth. In the limit of small amplitudes, the frequency of these oscillations, known as the *Josephson plasma frequency*, is given by

$$\omega_{\mathrm{p}} = \frac{2J_{\mathrm{c}}}{\hbar}\sqrt{1+\Lambda} = \frac{1}{\hbar}\sqrt{2J_{\mathrm{c}}\Big(UN_{\mathrm{T}} + 2J_{\mathrm{c}}\Big)} \,, \tag{3.48}$$

which reduces to the noninteracting Rabi frequency $\Omega_{\mathrm{R}} = 2J_{\mathrm{c}}/\hbar$ when $U \to 0$.[5] In phase space, low–energy trajectories are closed orbits encircling $(0, 0)$.

[5] when interactions are negligible ($\Lambda \ll 1$), the dynamics are purely sinusoidal at Ω_{R} and coincide with single–particle Rabi oscillations, which we do not analyze further here as our focus is the interacting Josephson regime.

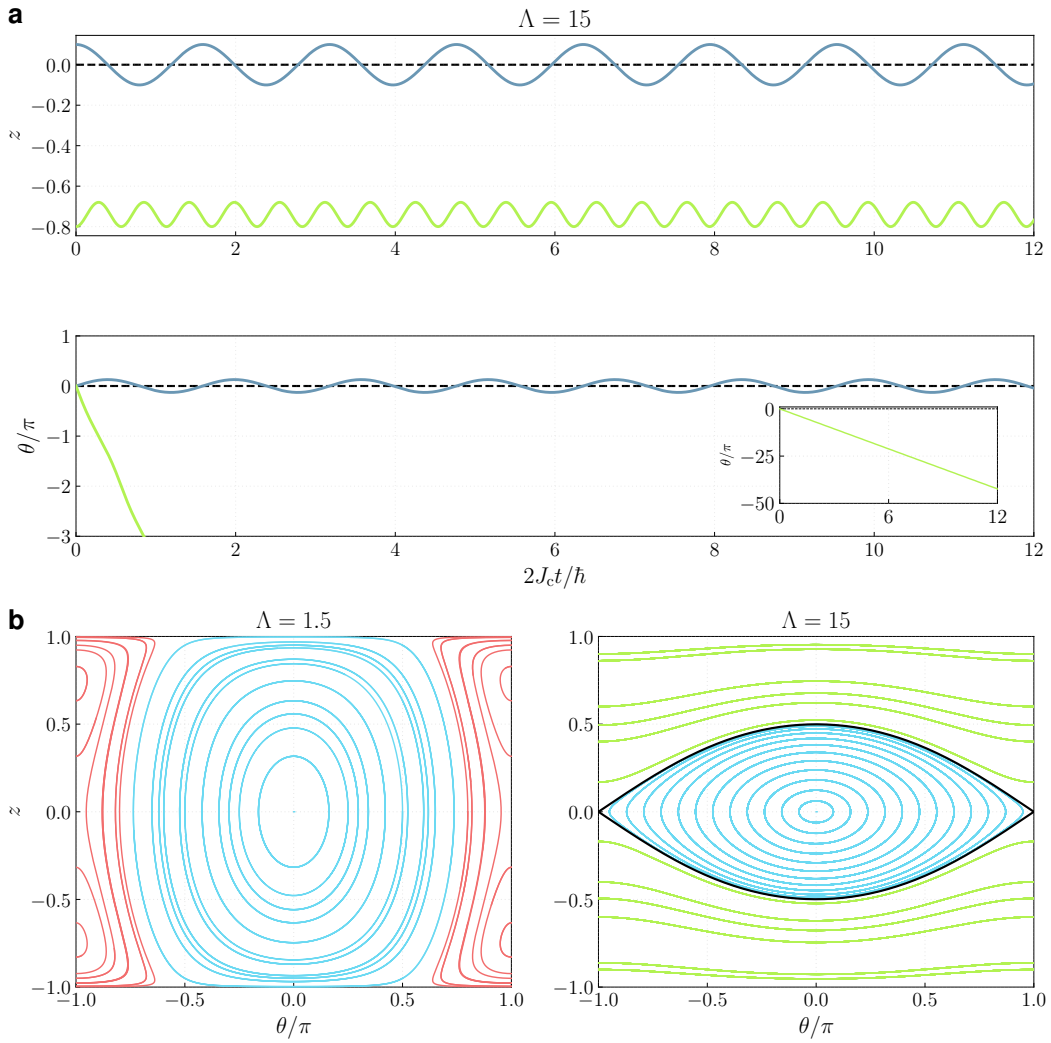

Figure 3.14: Josephson dynamics in the two–mode model. (**a**) Time evolution of the population imbalance z and relative phase θ for $\Lambda = 15$. Blue: initial condition $z_0 = 0.1$, $\theta_0 = 0$ (Josephson/plasma oscillations). Green: initial condition $z_0 = -0.8$, $\theta_0 = 0$ (macroscopic self–trapping; inset: the phase $\theta(t)$ winds monotonically). Time is measured in units $\hbar/2J_c$. Red curves illustrate oscillations about fixed points with nonzero phase. (**b**) Phase–space portraits in (θ, z) for different Λ. Blue curves indicate closed Josephson orbits; green curves indicate self-trapped trajectories. The black curve is the separatrix for $\Lambda = 15$, which separates the Josephson and self-trapping regimes.

Macroscopic quantum self–trapping (MQST)

For sufficiently strong interactions relative to tunneling ($\Lambda \gg 1$), the nonlinear dynamics admit a separatrix that passes through the saddle points $(z, \theta) = (0, \pm\pi)$. Initial conditions that place the system above this separatrix give rise to *macroscopic quantum self–trapping* (MQST): $z(t)$ oscillates about a nonzero mean while the

phase $\theta(t)$ winds continuously (see Figure 3.14a). The origin of MQST can be seen from the classical two–mode Hamiltonian [76, 79, 80]

$$H(z,\theta) = \frac{\Lambda}{2}\, z^2 - \sqrt{1-z^2}\,\cos\theta\,, \tag{3.49}$$

where we have written the Hamiltonian in the standard dimensionless form, yielding equations of motion with a rescaled time $\tau = (2J_c/\hbar)t$. We also set the static bias to zero, $\Delta = 0$. We know the dynamics acquire a separatrix passing through $(z,\theta) = (0,\pi)$ for $\Lambda \gg 1$. Energy conservation together with the bounded tunneling term $-\sqrt{1-z^2}\cos\theta \in [-1,1]$ implies that at balanced population $z = 0$ the energy satisfies $H(0,\theta) \in [-1,1]$. Therefore, if the initial energy E_0 exceeds the separatrix value $E_{\rm sep} = H(0,\pi) = 1$, the point $z = 0$ does not lie on the constant–energy trajectory and is kinematically inaccessible.

For an initial phase $\theta_0 = \theta\,(0) = 0$, the onset of MQST is obtained by equating the initial energy to the separatrix energy,

$$\frac{\Lambda}{2}\, z_0^2 - \sqrt{1-z_0^2} = 1\,,$$

which yields the threshold imbalance

$$z_c(\Lambda) = \frac{2\sqrt{\Lambda-1}}{\Lambda}\,, \qquad (\Lambda > 1)\,, \tag{3.50}$$

so that trajectories cannot cross $z = 0$ for any subsequent time when $z_0 > z_c$, as shown in Figure 3.14b.

3.3.1.2 Numerical simulation of Josephson effects

We simulate the Josephson effect by preparing initial fields in a decoupled 2D bilayer using Monte Carlo sampling at $T = 30\,\mathrm{nK}$, confined in a square box potential of size $49\,\mu\mathrm{m}$. The simulations are performed with a discretization length of $0.25\,\mu\mathrm{m}$. For each realization, the mean phase of each layer is computed, and a controlled global phase difference is introduced by adding a phase offset. This procedure ensures that each cloud retains its intrinsic phase fluctuations. To introduce a density imbalance, layers 1 and 2 are prepared with different PSDs, corresponding to different atom

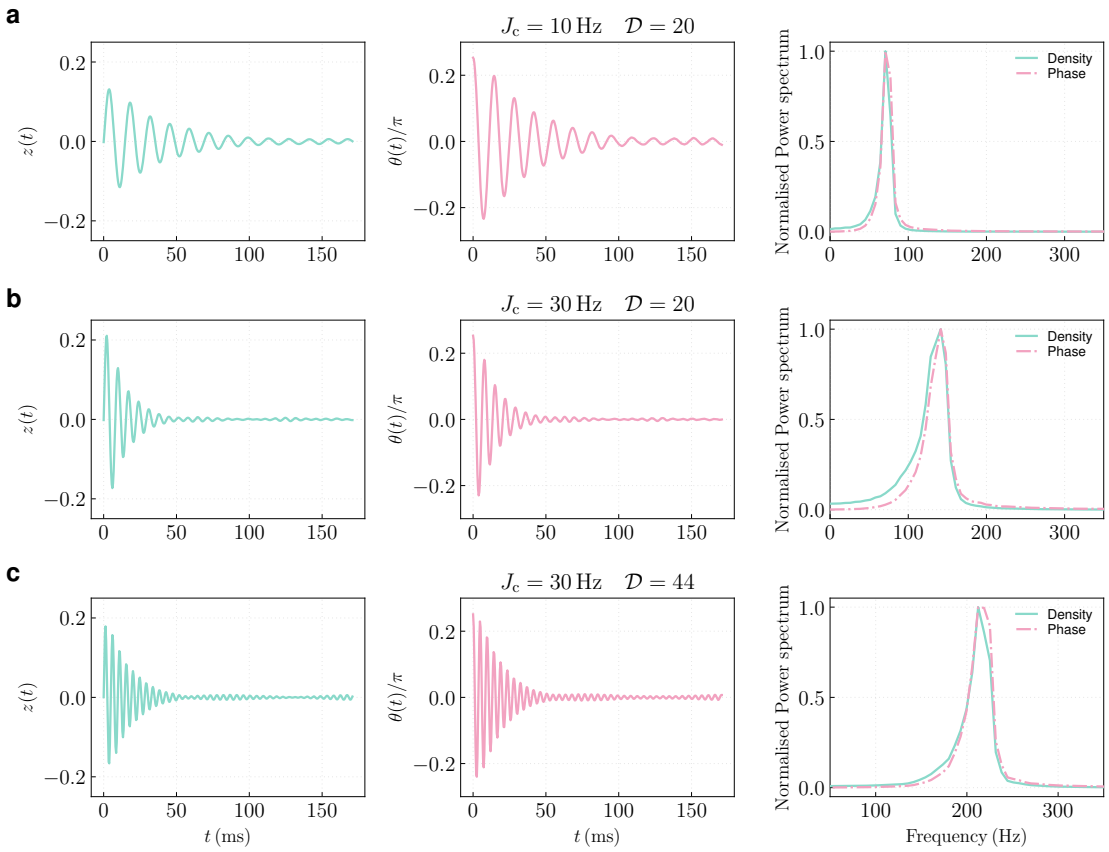

Figure 3.15: Numerical simulation of Josephson oscillations. Time evolution of the fractional population imbalance and relative phase for $\mathcal{D} = 20$ with (**a**) $J_c = 10\,\mathrm{Hz}$ and (**b**) $J_c = 50\,\mathrm{Hz}$, averaged over 10 realizations at each time step. The corresponding power spectra are shown for both density and phase, normalized to their respective maxima. (**c**) Same analysis for $\mathcal{D} = 44$.

numbers in each cloud, thereby mimicking realistic experimental conditions. The bilayer fields ψ_1 and ψ_2 are subsequently time evolved from $t = 0$ according to Eq. (3.40), with a controlled interlayer coupling J_c [6], corresponding to a sudden switch-on of the coupling. The integration timestep is chosen sufficiently small ($\Delta t \sim 0.2\,\mu\mathrm{s}$) to ensure numerical accuracy and preserve unitary evolution.

We first simulate the dynamics with $z_0 \approx 0$ and $\theta_0 \approx 0.25\pi$, using $\mathcal{D} = 20$ for both clouds, which lies well above the BKT transition point ($\mathcal{D}_c \approx 11$) and is experimentally accessible. Figures 3.15a and 3.15b show the evolution of the fractional population imbalance z and the relative phase θ for two different interlayer couplings. Both z and θ oscillate around zero with matching frequencies, as expected.

[6] Here J_c is defined such that hJ_c corresponds to the single-particle Josephson tunnelling energy

We then simulate the dynamics at even higher PSD ($\mathcal{D} = 44$) while keeping the coupling strength fixed, corresponding to an increased atom number at constant temperature. As anticipated, the oscillation frequency is higher than in the lower-PSD case. In Figure 3.16a, we plot the dominant oscillation frequency as a function of coupling strength and compare it with the prediction of the two-mode model prediction (solid line), finding good overall agreement. For $\mathcal{D} = 20$, however, the frequency is slightly lower than the theoretical value, possibly due to finite-temperature effects. In all simulations, the oscillations decay over time rather than maintaining a constant amplitude, in contrast to the two-mode prediction. Notably, although the oscillations damp rapidly at early times, they persist with small amplitude throughout the simulation window rather than locking completely to zero. In the high-PSD simulations, we observe a clear revival of the oscillation amplitude following the initial decay, which can be attributed to partial rephasing [81, 82]. A similar decay of oscillation amplitude beyond the two-mode description has also been observed experimentally in various systems [4, 7, 8, 72, 83]. We find that the damping rate depends on the coupling strength, as shown in Figure 3.16b.[7] In addition, the high PSD case exhibits a slightly longer damping time, corresponding to a lower damping rate compared with the low PSD case.

Damping in bosonic Josephson junctions can arise from both extrinsic and intrinsic channels. Coupling the system to an Ohmic bosonic bath provides a dissipative environment [84], while in two-dimensional junctions the supercurrent can additionally lose energy through phonon radiation and vortex–antivortex pair dynamics [85]. In our simulations of bilayers, we observe the presence of topological defects, which can contribute to the damping and will be discussed in more detail later. In elongated quasi-one-dimensional tunnel-coupled condensates, a spatially uniform phase imprint excites a ladder of even $k > 0$ Bogoliubov modes. The multimode dephasing of these modes, together with the nonlinear coupling to the symmetric (common density) mode, rapidly attenuates the global Josephson

[7] In a harmonically trapped 1D bilayer coupled Bose gas [7], the damping rate was observed to be nearly independent of the effective coupling. By contrast, simulations of such systems indicate that the damping rate depends on the single-particle tunneling coupling J_c [82].

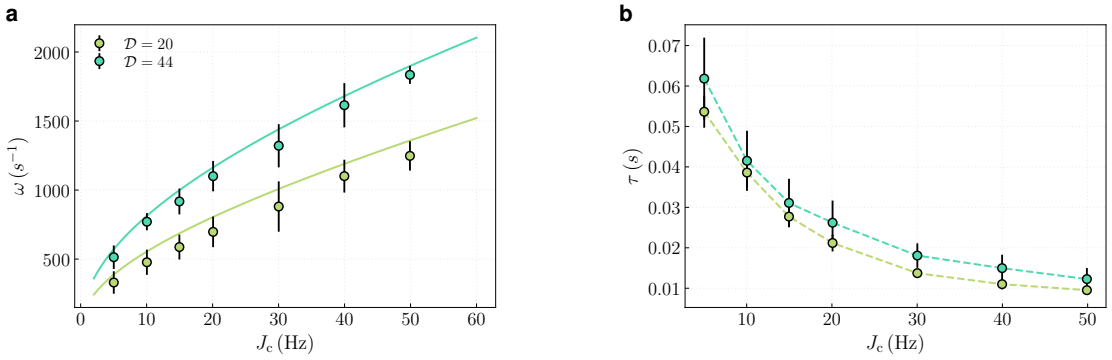

Figure 3.16: Frequency and damping time of oscillations. (**a**) Angular frequency as a function of interlayer coupling strength for two different PSDs. The solid line shows the two-mode model prediction, $\omega = \sqrt{2hJ_c\,(gn_T + 2hJ_c)}/\hbar$. (**b**) Damping time $\tau = 1/\gamma$ for various J_c, where γ is the damping rate. The damping time is obtained by fitting the peak envelope with $A = A_0 e^{-\gamma t}$.

oscillation [82]. It has further been proposed that in a uniform box trap the coupling to the common mode is suppressed, preventing the system from fully phase locking [82]. This is consistent with our observations in Figure 3.15.

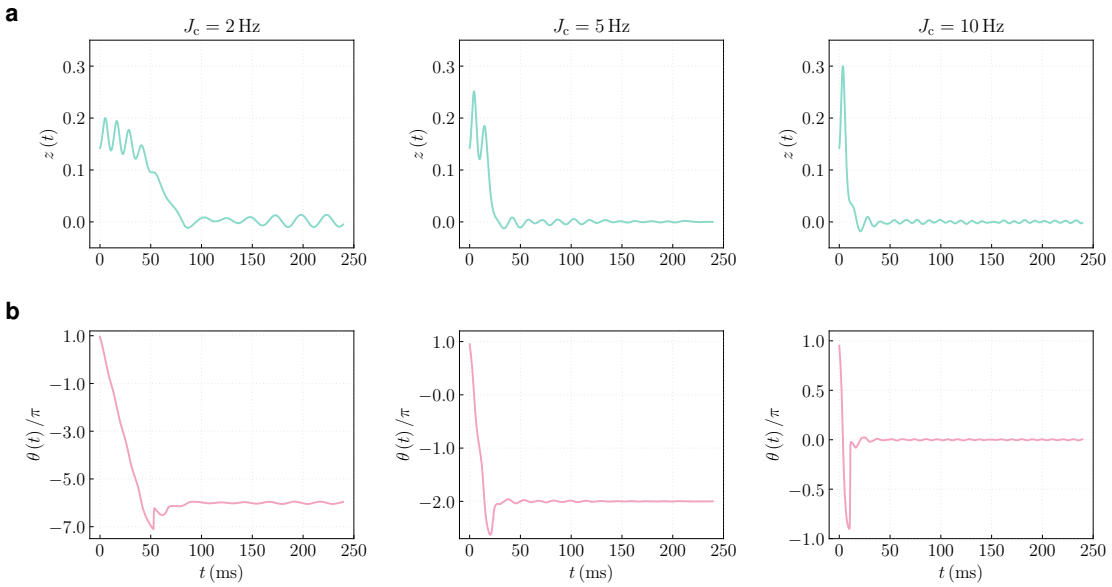

Figure 3.17: Macroscopic self-trapping. (**a**) Time evolution of the fractional population imbalance for different J_c. (**b**) Corresponding evolution of the unwrapped relative phase, averaged over 10 realizations at each time step.

We next consider the case of an initial population imbalance combined with a large phase difference. Beyond a critical condition, the system is expected to exhibit macroscopic quantum self-trapping (MQST), as shown in Eq. (3.50) and Figure 3.14.

We choose initial conditions $z_0 \approx 0.14$ ($\mathcal{D}_1 = 33$, $\mathcal{D}_2 = 25$) and $\theta_0 \approx 0.95\pi$. In our simulations, and as is normally the case in ultracold-atom experiments, the condition $\Lambda \gg 1$ holds, so the critical imbalance z_c decreases as J_c is reduced for a fixed atom number. We therefore vary the interlayer coupling strength and expect self-trapping to emerge at sufficiently low J_c. This is indeed the case, as seen in Figure 3.17. For low coupling strengths, the population imbalance initially remains trapped at a nonzero value, accompanied by a monotonically winding phase, which signals the self-trapping. However, in contrast to the sustained self-trapping predicted by the two-mode model, we find that the imbalance damps and eventually relaxes into oscillations around zero. At the same time, the relative phase ceases to wind and instead oscillates around $\theta = n2\pi$ with $n \in \mathbb{Z}$. Such relaxation is expected in the presence of dissipation [84], which may also be relevant to our simulations. Although the total energy is conserved, the symmetric (common) mode can act as a weak bath for the antisymmetric (relative) mode. Moreover, the topological excitations can again mediate energy transfer, as will be discussed later. As a result, the argument for sustained self-trapping in the two-mode model no longer applies, and $z = 0$ becomes kinematically accessible.

3.3.1.3 Domain walls and topological excitations under Josephson oscillations

Although the initial state is prepared deep in the superfluid regime, the non-adiabatic switch-on of the interlayer coupling renders this state excited with respect to the post-quench Hamiltonian and can lead to the generation of topological defects such as vortices. In the antisymmetric sector, an additional type of excitation is permitted, namely domain walls. These are line-like kinks of the relative phase (with dimensions larger than 1) that interpolate between adjacent minima of the Josephson cosine potential $J_c \cos(\theta)$, producing a 2π jump across the wall. As we will see in Chapter 5, the antisymmetric phase field is deeply connected to 2D sine-Gordon (SG) model. In this description, domain walls are the classical *soliton solutions* with a characteristic width $\xi_{\text{wall}} \propto \sqrt{1/J_c}$ [24, 86] (here we consider two clouds with equal atom number).

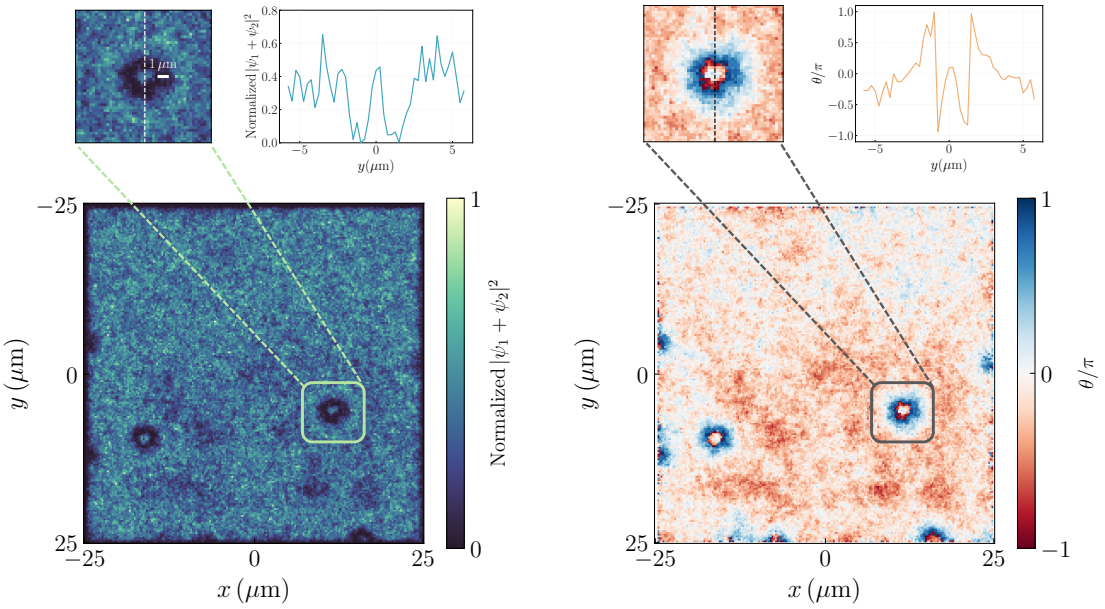

Figure 3.18: Domain walls in Josephson dynamics. (Left) Profile of $|\psi_1 + \psi_2|^2$, normalized such that the maximum value is unity. A zoomed-in view is shown at the top, and the corresponding sliced density profile along the dashed line is displayed alongside. (Right) Wrapped relative-phase profile, with a zoomed-in view shown at the top and the sliced phase profile along the dashed line displayed alongside. Two sharp phase jumps of approximately 2π, connecting regions with $\theta \approx 0$, are observed, indicating the presence of domain walls.

In Figure 3.18, we show a snapshot of $|\psi_1 + \psi_2|^2$ and of the relative phase θ at $t \approx 10\,\text{ms}$ for $z_0 = 0$, $\theta_0 = 0.25\pi$, $J_c = 40\,\text{Hz}$, and $\mathcal{D} = 44$. We find that domain walls emerge as closed loops in the relative phase, accompanied by "density" dips of characteristic size $\sim 1\,\mu\text{m}$ in $|\psi_1 + \psi_2|^2$, arising from the contribution of $\text{Re}[\psi_1\psi_2^*]$ (reflects the value of $\cos(\theta)$). We then vary the coupling strength while keeping the initial conditions fixed, and observe that reducing the coupling strength results in a thicker domain wall, as shown in Figure 3.19, consistent with expectations. We note that a similar, but much weaker, true density depletion is observed in one of the layers, accompanied by a corresponding phase winding that does not connect the minima of $\cos(\theta)$ (see Figure 3.20). This feature becomes difficult to identify as the domain wall width or thermal fluctuations increase.

We now track the formation and evolution of one of the domain walls during the Josephson oscillation, and the results are presented in Figure 3.21. At the beginning of the dynamics, no domain walls are observed in the entire field, and

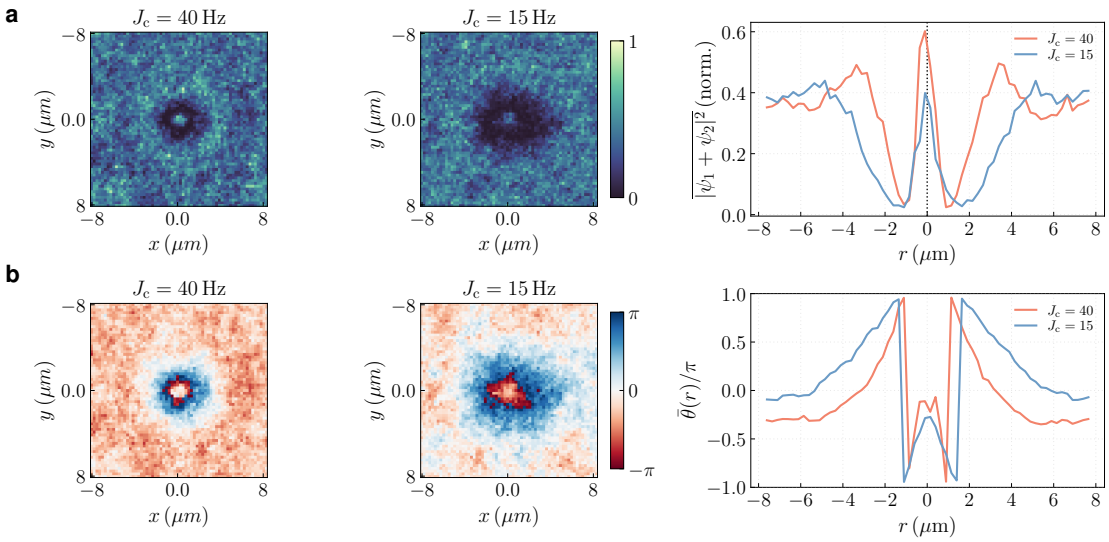

Figure 3.19: Size of domain wall. (**a**) Domain wall in the normalized $|\psi_1 + \psi_2|^2$ for two different interlayer coupling strengths, $J_c = 15\,\mathrm{Hz}$ and $J_c = 40\,\mathrm{Hz}$. The rightmost panel shows angular average computed over diameters rotated by 180°, for $J_c = 15\,\mathrm{Hz}$ (red line) and $J_c = 40\,\mathrm{Hz}$ (blue line). (**b**) Corresponding plots for the relative phase.

consequently the zoomed-in region in Figure 3.21 also shows no indication of domain wall formation. As time progresses, the first signs of a domain wall appear at the edge of the cloud around $t \approx 6\,\mathrm{ms}$ (not shown). The domain wall subsequently develops within the selected region at approximately $t \approx 7\,\mathrm{ms}$, and we find that this formation process is closely connected to the Josephson oscillation of the global relative phase. A clear domain wall at its maximum size appears when the global relative phase reaches its peak value; thereafter the wall gradually shrinks (consistent with the fact that the energy cost increases with the length of the domain wall [24]) and undergoes a rearrangement as the phase evolves toward the opposite extremum. When the global relative phase reaches this opposite extremum, the configuration of the domain wall is inverted. For example, at $t = 9.93\,\mathrm{ms}$ the domain wall changes from approximately 0 to 2π, while at $t = 12.50\,\mathrm{ms}$ it changes from approximately 0 to -2π. At later times, when the oscillation is small around $\theta = 0$, we find that no domain walls remain in the system. It is interesting to note that the formation of domain walls occurs within the regime of rapid damping of the Josephson oscillation. This suggests that domain walls may serve as an energy-loss channel (for example, by

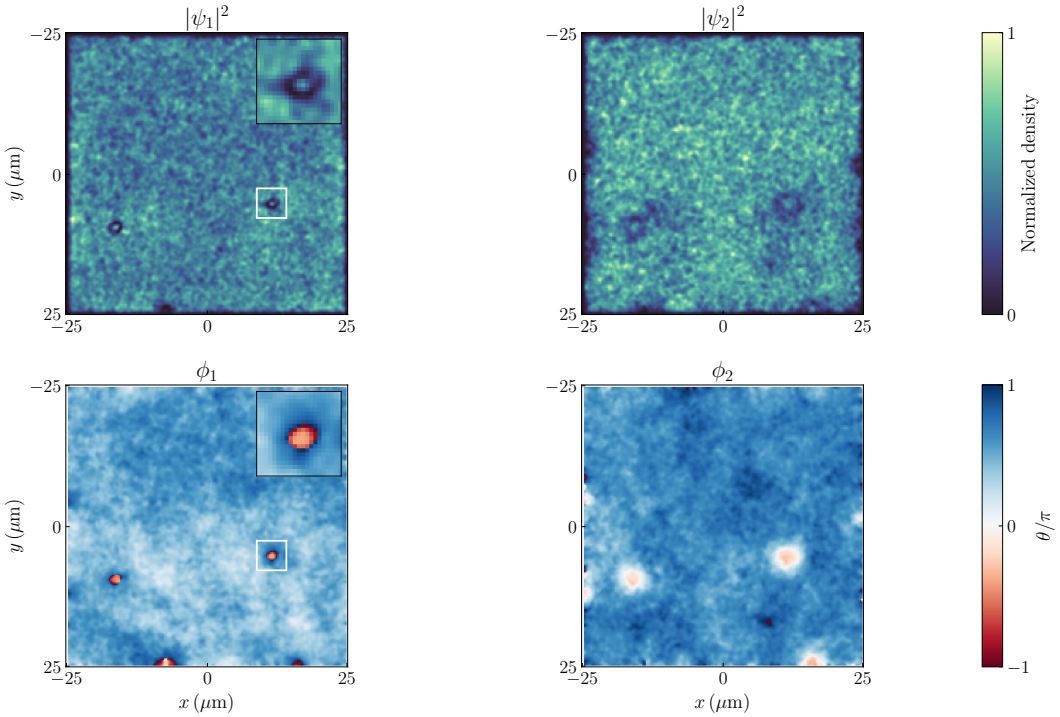

Figure 3.20: Density depletion and phase in each layer. (Top) Density profiles of Layers 1 and 2, normalized to their respective maximum values. A magnified view of the region enclosed by the white rectangle is shown in the upper-left inset. (Bottom) Wrapped phase profiles of Layers 1 and 2, with a corresponding magnified view of the same region. A Gaussian filter of $\sigma = 0.25\,\mu$m is applied.

radiating energy into phonons or into the common mode when they deform), thereby contributing to the damping of the oscillation in two-dimensional bilayer systems.

It is important to remember that topological defects can arise in tunnel-coupled two-dimensional bilayer systems. When the coupling strength is sufficiently strong and thermal fluctuations are small, a vortex–antivortex pair is expected to be connected by an open domain wall, or equivalently a finite-tension string (see Section 3.2.2). A closer examination of the domain wall dynamics reveals that a closed domain wall first shrinks and then deforms into vortices and antivortices. Subsequently, an open domain wall with a vortex–antivortex pair at its ends gradually forms and eventually reconnects to produce a new closed-loop domain wall, as shown in Figure 3.22. In this figure, a Gaussian filter with $\sigma = 1\,\text{pixel} = 0.25\,\mu$m is applied to suppress short-range noise and to eliminate tightly bound vortex–antivortex pairs, without losing essential information. Similar “domain-wall-like” structures

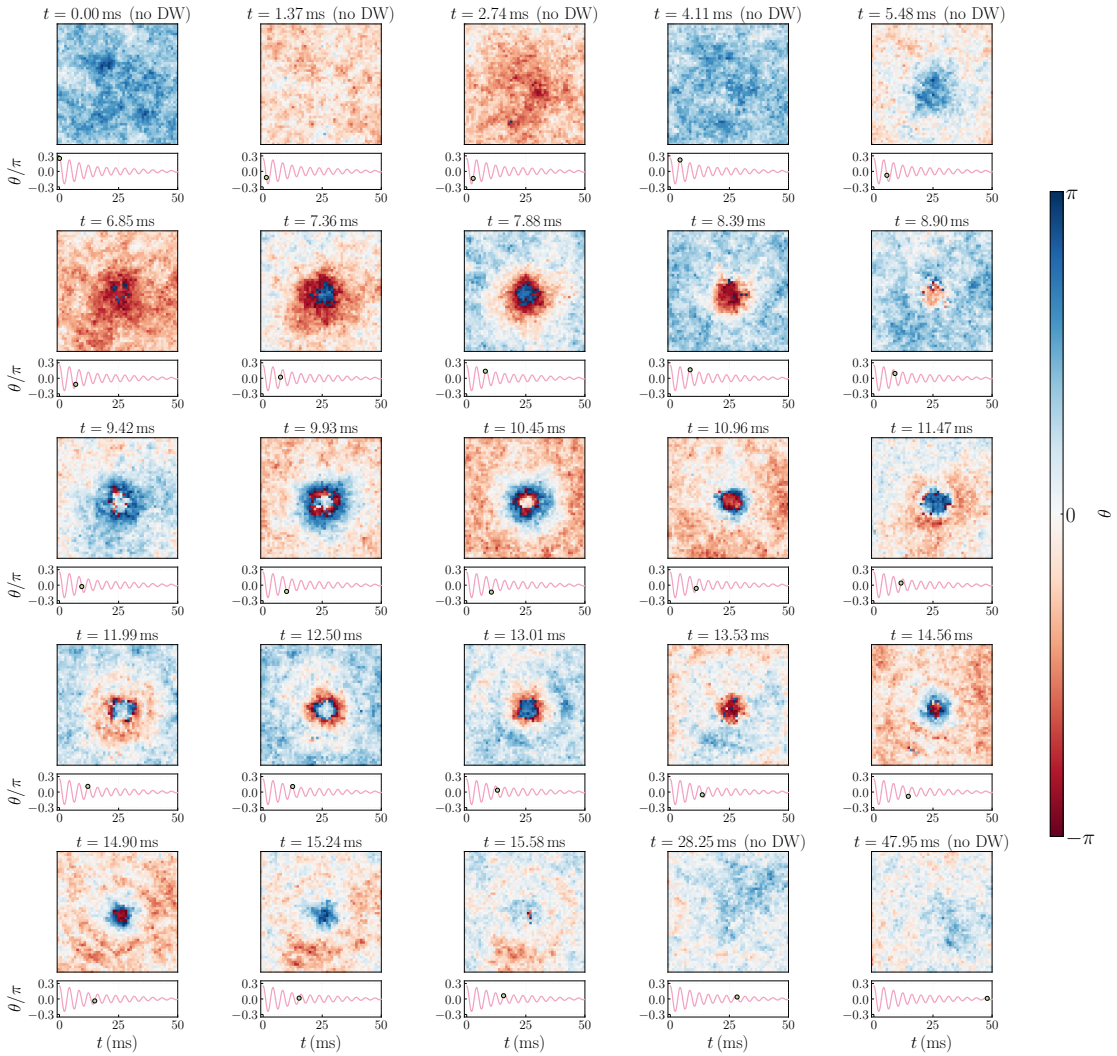

Figure 3.21: Evolution of domain wall during Josephson oscillation. Evolution of the wrapped relative phase profile in a selected region, shown together with the globally averaged relative phase oscillation (averaged over 5 samples) in the bottom panel. The corresponding time points are indicated by circular markers in the bottom panel. When no domain wall is observed in the entire field, the label "no DW" is added in the title.

can sometimes be seen in the wrapped phase of the normal two-dimensional XY model (either a single layer or a decoupled bilayer Bose gas), particularly after the application of a Gaussian blur or other coarse-graining procedure[8]. However, these features are artefacts rather than physical domain walls, since the underlying $U(1)$ symmetry does not support their formation. By contrast, we believe that the domain walls observed here are not artefacts: they appear even without any coarse-graining and, importantly, are characterized by a well-defined width as well

[8]An example is shown in Fig. 2.1 of Ref. [63].

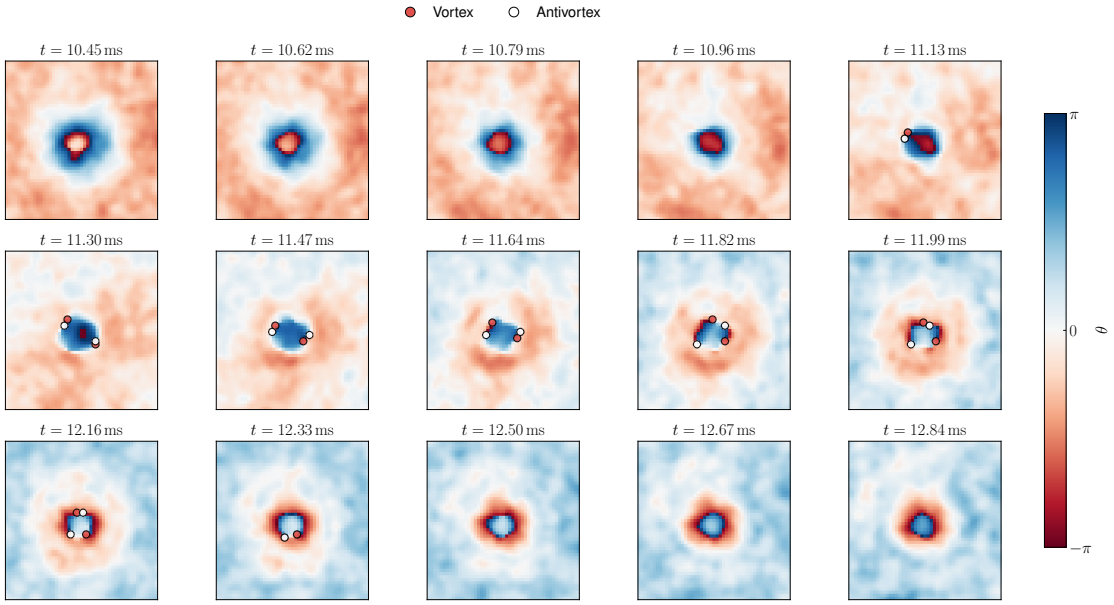

Figure 3.22: Vortices and formation of domain wall. Evolution of the wrapped relative phase profile in a selected region with vortices detected. A Gaussian filter of $\sigma = 0.25\,\mu$m is applied.

as a connection between the minima of $\cos(\theta)$ rather than random phase values.

3.3.1.4 Domain walls and topological excitations under self-trapping

Now we examine initial conditions with population imbalance and a large global phase difference, using the same data as in Figure 3.17. Interestingly, we find that large, structured domain walls start to form once the phase winding (or self-trapping) has stopped. Figure 3.23 presents snapshots of the relative phase for two different values of J_c, revealing two distinct forms of domain wall evolution. When the interlayer coupling strength is high, the domain walls break into separate segments terminated by vortex–antivortex pairs. In contrast, when the coupling is small, the domain wall shrinks rather than breaks. One possible reason for this behavior is that the weaker coupling is insufficient to form linearly confined vortex–antivortex pairs, thereby suppressing the formation of open domain walls and preventing the breaking process. For stronger coupling, however, nonequilibrium excitations can generate vortex–antivortex pairs more rapidly than the wall can retract, so that wall breaking occurs on a shorter timescale than shrinking. In addition, we again observe that the width of domain walls is larger for smaller values of J_c, as expected.

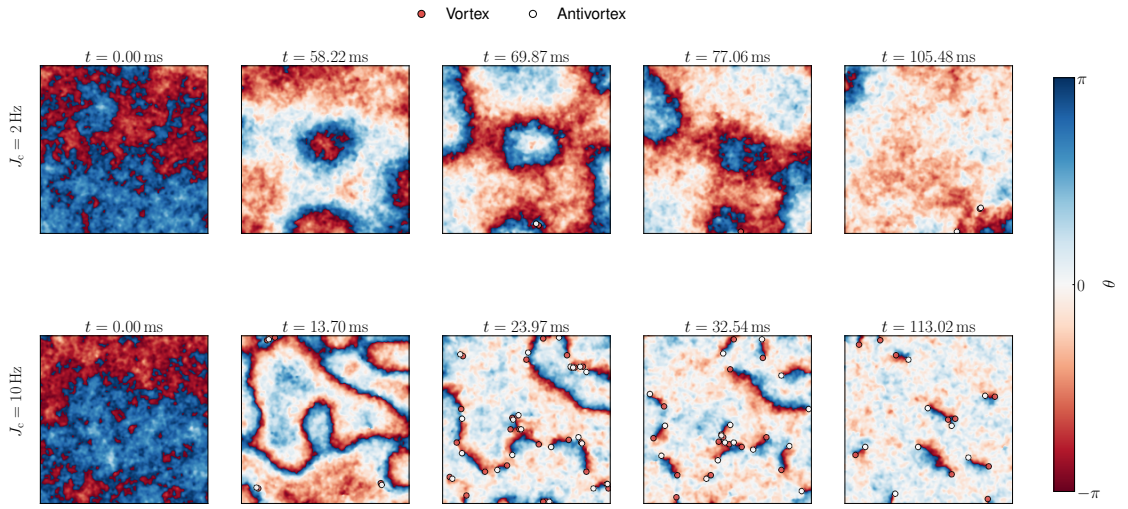

Figure 3.23: Domain walls with initial population imbalance. Wrapped relative phase profiles without coarse-graining are shown at different times for two values of the coupling strength J_c. A Gaussian filter with $\sigma = 0.25\,\mu$m is applied to the fields before the vortex detection. The profiles at $t = 0$ differ because different realizations are used for the plot.

In Figure 3.24, we present the evolution of the vortex density detected in the relative phase. Initially, no vortices are observed, as the system starts deep in the superfluid regime, and this remains the case during the self-trapping dynamics. Vortices are generated subsequently, with the onset and number depending on the coupling strength: stronger coupling produces vortices more rapidly and in larger numbers due to the breaking of closed-loop domain walls. By comparing the time at which self-trapping stops with the evolution of vortices, we find that self-trapping ends when the vortex number is still very low. This suggests that the mechanism responsible for interrupting self-trapping is not vortex proliferation but rather another process.

The number of vortices then decreases as the system relaxes. We identify two main decay pathways: vortex–antivortex pairs confined by domain walls (or strings) either move to the boundary of the cloud and vanish, or distinct pairs confined by walls meet and merge (or fuse) to form a new pair. The latter process dominates the initial decay of vortices immediately after the breaking of the walls. The merging occurs when a vortex in one well approaches an antivortex in the other well. At the

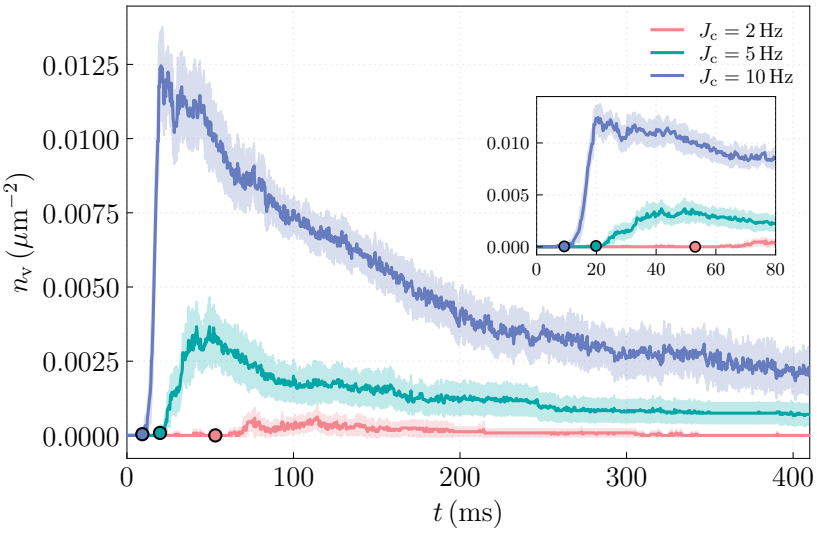

Figure 3.24: Excitation and relaxation of vortices with initial population imbalance. Vortex density in the relative phase as a function of evolution time for three coupling strengths J_c. Solid lines show the mean density obtained from ten realizations, while shaded regions indicate the standard error. Circle markers denote the times at which the global relative phase stops to wind monotonically, together with the corresponding vortex densities. The inset shows a zoomed-in view for the first 80 ms. A Gaussian filter with $\sigma = 0.25$ μm is applied to the field for vortex detection, and the density is obtained by averaging over ten realizations at each time step.

same time, we also observe long-lived confined vortex–antivortex pairs connected by domain walls (for $J_c = 5$, 10 Hz), indicating that these excitations are metastable.

Next, we track the evolution of the total domain-wall length within a single phase profile, as shown in Figure 3.25a. The total wall length averaged over ten realizations is presented as a function of time in Figure 3.25b. We find that stronger coupling strengths result in domain walls with longer total lengths. Before the self-trapping stops, domain walls have already formed for all values of J_c, during which the self-trapping persists but becomes damped. The end of self-trapping is accompanied by the formation of large domain walls. This suggests that the domain walls likely act as a main energy dissipation channel, thereby interrupting the self-trapping dynamics. At later times, we observe statistically long-lived domain walls (non-zero total domain wall length), consistent with the vortex statistics.

By comparing Figure 3.24 and Figure 3.25, we find that the number of vortices remains distinct for $J_c = 5$, 10 Hz, whereas the statistical total length of domain

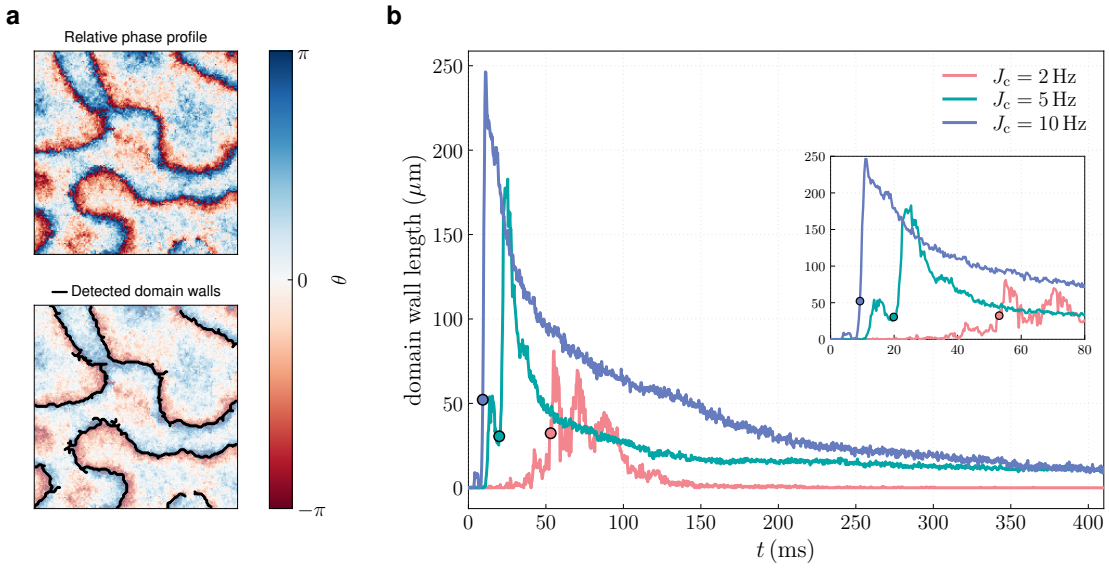

Figure 3.25: Domain wall length detection. (**a**) Relative phase profile with detected domain walls indicated by black solid lines. (**b**) Total domain wall length as a function of evolution time for three coupling strengths J_c. Circular markers denote the times at which the global relative phase stops to wind monotonically, as in Figure 3.24. The inset shows a zoomed-in view for the first 80 ms. The length of the domain wall is estimated by summing up the detected wall pixels, and then multiply it with the grid size 0.25 μm.

walls for the two coupling strengths becomes comparable. This suggests that at higher J_c, the domain walls tend to fragment into smaller segments on average. This behavior is expected, as the linear confinement potential scales proportionally to $\sqrt{J_c}$. A simple way to understand these metastable confined vortex–antivortex pairs is to consider the the relative phase alone, neglecting or assuming weak coupling to the common modes. In this picture, the free energy of a confined vortex–antivortex pair separated by a distance R at finite temperature T can be approximated as

$$F \approx \alpha\sqrt{J_c}R - 2k_B T \ln\left(\frac{R}{\xi}\right), \tag{3.51}$$

where α is a proportionality constant and ξ denotes the healing length. We only consider the regime $\xi < R \ll L$, with L the system size. The free energy exhibits a stationary point at $R_0 = 2k_B T/\alpha\sqrt{J_c}$. For $R < R_0$, the free energy decreases with increasing R, while for $R > R_0$ it increases with increasing R, indicating a metastable equilibrium separation between the vortex and antivortex pair.

We estimate the separation of confined vortex–antivortex pairs at time t as $2L_{DW}(t)/N_v(t)$, where $L_{DW}(t)$ denotes the total length of the detected domain walls

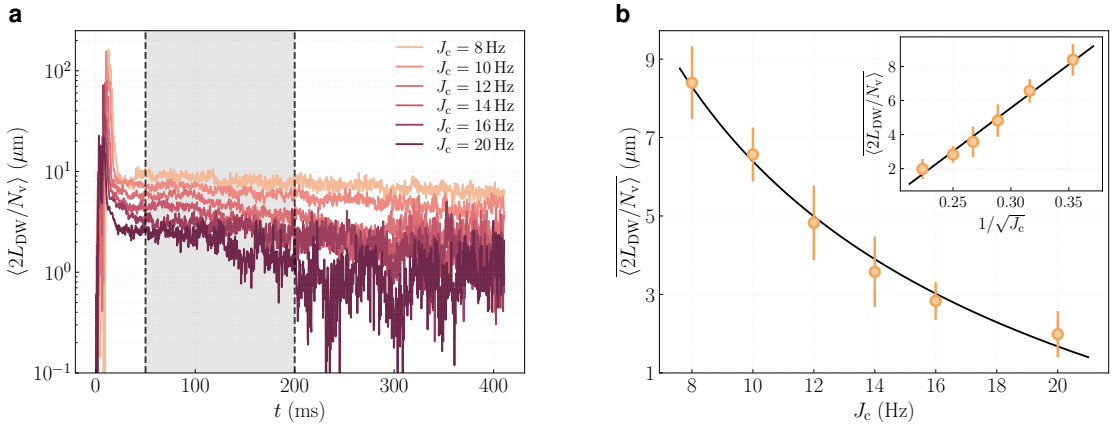

Figure 3.26: Average separation of confined vortex–antivortex pairs. (**a**) Time evolution of the mean separation distance for different tunnel-coupling strengths J_c. The vertical axis is shown on a logarithmic scale. (**b**) Separation distance averaged over the interval $t = 50$–200 ms (shaded region in (**a**)) as a function of J_c. The solid black line shows a fit to the model $y = a/\sqrt{x} + b$, yielding $b \approx -9.7$. The inset displays the same data and fit plotted against $1/\sqrt{J_c}$.

and $N_v(t)$ the number of detected vortices. Following the fragmentation of the domain wall, the mean separation rapidly decreases and subsequently approaches a quasi-steady value. Furthermore, increasing the coupling strength J_c results in a systematic reduction of the pair separation, as shown in Fig. 3.26a. Figure 3.26b displays the time-averaged separation, $\overline{2L_{DW}(t)/N_v(t)}$, evaluated over the interval during which the separation distance remains approximately stationary, as a function of J_c. We observe that the mean separation of confined vortex-antivortex pairs scales as $1/\sqrt{J_c}$, in agreement with the free energy argument. However, the fit yields a non-zero offset b. This residual constant may arise from uncertainties in the numerical estimation of the separation distance, or from physical effects not captured by Eq. (3.51), such as finite-size corrections or density fluctuations.

3.3.1.5 Classification of confined vortex-antivortex paris

The confined vortex–antivortex pairs in the relative phase can originate from several distinct configurations:

- $V_1|AV_1$: a vortex–antivortex pair in ψ_1,
- $V_2|AV_2$: a vortex–antivortex pair in ψ_2,

- $V_1|V_2$: a vortex in ψ_1 and another vortex in ψ_2,
- $AV_1|AV_2$: an antivortex in ψ_1 and another antivortex in ψ_2.

In a two-component Josephson-coupled bilayer system, similar configurations have been proposed as analogues of hadrons in $SU(2)$ quantum chromodynamics (QCD) [87, 88]. The $V_1|V_2$ and $AV_1|AV_2$ configurations are analogous to baryons, while $V_1|AV_1$ and $V_2|AV_2$ correspond to mesons. The baryons are found to rotate and mesons move translationally. In our system, the situation differs because it is not a two-component gas; hence, there is no intercomponent atom-atom interaction ($g_{12} = 0$), and the dynamics are considered at finite temperature. Nevertheless, we observe similar behavior: "baryon-type" pairs rotate, while "meson-type" pairs undergo translational motion.

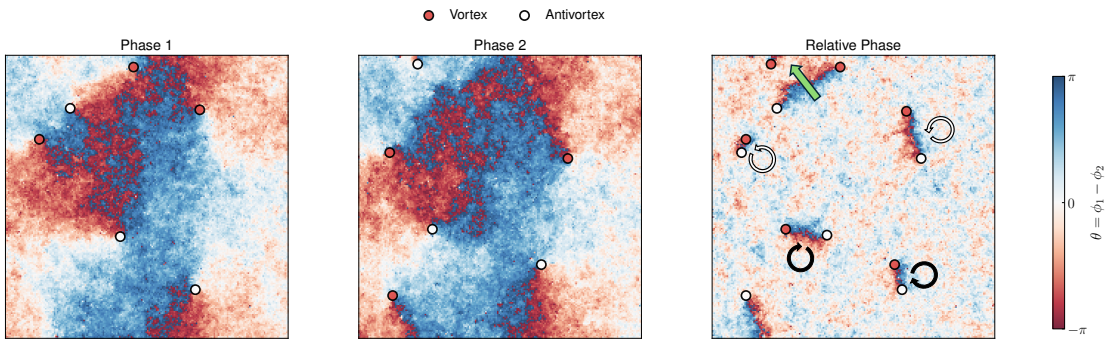

Figure 3.27: Classification and motion of confined vortices. Vortices and antivortices detected in phase 1 (ϕ_1), phase 2 (ϕ_2), and the relative phase (θ). Different types of motion of confined vortex–antivortex pairs in the relative phase are indicated: counterclockwise rotation (white curved arrow), clockwise rotation (black curved arrow), and translational motion (green straight arrow).

To track the motion of confined vortex–antivortex pairs, we focus on late times at a coupling strength of $J_c = 10$ Hz, when only a few pairs remain. The background relative phase is locked at $\theta = 0$, with only residual thermal fluctuations, providing a clean background for tracking vortex motion. We find that, for a given coupling strength, the direction of rotation depends on whether the configuration is $V_1|V_2$ or $AV_1|AV_2$ across the layers, as shown in Figure 3.27. The $V_1|V_2$ bounds rotate counterclockwise while the $AV_1|AV_2$ bounds rotate clockwise. [9]

[9] One can consider $V_1|V_2$ and $AV_1|AV_2$ as baryon and antibaryon.

The $V_1|AV_1$ bounds move translationally without rotation. Therefore, we can conclude that the (statistically) long-lived confined pairs are the rotating pairs (i.e.,$V_1|V_2$ and $AV_1|AV_2$).

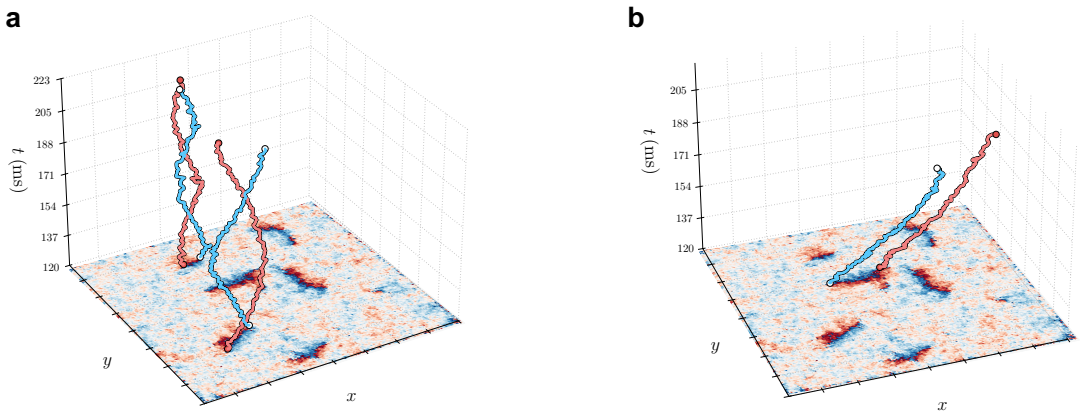

Figure 3.28: Motion of confined vortices. Three-dimensional representations of the trajectories of selected confined vortex–antivortex pairs. The x–y coordinates indicate the spatial positions of the pairs, while the z axis represents time. (**a**) Confined vortex–antivortex pairs exhibit rotational motion. (**b**) Confined vortex–antivortex pairs translate without rotation.

Figure 3.28 visualizes the time evolution of confined vortex–antivortex pairs, which exhibit either rotational or translational motion. We note that the rotation period depends on the separation between the vortex and antivortex: larger separations lead to slower rotation (see Figure 3.28a), consistent with the behaviour observed in the two-component case [87].

In addition, complicated dynamical transformations between rotating and translating pairs are observed, as previously studied in an ideal scenario for a two-component system [88]. For example, two rotating pairs can merge to form two translating pairs, or just one translating pair.

3.4 Conclusion

In this chapter, we discuss different numerical simulation methods for 2D Bose gases at finite temperature. We first show that the stochastic Ornstein–Uhlenbeck process can be used to generate phase profiles for both homogeneous and inhomogeneous

2D Bose clouds in the superfluid regime. As a natural extension, the relative phase in a tunnel-coupled bilayer system can also be simulated within the quadratic approximation. However, this stochastic approach captures only phonon-like excitations and cannot describe vortices. To overcome this limitation, we introduce the classical-field Monte Carlo method, which can be broadly applied to simulate finite-temperature systems. We employ this method to study the equilibrium properties of bilayer Bose gases, including the phase correlation function and vortex statistics. We further construct phase diagrams for bilayer systems with two-body interlayer coupling, illustrating the coupling dependence of the critical PSD. In addition, we confirm the existence of a paired BKT phase in bilayers with four-body interlayer coupling, showing that it originates from the binding of vortices and antivortices across different layers. Finally, we investigate the Josephson effects by combining Monte Carlo sampling with the Gross–Pitaevskii equations, finding that the damping of the oscillations most likely originates from sine–Gordon solitons (domain walls). We then classify the different types of confined vortex–antivortex pairs and demonstrate their distinct dynamics.

4

Experiment Apparatus and Realization of Bilayer 2D cloud

Contents

In this chapter, we begin with a brief overview of the multiple-radiofrequency dressed double-well potential employed to trap and realise quasi-two-dimensional ultracold bilayer Bose gases. We show that the double-well potential can be calculated numerically within the semi-classical approximation using Floquet theory, and illustrate how its shape can be manipulated. We then describe the experimental apparatus and sequence employed for cooling, loading, and imaging atoms in the double-well potential.

4.1 RF-dressed double-well potential

4.1.1 Atoms in a weak magnetic field

We consider a particle in a magnetic field $\mathbf{B}$. Its magnetic dipole interaction Hamiltonian is

$$\mathcal{H} = -\boldsymbol{\mu} \cdot \mathbf{B} \,, \tag{4.1}$$

where $\boldsymbol{\mu}$ is the magnetic moment. For an atom in an external magnetic field $\mathbf{B}_{\text{ext}}$, the magnetic and electric dipole interaction Hamiltonian can be written as [89]

$$\mathcal{H}_{\text{HFS}} = V_{\text{HFS}} + V_{\text{J}} + V_{\text{I}} + V_{\text{Q}} \simeq A_{\text{J}}\, \hat{\mathbf{I}} \cdot \hat{\mathbf{J}} + g_{\text{J}} \mu_{\text{B}}\, \hat{\mathbf{J}} \cdot \mathbf{B}_{\text{ext}} - g_{\text{I}} \mu_{\text{N}}\, \hat{\mathbf{I}} \cdot \mathbf{B}_{\text{ext}} \,, \tag{4.2}$$

where $\hat{\mathbf{I}}$ is the nuclear spin operator and $\hat{\mathbf{J}}$ is the electronic total angular momentum operator, g denotes the Landé g factor, μ_B and μ_N are the Bohr magneton and the nuclear magneton, respectively. The term $V_{\text{HFS}} = A_{\text{J}}\, \hat{\mathbf{I}} \cdot \hat{\mathbf{J}}$ is the hyperfine interaction with hyperfine constant A_J, while $V_{\text{J}} = g_{\text{J}} \mu_B\, \hat{\mathbf{J}} \cdot \mathbf{B}_{\text{ext}}$ and $V_{\text{I}} = g_{\text{I}} \mu_N\, \hat{\mathbf{I}} \cdot \mathbf{B}_{\text{ext}}$ describe the coupling of the electronic and nuclear magnetic moments to the field. We neglect V_{Q}, which represents the electronic quadrupole interaction energy, as it is typically much smaller than the other magnetic contributions [89].

In the absence of an external field ($\mathbf{B}_{\text{ext}} = 0$), it is convenient to introduce the total angular momentum operator $\hat{\mathbf{F}} = \hat{\mathbf{I}} + \hat{\mathbf{J}}$, which is conserved in a closed system since no external torque acts on the atom. The operator $V_{\text{HFS}} = A_J\, \hat{\mathbf{I}} \cdot \hat{\mathbf{J}}$ is then diagonalised in the basis $|I, J, F, m_F\rangle$. Moreover, if the external field is weak[1] in the sense that $g_{\text{J}} \mu_{\text{B}} B_{\text{ext}} \ll A_{\text{J}}$, the Zeeman terms can be treated as a perturbation of V_{HFS} so that $\mathbf{I}$ and $\mathbf{J}$ remain strongly coupled [89, 90]. Therefore F is still a good quantum number in a weak magnetic field. To first order in perturbation theory one has the effective relation

$$g_{\text{J}} \mu_{\text{B}}\, \hat{\mathbf{J}} \cdot \mathbf{B}_{\text{ext}} - g_{\text{I}} \mu_{\text{N}}\, \hat{\mathbf{I}} \cdot \mathbf{B}_{\text{ext}} = g_{\text{F}} \mu_{\text{B}}\, \hat{\mathbf{F}} \cdot \mathbf{B}_{\text{ext}} \,, \tag{4.3}$$

[1] Throughout this section, the applied dc magnetic field is assumed to remain within the weak-field regime.

where

$$g_{\mathrm{F}} = g_{\mathrm{J}} \frac{F(F+1)+J(J+1)-I(I+1)}{2F(F+1)} - g_{\mathrm{I}} \frac{m}{M} \frac{F(F+1)+I(I+1)-J(J+1)}{2F(F+1)} \\ \approx g_{\mathrm{J}} \frac{F(F+1)+J(J+1)-I(I+1)}{2F(F+1)} \, . \tag{4.4}$$

The approximation from the first to the second line in Eq. (4.4) follows from neglecting the term proportional to $g_{\mathrm{I}} m/M$, which is approximately three orders of magnitude smaller than g_{J} [89]. For a weak external magnetic field, Eq. (4.2) can therefore be written as

$$\mathcal{H}_{\mathrm{HFS}} = A_{\mathrm{J}} \, \hat{\mathbf{I}} \cdot \hat{\mathbf{J}} + g_{\mathrm{F}} \mu_{\mathrm{B}} \, \hat{\mathbf{F}} \cdot \mathbf{B}_{\mathrm{ext}} \, , \tag{4.5}$$

where the second term corresponds to the Zeeman interaction. For a given hyperfine level, the hyperfine structure term is constant, so only the Zeeman interaction needs to be considered. Furthermore, in the presence of a magnetic-field gradient (i.e. when the field strength varies spatially), this interaction can provide a trapping potential for atoms. An example is the static quadrupole magnetic field, defined as

$$\mathbf{B}_{\mathrm{quad}} = b \, (x \mathbf{e}_x + y \mathbf{e}_y - 2z \mathbf{e}_z) \, , \tag{4.6}$$

where b is the magnetic-field gradient (in units of T/m). For this cylindrically symmetric quadrupole field, the interaction Hamiltonian

$$\mathcal{H}_{\mathrm{int}} = g_{\mathrm{F}} \mu_{\mathrm{B}} \, \hat{\mathbf{F}} \cdot \mathbf{B}_{\mathrm{quad}} \, , \tag{4.7}$$

can be evaluated more conveniently by transforming to a new coordinate system. We define

$$x = r \cos\phi \sin\theta \, , \qquad y = r \sin\phi \sin\theta \, , \qquad 2z = r \cos\theta \, , \tag{4.8a}$$

$$r = \sqrt{x^2+y^2+4z^2} \, , \quad \cos\theta = \frac{2z}{\sqrt{x^2+y^2+4z^2}} \, , \quad \cos\phi = \frac{x}{\sqrt{x^2+y^2}} \, . \tag{4.8b}$$

Then the relation between the old and new coordinate systems can be expressed through the transformation matrix

$$\mathbf{R} = \begin{pmatrix} \cos\theta\cos\phi & \sin\phi & \sin\theta\cos\phi \\ \cos\theta\sin\phi & -\cos\phi & \sin\theta\sin\phi \\ \sin\theta & 0 & -\cos\theta \end{pmatrix} \, , \tag{4.9}$$

which transforms the unit vectors as

$$\begin{pmatrix} \mathbf{e}_x \\ \mathbf{e}_y \\ \mathbf{e}_z \end{pmatrix} = \mathbf{R} \begin{pmatrix} \mathbf{e}_\theta \\ \mathbf{e}_\phi \\ \mathbf{e}_r \end{pmatrix} , \tag{4.10a}$$

and

$$\begin{pmatrix} \mathbf{e}_\theta \\ \mathbf{e}_\phi \\ \mathbf{e}_r \end{pmatrix} = \mathbf{R}^{-1} \begin{pmatrix} \mathbf{e}_x \\ \mathbf{e}_y \\ \mathbf{e}_z \end{pmatrix} . \tag{4.10b}$$

In this new coordinate system, the quadrupole field can be written simply as

$$\mathbf{B}_{\text{quad}} = b\, r\, \mathbf{e}_r, \tag{4.11}$$

which leads to the Zeeman Hamiltonian

$$\mathcal{H}_{\text{Zeeman}} = g_{\text{F}} \mu_{\text{B}}\, \hat{\mathbf{F}} \cdot \mathbf{B}_{\text{quad}} = g_{\text{F}} \mu_{\text{B}}\, b\, r\, \hat{F}_r. \tag{4.12}$$

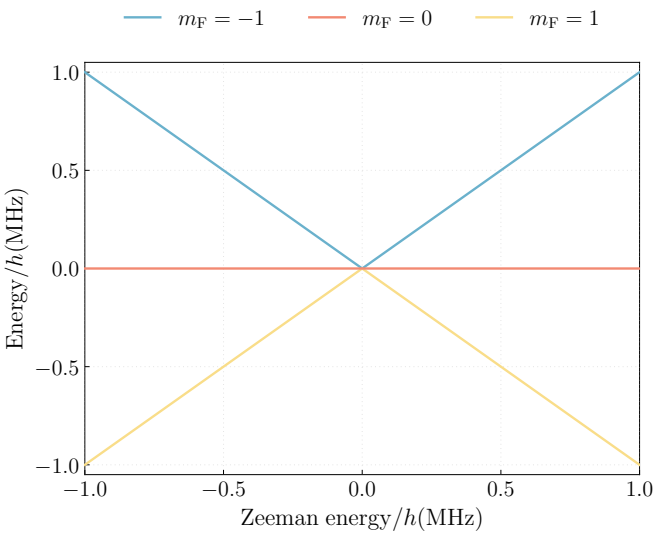

Figure 4.1: Zeeman energy shifts of different m_{F} states. Energy/h as a function of the Zeeman energy/h. The red line corresponds to the state $|m_{\text{F}} = 0\rangle$, while the blue and yellow lines represent $|m_{\text{F}} = -1\rangle$ and $|m_{\text{F}} = +1\rangle$, respectively. Atoms in the $|m_{\text{F}} = -1\rangle$ state act as low-field seekers and can be magnetically trapped. The x-axis Zeeman energy is given by $E_{\text{Zeeman}}/h = g_{\text{F}}\mu_{\text{B}} bz/(2\pi)$, for $\phi = 0$ and $\theta = \pi$.

The eigenstates of this Hamiltonian are $|m_F\rangle$, where m_F is the eigenvalue of $\hat{F}_r$, defined by $\hat{F}_r\,|m_{\text{F}}\rangle = m_{\text{F}}\,|m_{\text{F}}\rangle$. Physically, m_{F} is the quantum number associated with the projection of the total angular momentum onto the quantization axis set

by the local quadrupole magnetic field. For the ^{87}Rb atoms used in our experiments, which are trapped in the $5s\,^2S_{1/2}$ ground state with $F = 1$ ($g_{\rm F} = -\frac{1}{2}$), the allowed values of $m_{\rm F}$ are $-1, 0, 1$. The corresponding energy $E = m_{\rm F} g_{\rm F} \mu_{\rm B}\, b\, r$, is position dependent and forms a trapping potential for $m_F = -1$, as illustrated in Figure 4.1. However, the energy levels cross at the centre of the trap, where the magnetic field strength vanishes. At this point atoms may undergo Majorana spin-flip transitions to untrapped states, causing loss from the trap. A common way to suppress such losses is to apply a strong time-varying radio-frequency (RF) field.

4.1.2 Interaction between atoms and RF field

As discussed earlier, Majorana spin-flip loss in a quadrupole trap can be suppressed by applying a sufficiently strong RF field. To analyse this effect rigorously, we first consider the fully quantised description. Assume a quantised single-frequency RF field $\hat{\mathbf{B}}_{\rm RF}$, represented as a second-quantised operator. The corresponding quantised dressed-atom Hamiltonian can be written as [91]

$$\hat{H} = \hat{H}_{\rm field} + \hat{H}_{\rm atom} + \hat{H}_{\rm int} = \omega \hat{a}^\dagger \hat{a} + g_F \mu_B b\, r \hat{F}_r + g_F \mu_B \hat{\mathbf{F}} \cdot \hat{\mathbf{B}}_{\rm RF} \ , \tag{4.13}$$

where the three contributions are

$$\hat{H}_{\rm atom} = g_F \mu_B b\, r \hat{F}_r \ , \tag{4.14a}$$

$$\hat{H}_{\rm field} = \omega \hat{a}^\dagger \hat{a} \ , \tag{4.14b}$$

$$\hat{H}_{\rm int} = g_{\rm F} \mu_{\rm B} \hat{\mathbf{F}} \cdot \hat{\mathbf{B}}_{\rm RF} \ . \tag{4.14c}$$

Here ω is the RF field frequency, and the zero-point energy term $\hbar\omega/2$ in Eq (4.14b) has been omitted since it only adds a constant energy offset. Throughout this discussion we set $\hbar = 1$, which corresponds to measuring the Hamiltonian in units of $E/\hbar$. It is also useful to note that $\langle \alpha(t)| \hat{\mathbf{B}}_{\rm RF} |\alpha(t)\rangle = \mathbf{B}_{\rm exp}(t)$ for $\alpha \gg 1$, where $\mathbf{B}_{\rm exp}(t)$ is the experimentally applied RF field, treated classically [92]. Because the spatial variation of the RF field is negligible on the scale of the atom, we consider it as a purely time dependent variable [92].

Using the quantised expression for the magnetic field, the interaction Hamiltonian in the coordinate system defined by Eq. (4.8) takes the form

$$\hat{H}_{\text{int}} = g_{\text{F}}\mu_{\text{B}}\mathcal{E}\left(\frac{\beta}{\sqrt{2}}\hat{F}_{+} + \frac{\alpha}{\sqrt{2}}\hat{F}_{-} + \zeta\hat{F}_{r}\right)\hat{a}^{\dagger} + \text{H.c.}\,, \tag{4.15}$$

where $\hat{F}_{+} = \hat{F}_{\theta} + i\hat{F}_{\phi}$ and $\hat{F}_{-} = \hat{F}_{\theta} - i\hat{F}_{\phi}$ are the angular momentum raising and lowering operators, and $\mathcal{E} = \sqrt{\omega/(2\varepsilon_0 V)}$, with ε_0 the vacuum permittivity and V the volume. The coefficients are defined by

$$\alpha = \frac{1}{\sqrt{2+2\kappa}}\left[\cos\theta\cos\phi - \kappa\cos\phi + i\left(\kappa\cos\theta\sin\phi + \sin\phi\right)\right]\,, \tag{4.16a}$$

$$\beta = \frac{1}{\sqrt{2+2\kappa}}\left[\cos\theta\cos\phi + \kappa\cos\phi + i\left(\kappa\cos\theta\sin\phi - \sin\phi\right)\right]\,, \tag{4.16b}$$

$$\zeta = \frac{1}{\sqrt{1+\kappa}}\left(\sin\theta\cos\phi + i\kappa\sin\phi\sin\theta\right)\,, \tag{4.16c}$$

with $|\alpha|^2 + |\beta|^2 + |\zeta|^2 = 1$. The parameter κ specifies the RF field polarisation: $\kappa = 1$ corresponds to circular polarisation, while $\kappa = 0$ corresponds to linear polarisation. This Hamiltonian form follows from choosing the static quadrupole field as the quantisation axis.

The eigenvalues of this Hamiltonian can be obtained analytically within the rotating-wave approximation (RWA) for circularly polarised RF fields [93, 94]. For linearly polarised RF fields, however, analytical diagonalisation is difficult, requiring numerical techniques. A standard approach employs the Floquet theory within a semi-classical framework, which provides solutions of arbitrary precision and, importantly, can be generalised naturally to RF fields with multiple frequency components [95, 96].

To obtain the semi-classical Hamiltonian, we first transform the Hamiltonian into the interaction picture, where operators are defined as $\hat{A}_{\text{I}} = U^{\dagger}\hat{A}_{\text{S}}U$, with $U = \exp\left[-i\hat{H}_0 t\right] = \exp\left[-i\hat{a}^{\dagger}\hat{a}\,\omega t\right]$. In this representation, the interaction Hamiltonian becomes explicitly time dependent,

$$\hat{H}_{\text{int}}(t) = g_F\mu_B\mathcal{E}\left(\frac{\beta}{\sqrt{2}}\hat{F}_{+} + \frac{\alpha}{\sqrt{2}}\hat{F}_{-} + \zeta\hat{F}_{r}\right)\hat{a}^{\dagger}e^{i\omega t} + \text{H.c.} \tag{4.17}$$

We then define a classical RF field of the form

$$\begin{aligned}\mathbf{B}_{\mathrm{RF}}(t) &= B_0 \frac{\cos(\omega t)\,\mathbf{e}_x - \kappa \sin(\omega t)\,\mathbf{e}_y}{\sqrt{1+\kappa}} \\ &= \frac{B_0}{2}\left(\mathbf{e}e^{-i\omega t} + \text{c.c.}\right) ,\end{aligned} \tag{4.18}$$

where $\mathbf{e} = \frac{1}{\sqrt{1+\kappa}}\left(\mathbf{e}_x - i\kappa \mathbf{e}_y\right)$ is the polarisation unit vector. Using the relation $\langle\alpha(t)|\,\hat{\mathbf{B}}_{\mathrm{RF}}\,|\alpha(t)\rangle = \mathbf{B}_{\mathrm{RF}}(t)$, we obtain $\mathcal{E}\langle\hat{a}\rangle = \mathcal{E}\langle\hat{a}^\dagger\rangle = B_0/2$. In the strong coherent-field limit, the mean photon number is large while the relative fluctuations around this value are negligible. Consequently, $\mathcal{E}\hat{a}$ and $\mathcal{E}\hat{a}^\dagger$ may be replaced by their expectation value $B_0/2$ in the semi-classical approximation. Substituting this result into the interaction Hamiltonian and combining it with Eq. (4.14a) and Eq. (4.11), we obtain the full semi-classical Hamiltonian in the interaction picture:

$$\hat{V}(t) = g_F \mu_B b\, r \hat{F}_r + \frac{g_F \mu_B}{2}\left[\left(\frac{\beta}{\sqrt{2}}\hat{F}_+ + \frac{\alpha}{\sqrt{2}}\hat{F}_- + \zeta \hat{F}_r\right) B_0 e^{i\omega t} + \text{H.c.}\right] . \tag{4.19}$$

If the RF field is linearly polarised ($\kappa = 0$), Eq. (4.19) simplifies to

$$\begin{aligned}\hat{V}(t) &= g_F \mu_B b\, r \hat{F}_r + \frac{g_F \mu_B}{2} B_0 \cos(\omega t)\Big[\left(\cos\theta\cos\phi + i\sin\phi\right)\hat{F}_- \\ &\qquad + \left(\cos\theta\cos\phi - i\sin\phi\right)\hat{F}_+ \\ &\qquad + \cos\phi\sin\theta\,\hat{F}_r\Big] \\ &= g_F \mu_B b\, r \hat{F}_r + g_F \mu_B\, \hat{\mathbf{F}} \cdot \left[B_0 \cos(\omega t)\,\mathbf{e}_x\right] .\end{aligned} \tag{4.20}$$

We note that this expression is equivalent to that obtained by treating the RF field directly as a classical field through the interaction term $g_F \mu_B\, \hat{\mathbf{F}} \cdot \mathbf{B}_{\mathrm{RF}}(t)$, where $\mathbf{B}_{\mathrm{RF}}(t)$ is defined in Eq. (4.18).

To obtain the eigenenergies of the time-dependent Hamiltonian, we employ Floquet theory, a powerful framework for analysing quantum systems with Hamiltonians that are periodic in time, $H(t) = H(t+T)$, where the period is $T = 2\pi/\omega$. In this framework, the solutions to the time-dependent Schrödinger equation take the form

$$|\psi(t)\rangle = e^{-i\frac{E't}{\hbar}}|\Phi(t)\rangle, \tag{4.21}$$

where E' is the real floquet energies which is multiple of $\hbar\omega$, and $|\Phi(t)\rangle$ a function that shares the periodicity of the Hamiltonian, $|\Phi(t+T)\rangle = |\Phi(t)\rangle$. The time-evolution operator over one period, $U(0,T)$, connects the state at $t = 0$ to that

at $t = T$. This implies

$$U(0,T)|\psi(0)\rangle = e^{-iE'T/\hbar}\,|\psi(0)\rangle\ . \tag{4.22}$$

The dressed eigenenergies of the system can thus be extracted from the eigenvalues of the one-period evolution operator according to

$$E' = \frac{-i\hbar}{T}\,\log\Big(U(0,T)\Big). \tag{4.23}$$

We evaluate $U(0,T)$ by numerically integrating the Schrödinger equation in the

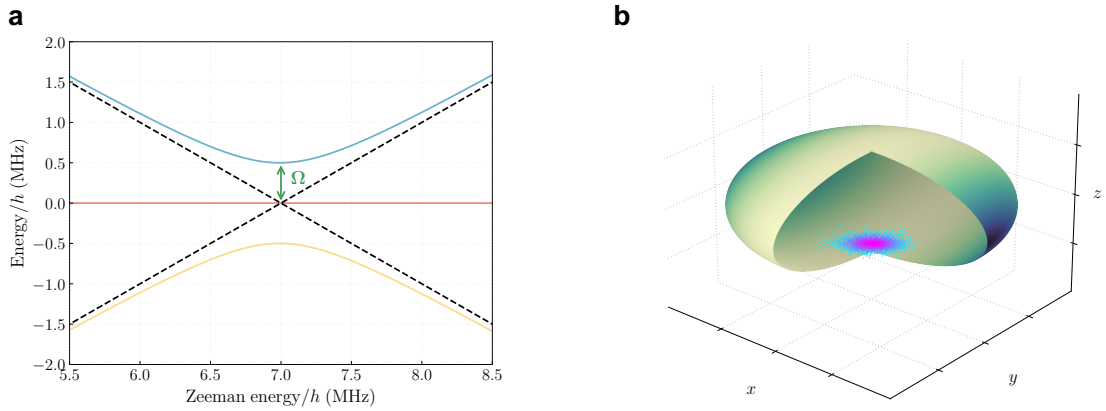

Figure 4.2: RF-dressed potential. (**a**) Solid lines show numerically calculated eigenenergies along the z-direction for a 7.0 MHz linearly polarised RF field coupled to atoms. Dashed lines represent the corresponding uncoupled eigenenergies. Both cases neglect the effect of gravity. (**b**) Three-dimensional illustration of the potential minimum for linearly polarised RF field in a quadrupole field (resonant spheroid). Atoms accumulate at the bottom of the "shell" due to gravity. The shell surface is partially cut away to show the trapped atoms.

interaction picture, and subsequently obtain the potential. The eigenvalues obtained from the Floquet calculation are shown in Figure 4.2a, where an avoided crossing is clearly visible near resonance. The trap minimum occurs at $\omega_{\text{Zeeman}} = \omega_{\text{RF}} = 2\pi \times 7.0\,\text{MHz}$, indicating that the trapping position can be controlled by adjusting the frequency of the RF field. The energy gap at the avoided crossing corresponds to the Rabi frequency Ω (in the figure, $\Omega/2\pi$ is indicated by the arrow, and the factor of 2π is omitted), which is proportional to the amplitude of the RF field. Consequently, the shape of the trapping potential can be tuned by varying the RF

field strength. The potential minimum of this potential, known as the resonant spheroid, forms a "shell" in space (as $E_{\text{Zeeman}} \propto r$), and atoms are trapped at the bottom of this shell under the influence of gravity (see Figure 4.2b).

The spatial distribution of the (angular) Rabi frequency $\Omega(\mathbf{r})$, which quantifies the coupling strength over the resonance spheroid, is given by [96–98]

$$\begin{aligned}\Omega_{\text{circular}}(\mathbf{r}) &= \frac{g_{\text{F}}\mu_{\text{B}}B_0}{2\hbar}\left(1 - \frac{2z}{\sqrt{x^2+y^2+4z^2}}\right) \\ &= \frac{g_{\text{F}}\mu_{\text{B}}B_0}{2\hbar}\left(1-\cos\theta\right) \ ,\end{aligned} \tag{4.24}$$

for a circularly polarised RF field in the x–y plane. The second line of Eq. (4.24) is obtained by rewriting the Rabi frequency in spherical coordinates as defined in Eq. (4.8). It is easy to see that the maximum coupling strength occurs at the bottom of the shell, where $\Omega_{\text{max}} = g_{\text{F}}\mu_{\text{B}}B_0/\hbar$, while a node ($\Omega_{\text{circular}}(\mathbf{r}) = 0$) appears at the top, as shown in Figure 4.3a.

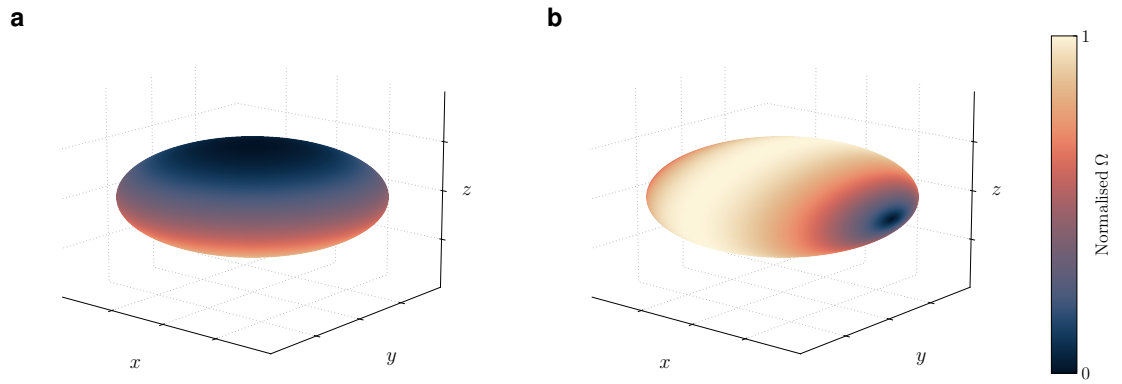

Figure 4.3: Spatial distribution of the coupling strength. Calculated Rabi frequency Ω on the resonant spheroid for (**a**) a circularly polarised RF field in the x–y plane, and (**b**) a linearly polarised RF field along the x-axis.

For a linearly polarised RF field in the x–y plane, the coupling takes the form [96–98]

$$\Omega_{\text{linear}}(\mathbf{r}) = \frac{g_{\text{F}}\mu_{\text{B}}B_0}{2\hbar}\sqrt{\frac{r_\perp^2+4z^2}{r_\perp^2+r_\parallel^2+4z^2}} \ , \tag{4.25}$$

where $r_\perp$ and $r_\parallel$ denote the coordinates perpendicular and parallel to the polarisation axis, respectively. For simplicity, but without loss of generality, we consider the

case of linear polarisation along the x-direction. We obtain

$$\begin{aligned}\Omega_{\text{linear}}(\mathbf{r}) &= \frac{g_{\text{F}}\mu_{\text{B}}B_0}{2\hbar}\sqrt{\frac{y^2+4z^2}{x^2+y^2+4z^2}} \\ &= \frac{g_{\text{F}}\mu_{\text{B}}B_0}{2\hbar}\sqrt{\sin^2\phi\,(1-\cos^2\theta)+\cos^2\theta}\,.\end{aligned} \tag{4.26}$$

In this case, we can see the maximum coupling $\Omega_{\text{max}} = g_{\text{F}}\mu_{\text{B}}B_0/2\hbar$ is found along the contour $\phi = \pi/2$, while nodes appear at $\theta = \pi/2$ with $\phi = 0$ or π, as illustrated in Figure 4.3b.

At the bottom of the resonant spheroid, where atoms are confined by gravity, the adiabatic potential may be expanded to second order about its minimum to obtain the local harmonic frequencies. For a circularly polarised RF field the trap frequencies are [97]

$$\begin{aligned}\omega_r^{(\text{circ})} &= \sqrt{\frac{g}{4R}}\left[1-\frac{\tilde{m}_{\text{F}}\,\hbar\Omega_0}{2MgR}\sqrt{1-\epsilon^2}\right]^{1/2}, \\ \omega_z^{(\text{circ})} &= 2\,|g_{\text{F}}|\,\mu_{\text{B}}\,b\sqrt{\frac{\tilde{m}_{\text{F}}}{M\hbar\Omega_0}}\left(1-\epsilon^2\right)^{3/4},\end{aligned} \tag{4.27}$$

where M is the atomic mass, g the gravitational acceleration, b the quadrupole gradient, Ω_0 the Rabi frequency at the bottom of the shell (defined by $\Omega_0 = |g_{\text{F}}|\mu_{\text{B}}B/\hbar$) and $\tilde{m}_{\text{F}}$ denote the dressed eigenstate. The dimensionless parameter ϵ compares gravity with magnetic quadrupole force, $\epsilon = Mg/2\,g_{\text{F}}\mu_{\text{B}}b\,\tilde{m}_{\text{F}}$, and R is the vertical distance below the quadrupole node.

Linear RF polarisation breaks the cylindrical symmetry of the shell, so that $\omega_x \neq \omega_y$. For a field linearly polarised along the x direction, we have

$$\begin{aligned}\omega_y^{(\text{lin})} &= \sqrt{\frac{g}{4R}}\,, \\ \omega_x^{(\text{lin})} = \omega_r^{(\text{circ})}\,, &\qquad \omega_z^{(\text{lin})} = \omega_z^{(\text{circ})}\,, \quad \text{with } B_0 \to B_0/2\,.\end{aligned} \tag{4.28}$$

For typical experimental parameters, the radial confinement is weak, with $\omega_r \sim$ 10 Hz, while the axial confinement is much stronger, ranging from about 300 Hz to above 1 kHz. This strong anisotropy makes the RF-dressed shell potential particularly well suited for realising quasi-two-dimensional Bose gases.

4.1.3 MRF-dressed double well

To realise a bilayer Bose gas, it is necessary to create a double-well potential. This can be achieved by extending the single-frequency RF dressing scheme to a multiple-radiofrequency (MRF) field. Following the procedure outlined in the previous section, the fully quantised MRF-dressed Hamiltonian is given by [96]

$$\hat{H}_{\mathrm{MRF}} = \sum_j \omega_j \, \hat{a}_j^\dagger \hat{a}_j + g_F \mu_B b \, r \hat{F}_r + g_F \mu_B \, \hat{\mathbf{F}} \cdot \hat{\mathbf{B}}_{\mathrm{MRF}} \,, \tag{4.29}$$

where $\hat{a}_j^\dagger$ and $\hat{a}_j$ are the creation and annihilation operators for photons in the j-th RF mode of frequency ω_j, and $\hat{\mathbf{B}}_{\mathrm{MRF}}$ represents the quantised multi-frequency RF field.

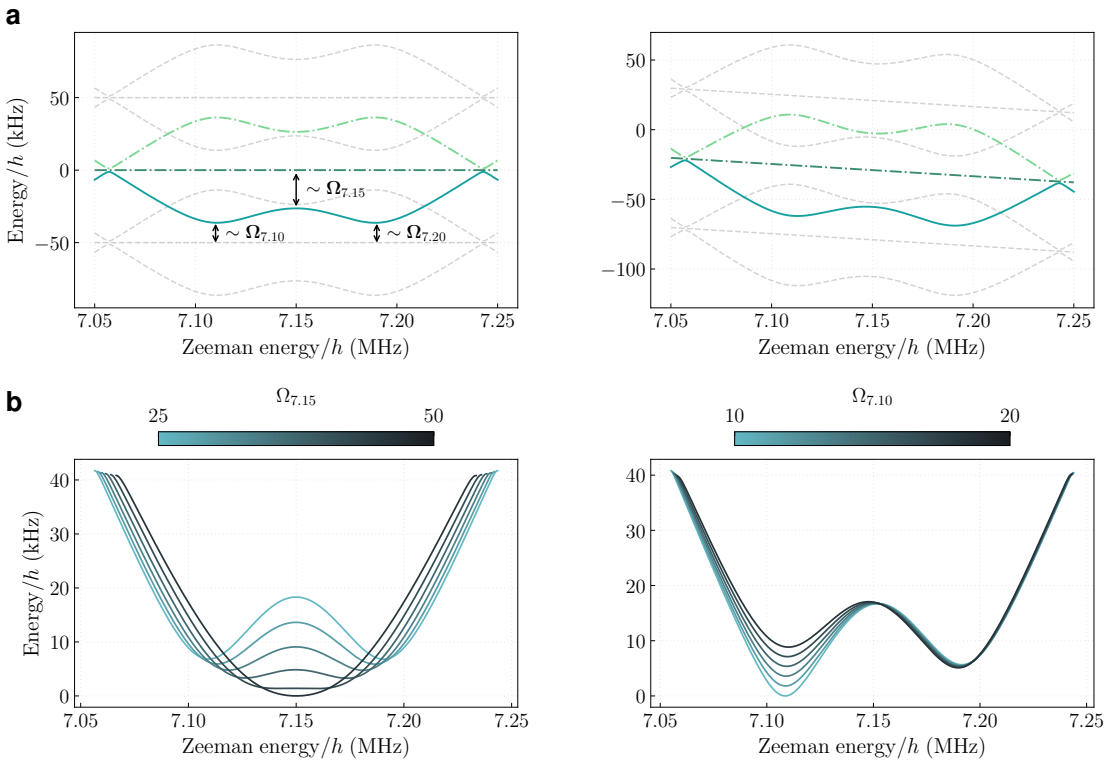

Figure 4.4: MRF-dressed double-well potential. (**a**) Numerically calculated potential for a three-component RF field $(f_1, f_2, f_3) = (7.10, 7.15, 7.20)\,\mathrm{MHz}$, shown without gravity (left) and with gravity (right). The relative depths of the potential minima and the barrier are controlled by the amplitudes of the individual RF components, i.e. their associated Rabi frequencies. The positions of the minima are shifted slightly due to coupling between different RF components. Atoms are confined in the double-well potential indicated by the solid line, while the light dashed curves show potentials belonging to other manifolds in the dressed-atom picture, separated by an energy $\hbar\omega_{\mathrm{f}}$. (**b**) Example of controlling the double-well potential by varying the amplitudes of the different frequency components of the MRF field.

Within the semi-classical approximation, the Hamiltonian reduces to

$$\hat{V}_{\mathrm{MRF}}(t) = g_F \mu_B b\, r \hat{F}_r + \frac{g_F \mu_B}{2} \sum_j \left[\left(\frac{\beta_j}{\sqrt{2}} \hat{F}_+ + \frac{\alpha_j}{\sqrt{2}} \hat{F}_- + \zeta_j \hat{F}_r \right) B_j e^{i(\omega_j t + \gamma_j)} + \mathrm{H.c.} \right], \tag{4.30}$$

where B_j is the classical amplitude of the j-th RF component, and α_j, β_j, and ζ_j are the coefficients defined in Eq. (4.16), which are determined by the polarisation of the corresponding RF field component. ω_j, γ_j and B_j are the angular frequency, relative phase and amplitude of each frequency component of the MRF dressing field, respectively. With these definitions, the multiple RF field can be written as

$$\mathbf{B}_{\mathrm{MRF}}(t) = \sum_j B_j \frac{\cos(\omega_j t)\, \mathbf{e}_x - \kappa_j \sin(\omega_j t)\, \mathbf{e}_y}{\sqrt{1+\kappa_j}} \,. \tag{4.31}$$

To render the time-dependent Hamiltonian periodic, and thereby enable the application of Floquet theory, we introduce a fundamental angular frequency ω_f and express each component as $\omega_j = n_j\, \omega_f$, where n_j is an integer. An example of numerically calculated eigenenergies is shown in Figure 4.4 for a three-component field with $(\omega_1, \omega_2, \omega_3) = 2\pi \times (7.10,\, 7.15,\, 7.20)\,\mathrm{MHz}$.

4.2 Experimental apparatus

We begin by summarising the sequence of stages used to prepare 2D bilayer Bose gases:

- **Magnetic transport:** atoms are collected in a pyramid MOT and magnetically conveyed to the ultra–high–vacuum (UHV) science cell.
- **Quadrupole trap:** atoms are confined in a quadrupole magnetic field and undergo initial forced evaporative cooling.
- **Time–orbiting potential (TOP):** a rotating bias field is applied to remove the field zero of the quadrupole, allowing further evaporation without Majorana losses.

- **Time–averaged adiabatic potential (TAAP):** a ciruclar-polarised RF dressing field is introduced in combination with the rotating bias, producing a smooth trap suitable for adiabatic loading.

- **Multiple–radiofrequency (MRF) double well:** additional dressing frequencies transform the single RF-dressed shell potential into a bilayer double–well potential, with tunable layer separation and interwell coupling.

This section provides a brief overview of the apparatus and the experimental sequences used to prepare, manipulate and image ultracold ^{87}Rb gases confined in a MRF dressed double well. Detailed descriptions of the individual experimental steps and apparatus setup can be found across earlier group theses [62, 99–102], each of which provides an in-depth account of specific aspects of the apparatus and methods.

4.2.1 Initial Cooling and magnetic transport

The experimental cycle starts with the laser cooling and trapping of ^{87}Rb atoms from a background vapour. This is performed in a magneto-optical trap (MOT) that utilises a pyramidal mirror configuration [103], allowing for a robust, single-beam-input MOT. The incident laser beam has a power of approximately 350 mW and is collimated to a 4 cm waist. It contains two frequency components (see Figure 4.6): "cooling" light, which is red-detuned by $\Delta = -22$ MHz from the $F = 2 \rightarrow F' = 3$ cycling transition of the ^{87}Rb D2 line; and "repump" light, resonant with the $F = 1 \rightarrow F' = 2$ transition, which prevents atoms from accumulating in the dark hyperfine state and pumps the atom back to the cooling cycle.

After a loading period of about 10 seconds, which accumulates approximately 2×10^9 atoms, the cloud undergoes a compressed MOT (cMOT) stage to increase its phase-space density (PSD). During this stage, the detuning of the cooling light is increased while the magnetic quadrupole gradient is ramped down, a process which reduces repulsive radiation pressure forces and facilitates sub-Doppler cooling mechanisms. Following this compression, the repump light is shuttered to allow cooling light to optically pump the atoms into the magnetically trappable $F = 1$ state.

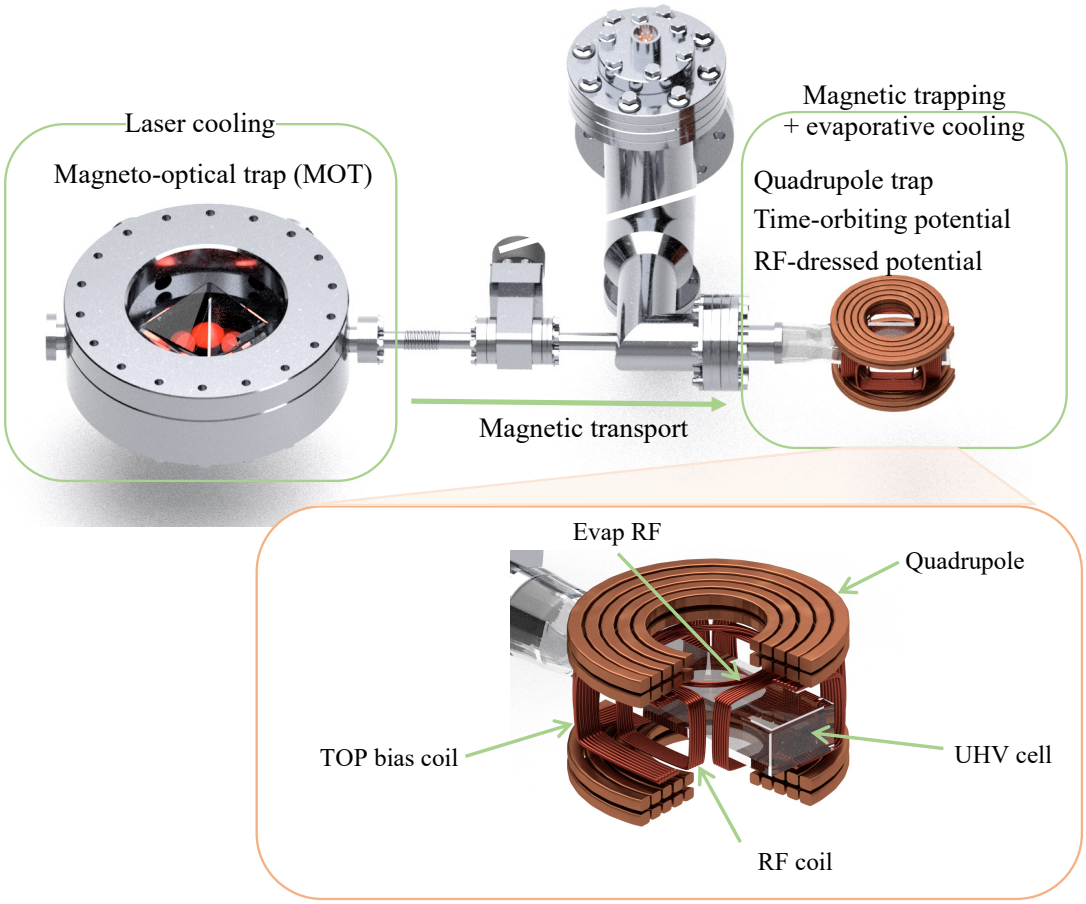

Figure 4.5: 3D model of the experimental apparatus. Initial laser cooling is performed in the pyramid MOT, after which the atoms are transported into the UHV science cell using magnetic transfer. Further evaporative cooling is then carried out, and the atoms are loaded into a double-well potential inside the science cell. The cell is surrounded by magnetic coils, as illustrated in the lower panel. The TOP bias coil and the RF dressing coils are mounted along the x and y axes. This figure is based on illustrations provided by Shinichi Sunami and originally created by Elliot Bentine.

The cold atomic cloud is then loaded into a magnetic quadrupole trap formed by a pair of coils mounted on a mechanical translation stage. This stage transports the atoms over a distance of approximately 80 cm, through a differential pumping tube, into the main ultra-high-vacuum (UHV) science cell where subsequent experiments are performed.

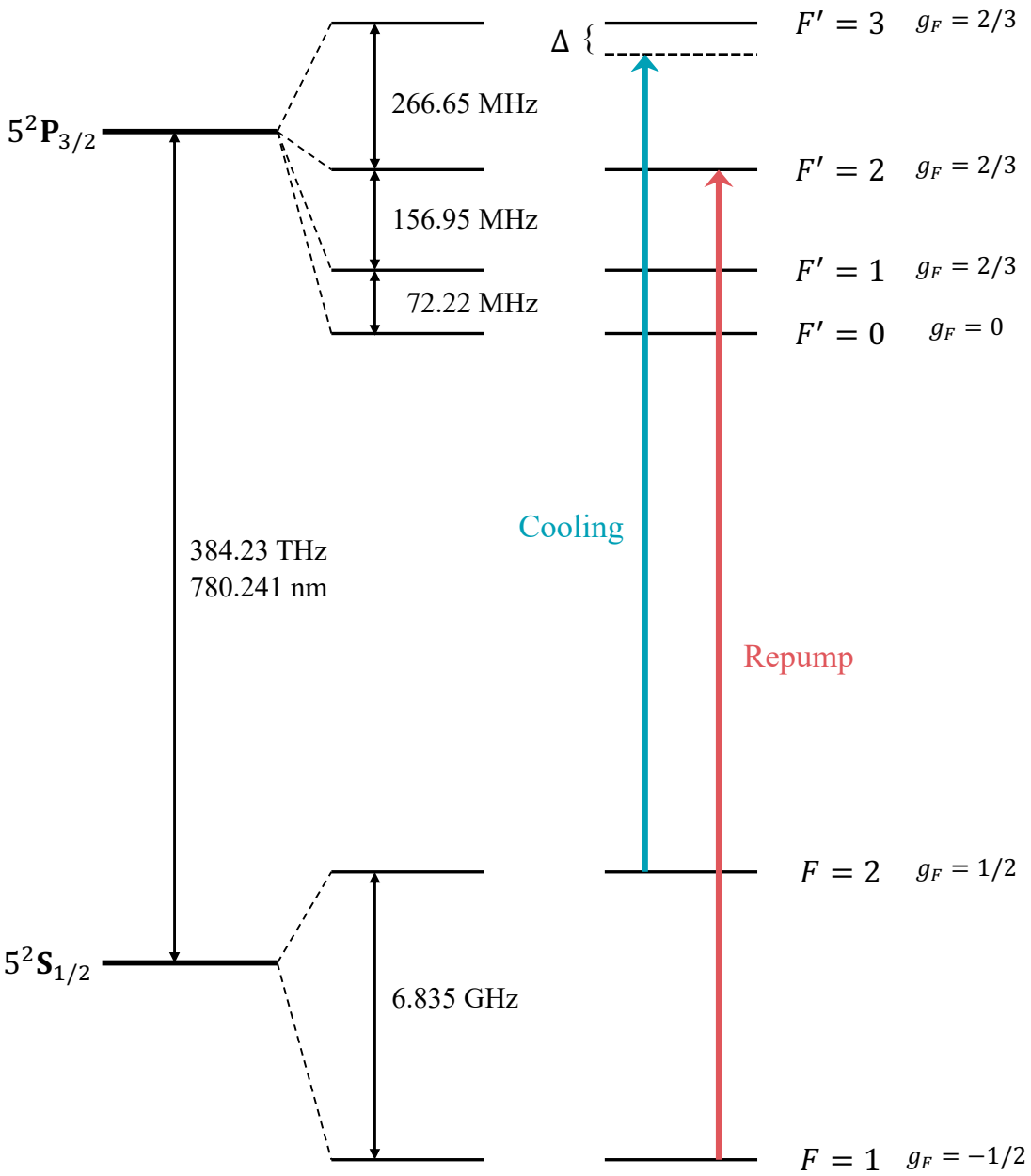

Figure 4.6: Hyperfine energy levels of ^{87}Rb D2 transition line. Figures are based on Ref. [104], with minor modifications to indicate the cooling and repump light, as well as the red detuning Δ applied during the MOT stage.

4.2.2 Magnetic trapping and evaporative cooling in the science cell

Once inside the UHV chamber, the atoms are transferred into a static magnetic quadrupole trap generated by a pair of fixed, high-current anti-Helmholtz coils. Here, forced evaporative cooling is initiated using a weak RF field, often referred to as an 'RF knife'. This RF field selectively removes the most energetic atoms from the trap. By sweeping the frequency of the RF knife, the atomic cloud is cooled to temperatures of a few tens of μK, leaving on the order of 10^7 atoms.

Further evaporative cooling in the pure quadrupole trap is hindered by Majorana spin-flip losses at the zero-field point at the trap center. To overcome this limitation, a rotating magnetic bias field at 7 kHz is superimposed on the quadrupole field, creating a time-orbiting potential (TOP) trap. The TOP trap effectively displaces the magnetic field zero away from the atomic cloud, thus suppressing Majorana losses and allowing evaporative cooling to proceed to much lower temperatures. This ultimately brings the gas to quantum degeneracy, where a BEC can be formed.

The final stage before generating the MRF potential is to load the atoms into a time-averaged adiabatic potential (TAAP) [98, 105]. This is achieved by introducing a circularly-polarised RF dressing field while the TOP bias field is still active. The atoms are then adiabatically transferred from the TOP trap into the RF-dressed potential by slowly ramping down the amplitude of the rotating bias field. A further evaporative cooling sequence is performed in the TAAP stage to produce a BEC with controlled temperature, which serves as the starting point for loading into the final MRF potential configuration.

4.2.3 MRF double-well loading and manipulation

The preparation of a bilayer 2D gas requires a carefully orchestrated sequence to load atoms into the double-well potential created by three dressing frequencies. This procedure is designed to be adiabatic to minimise heating and collective excitations.

Transition to a Linear Shell Trap

The process begins with a BEC in the circularly-polarised RF-dressing potential. As the subsequent double well potential are conducted with linearly-polarised fields, the first step is to adiabatically transition to a single-RF "shell" trap with linear polarisation. This is achieved by slowly ramping down the RF amplitude on one of the orthogonal dressing coils over ~ 1 s, leaving only the field component along the chosen axis. Simultaneously, the quadrupole current is increased to raise the axial trapping frequency (see Eq. (4.28)) and to shift the cloud vertically into the focus of the optical dipole potential (with 532 nm laser), which is used to generate a ring-shaped potential that helps to produce a nearly homogeneous cloud.

Multi-Stage double-well Splitting Procedure

The single cloud is then coherently split into a symmetric double-well potential using three RF components, typically at 7.10, 7.15, and 7.20 MHz in this thesis. This process is executed in five distinct stages to ensure stability and minimise atom loss, as detailed in Ref. [62]:

1. **Initial MRF Introduction:** The atoms are held in a deep single-well potential created by the central RF frequency component ($\Omega_{7.15}/2\pi > 100$ kHz). The other two frequencies ($\Omega_{7.10}$ and $\Omega_{7.2}$) are then suddenly switched on (< 1 ms) at a low amplitude. This configuration perturbs the trap minimally at the location of the atoms but establishes the underlying MRF structure.

2. **Avoiding Majorana-like Loss:** The central RF amplitude, $\Omega_{7.15}$, is rapidly ramped down over 7 ms to a value below the fundamental frequency separation ($\omega_f = 2\pi \times 50$ kHz). This avoids a resonance condition at $\Omega_{7.15} = \omega_f$ which would otherwise lead to significant, Majorana-like atom loss. The amplitudes of other components are ramped simultaneously to maintain the potential shape.

3. **Flat-bottom Potential:** The RF amplitudes are slowly adjusted over $\sim$ 150 ms to transform the potential into a flat-bottomed shape. This procedure

ensures that, when the cloud is subsequently split, the population is evenly distributed between the two emerging wells and sloshing within the potential is reduced.

4. **Coherent Splitting:** The central barrier is slowly raised by decreasing the amplitude $\Omega_{7.15}$ over ∼150 ms. This adiabatically splits the single cloud into two separate, decoupled clouds. The symmetry of the ramp is crucial to minimise the excitation of collective modes like sloshing or breathing.

5. **Final Potential Shaping:** The potential is further modified to achieve the final desired trap parameters. This involves increasing the axial confinement of each well to $\omega_z/2\pi > 1$ kHz while setting the radial confinement to $\omega_r/2\pi \approx$ 12 Hz, thus ensuring the clouds are in the quasi-2D regime. The barrier height is adjusted to maintain the quasi-two-dimensional condition and to control the tunnel coupling between the two clouds. A small asymmetry in the amplitudes of $\Omega_{7.10}$ and $\Omega_{7.20}$ is introduced to compensate for the differential gravitational sag, ensuring that the two wells have equal depth.

After this splitting procedure, the system is held for an equilibration time of ~ 200 ms to allow any residual excitations to damp out before subsequent experimental steps.

RF Turn-off and State Projection

At the end of the experimental sequence, the trapping potential is turned off to allow for time-of-flight (TOF) expansion before imaging. The RF fields are switched off abruptly, projecting the atoms from the dressed-state basis into the bare Zeeman substates ($|m_F = -1, 0, 1\rangle$) of the residual quadrupole field. The quadrupole field is switched off approximately 0.7 ms later to ensure that the m_F states are fully separated during TOF. During this short interval, the magnetically sensitive states ($m_F = \pm 1$) experience a force, while the $m_F = 0$ state is unaffected. For matter-wave interference measurements, we normally analyze the $m_F = 0$ population, as it undergoes a clean expansion solely under gravity. The phase of the RF fields at the moment of turn-off is precisely controlled to maximise the projection of

atoms into this desired $m_F = 0$ state, which in turn maximizes the contrast of the interference pattern. An example of an interference pattern observed after time of flight (TOF) is shown in Figure 4.7. We note a slight misalignment of the fringe position along the radial direction $(x - y)$, which may result from stray magnetic fields induced by eddy currents during the turn-off process, or from a slight angular misalignment of the quadrupole field relative to gravity [63]. At the same time, the magnetically sensitive states exhibit a stretching and compressing effect along the radial direction (magnetic lensing effect introduced by the turn off of the quadrupole field). Although this thesis focuses on the analysis of the $m_F = 0$ states, it has been proposed that the magnifying states $m_F = 1$ can also be used to faithfully capture the correlation function (with a systematic correction factor on the correlation length determined by the magnification factor), and offer an advantage for probing short-range physics due to their stretching properties [63].

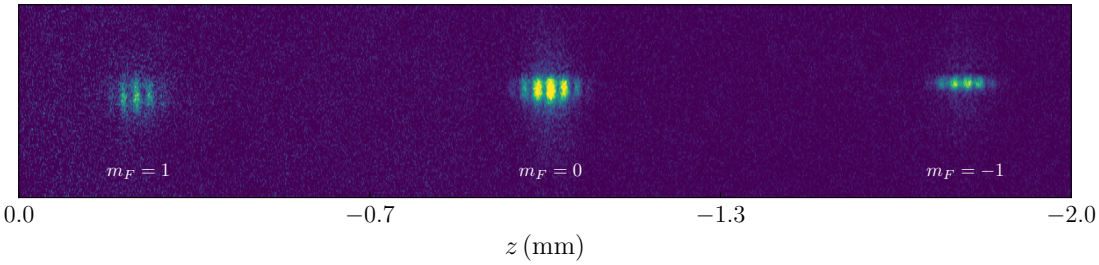

Figure 4.7: State projection and matter-wave interference pattern. Single fully repumped image of interference fringte pattern, with TOF = 16.5 ms. Atoms are projected into different Zeeman states.

4.2.4 Imaging and detection

We characterise the atomic clouds using absorption imaging, either *in situ* or after a period of TOF expansion.

Absorption Imaging Principles

The imaging technique relies on the Beer-Lambert law, which describes the attenuation of light as it passes through an absorbing medium [90]. A three-image protocol is used to construct the final atomic density profile: first, an absorption

image is taken of the atomic cloud illuminated by a probe beam (I_{a}); second, a reference image of the probe beam is taken without any atoms present (I_{r}); and finally, a background image is taken with no light to account for stray illumination and camera dark current (I_{B}).

As the atoms are magnetically trapped in the long-lived $F = 1$ hyperfine ground state, they must first be transferred to the $F = 2$ state to interact with the imaging light. This is again achieved by applying a brief pulse of repumping light, resonant with the $F = 1 \rightarrow F' = 2$ transition [101, 102]. The duration of this pulse is kept short (typically $\sim$300 μs) to minimise recoil heating from scattered photons, which could otherwise distort the measured atomic distribution [102]. Immediately following this, the 'imaging' or 'probe' beam illuminates the cloud. This beam is a pulse of circularly polarised light which is near-resonant with the closed cycling $F = 2 \rightarrow F' = 3$ transition, ensuring a strong absorption signal [62, 100]. The typical imaging intensity is several times the saturation intensity of the transition [101].

The column density of the cloud is then calculated from these three images. The optical density (OD) is determined using a formula that accounts for the saturation of the atomic transition at high light intensities [106]:

$$OD(x_p, y_p) = \ln\left(\frac{I_{\mathrm{a}} - I_{\mathrm{B}}}{I_{\mathrm{r}} - I_{\mathrm{B}}}\right) + \frac{I_{\mathrm{r}} - I_{\mathrm{a}}}{I_{\mathrm{sat}}}$$

where (x_p, y_p) are the pixel coordinates and $I_{sat} = 1.67$ mW/cm^2 is the saturation intensity for the imaging transition [104]. The number of atoms per pixel is found by dividing the optical density by the theoretical absorption cross-section, $N(x_p, y_p) = OD(x_p, y_p)/\sigma_{\mathrm{cross}}$. This calculation is then precisely calibrated by comparing the experimentally observed onset of Bose-Einstein condensation in a 3D harmonic trap with the established theoretical prediction for the critical point. This calibration is performed by measuring the condensate fraction as a function of temperature and fitting the data to obtain a single scaling factor for the total atom number; details are provided in Ref. [62].

Horizontal Imaging

The horizontal imaging system is oriented perpendicular to the direction of gravity. It is the primary method for observing matter-wave interference patterns, as the expanding clouds fall within its focal plane. The optical setup consists of a two-lens telescope with an objective of $f = 75$ mm and an eyepiece of $f = 200$ mm, providing a magnification of 2.71. The final image-plane pixel size is $l_p = 1.67$ μm, and the measured optical resolution (characterised by the point-spread function) is $\sigma_{\mathrm{PSF}} = 2.1$ μm.

Vertical Imaging

The vertical imaging system is aligned parallel to gravity and is used to measure the *in situ* 2D density distribution of the atomic clouds. It features a high numerical aperture (NA = 0.27) custom objective lens with $f = 37.6$ mm, an $f = 500$ mm eyepiece lens, and an electron-multiplying CCD (EMCCD) camera, providing an image with an effective pixel size of $l_p = 1$ μm and a point-spread function of $\sigma_{\mathrm{PSF}} = 0.5$ μm.

Selective Repumping

A key challenge in studying fluctuating 2D systems is that standard absorption imaging integrates the density along the line of sight. This averaging process obscures the local phase and density fluctuations that are central to the physics of interest. To overcome this, we employ a selective repumping technique, as detailed in Refs. [62, 102]. This method uses a Digital Micromirror Device (DMD) to shape the repumping laser beam. The DMD consists of an array of individually controllable micromirrors, projects an arbitrary light pattern onto the atoms. For our purposes, the repumping light (resonant with the $F = 1 \rightarrow F' = 2$ transition) is shaped into a thin sheet of controllable thickness, L_y, oriented perpendicular to the horizontal imaging axis.

This light sheet selectively transfers atoms within a thin slice of the cloud from the magnetically trapped $F = 1$ state to the $F = 2$ state, making them visible to

the imaging beam. By imaging only this repumped slice, we avoid integrating over the fluctuations along the line-of-sight, thereby revealing the local phase profile of the interference pattern with high contrast. A typical slice thickness of $L_y = \sim 4\ \mu$m is used to locally resolve phase variations, provided that the correlation length is larger than the slice thickness. The programmable nature of the DMD allows the position and thickness of this slice to be arbitrarily chosen, providing a powerful tool for probing the 2D gas [23, 107].

5

Coupling-induced Universal Dynamics in Bilayer 2D Bose Gases

Contents

Ordering dynamics far from equilibrium is among the most intriguing areas in many-body physics, with implications extending from early-universe cosmology to condensed matter and particle physics [108–112]. Systems driven far from equilibrium have been shown to exhibit scale invariance and self-similar behavior as they enter universal scaling regimes defined by specific scaling laws and exponents [15, 113–115]. Such universal dynamics have been reported across various systems spanning spinor Bose condensates [16, 17, 115–119], binary mixtures [120–122], spin-orbit-coupled condensates [123], exciton-polariton condensates [124–126], Rydberg atom arrays [127] and vortex-free scalar Bose gases [128]. A particularly interesting

form of universal dynamics is coarsening, emerging after a quench from disorder to order when the domain size grows beyond the relevant microscopic scale. It is well established that coarsening can follow a spontaneous symmetry breaking transition [15–17], or arise from topological transition, as in the 2D XY model where vortex and antivortex annihilation drive ordering [18–20]. In both cases, the late-time growth typically follows power laws set by dimensionality, symmetry, conservation laws, and topological defect types, rather than by microscopic details [15, 115], underscoring universality out of equilibrium. However, whether coarsening dynamics can arise following a quench that explicitly breaks the original symmetry remains poorly understood.

The coupled 2D XY model is a paradigmatic platform for such an investigation, with broad relevance including high temperature superconductivity [30, 70, 129–131] and high energy physics [87, 132, 133]. In equilibrium, the relative mode of the system exhibits a normal to coupling-induced bilayer superfluid (BSF) transition driven by vortex pair-binding, with a critical point that has a strong dependence on the interlayer coherent coupling strength J_c, which explicitly breaks the $U(1)$ symmetry [12, 13, 30–32]. Therefore, the recent realization of highly tunable coupled bilayer superfluids with ultracold atoms [14] offers a unique opportunity to extend the experimental probe of nonequilibrium dynamics: the precise and rapid control of the interlayer coupling strength in such a setup enables sudden coupling quenches. In the absence of topological defects, theory predicts that the relative phase following a coupling quench undergoes universal rephasing connected to sine-Gordon (SG) dynamics in both 1D and 2D superfluids [11, 134–138]. In contrast, the coupled 2D XY model hosts vortices and antivortices in the relative mode whose presence qualitatively modify relaxation and can enable a transition from disorder to order, leaving open whether universal dynamics persist and, if so, what form they take.

In this chapter, we report experimental observations of universal dynamics following a symmetry breaking coupling quench, appearing as coarsening via vortex and antivortex annihilation in the relative phase of a coherently coupled 2D bilayer. To this end, we realize a bilayer 2D quantum system consisting of two nearly

homogeneous layers of 2D Bose gases with precisely and dynamically controlled interlayer coupling. This allows us to quench the system from a disordered phase to an ordered phase by a sudden change of the coupling, after which the system relaxes toward a phase-locked, coherent state in the relative phase mode. We probe the resulting relaxation dynamics using matter-wave interferometry, which provides direct access to local phase fluctuations in the system. From these, we measure the two-point correlation function and the vortex density, which are key observables for characterizing the scale-invariant universal dynamics. The typical size of the phase coherent domain, extracted from the correlation function, exhibits power-law scaling in direct agreement with the scaling of the vortex density. By varying the initial phase-space density (PSD), we verify the universality of phase-ordering dynamics and extract the corresponding dynamic critical exponent $z = 1.73(7)$. We perform extensive numerical simulations based on classical-field approximation to corroborate our measurements. The measured value of the critical exponent indicates a diffusion-like coarsening, consistent with theoretical predictions for scaling dynamics in quenched 2D Bose gases [20], and close to the (near-) Gaussian non-thermal fixed point (NTFP) predicted in both quenched 2D Bose gases and the 2D SG model [19, 139].

5.1 Preparation and detection of non-equilibrium coupled 2D systems

We begin with an ultracold condensate Bose gas of ^{87}Rb atoms in the $F = 1$ hyperfine state, with a total atom number ranging from 1.8×10^4 to 2.5×10^4 at a temperature of $T \approx 27\,\mathrm{nK}$ (see Figure 5.1). The atoms are adiabatically loaded into a decoupled double-well quasi-two-dimensional (quasi-2D) potential, as described in detail in Section 4.2.3 and Refs. [23, 96, 140, 141]. The potential is engineered using three radio-frequency (RF) fields with frequencies $(f_1, f_2, f_3) = (7.10, 7.15, 7.20)$ MHz, combined with a static quadrupole magnetic field $\boldsymbol{B}(\boldsymbol{r}) = b(x\boldsymbol{e}_x + y\boldsymbol{e}_y - 2z\boldsymbol{e}_z)$, where the field gradient is $b = 147\,\mathrm{G\,cm^{-1}}$. In addition to the RF-dressed potential, an optical dipole potential is created by a 532 nm ring-shaped laser beam propagating

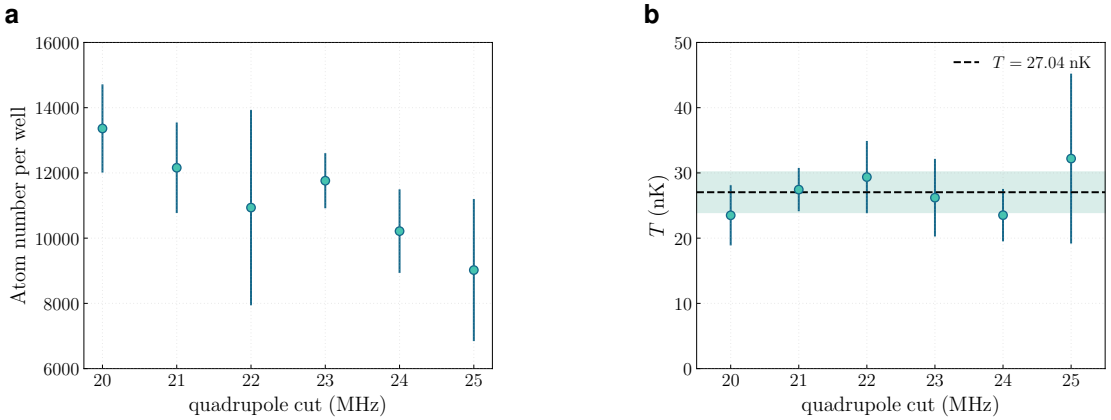

Figure 5.1: Atom number and thermometry. (**a**) Atom number per well and (**b**) temperature, as functions of the final evaporation frequency in the quadrupole trap (labeled as the "quadrupole cut"). The temperature is determined by loading the atoms into a purely harmonic trap (without the optical dipole potential) and performing bimodal fits after time of flight (TOF), as detailed in Ref. [62]. The cloud temperature is set by the final evaporation frequency in the TAAP stage, which is fixed in order to maintain a constant temperature. The cloud is fully repumped before measuring the atom number and temperature.

vertically, shaped via direct imaging of a digital micromirror device (DMD) onto the atomic plane. The dipole potential thus act as a hard wall which make the cloud near-uniform. Equal population in the two wells is ensured by maximizing the measured contrast of the matter-wave interference pattern, as described in Ref. [140].

The atomic clouds are held in the decoupled double-well for 250 ms to allow the system to equilibrate. The barrier height is then rapidly lowered over a duration of 15 ms to $E_b/h = 1.94\,\mathrm{kHz}$, constituting a non-adiabatic quench for the radial dynamics, which have a characteristic timescale of $2\pi/\omega_r = 86\,\mathrm{ms}$. During the quench, the tunnel coupling strength increases exponentially from less than 10^{-3} (which we refer to as zero coupling) to 34 Hz, as shown in Figure 5.2, while the axial trap frequencies are reduced from $\omega_z/2\pi = 1.6\,\mathrm{kHz}$ to 1.2 kHz. Throughout the experiment, the quasi-2D conditions $\hbar\omega_z > k_B T$ and $\hbar\omega_z > \mu$ are satisfied, where $\hbar$ is the reduced Planck constant, k_B the Boltzmann constant, and μ is the chemical potential. The characteristic dimensionless 2D interaction strength is $\tilde{g} = \sqrt{8\pi}a_s/\ell_0 \sim 0.08$, where a_s is the 3D scattering length and $\ell_0 = \sqrt{\hbar/(m\omega_z)}$ is the harmonic oscillator length along z for an atom of mass m. The coupling

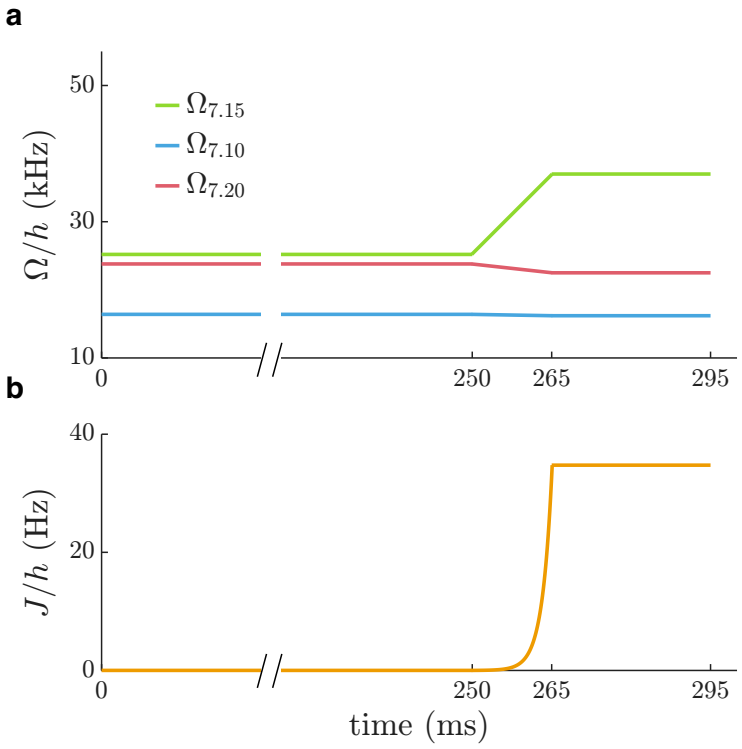

Figure 5.2: Coupling quench procedure. (**a**) Time evolution of the RF amplitudes during the coupling quench, expressed as Rabi frequencies $\Omega_{f_i} = g_F \mu_B B_i / 2\hbar$ for components $i = 1, 2, 3$, where B_i is the RF magnetic field amplitude at frequency f_i, g_F is the Landé g-factor, and μ_B is the Bohr magneton. Atoms are initially confined in a decoupled multiple-RF-dressed two-dimensional (2D) double-well potential and held for an additional 250 ms to allow thermal equilibration. The quench is initiated by rapidly increasing the amplitude of $\Omega_{7.15}$ for 15 ms, thereby modifying both the barrier height and the separation between the wells. The amplitude of $\Omega_{7.20}$ is dynamically adjusted during the quench to maintain a balanced double-well configuration. (**b**) The inter-well coupling strength exhibits exponential growth during the quench, calculated from two-mode model [77].

quench drives the system far from equilibrium, where the final coupling strength corresponds to the BSF phase, such that the system dynamically phase-locks and relaxes to an ordered state. To study the relaxation dynamics, the gases are then held in the coupled double-well for a variable duration. In this configuration, we measure a lifetime of 2.2 s (see Figure 5.3), which is sufficiently long to investigate the coarsening dynamics presented in the following sections.

Following the evolution, the MRF-dressed and optical potentials are turned off

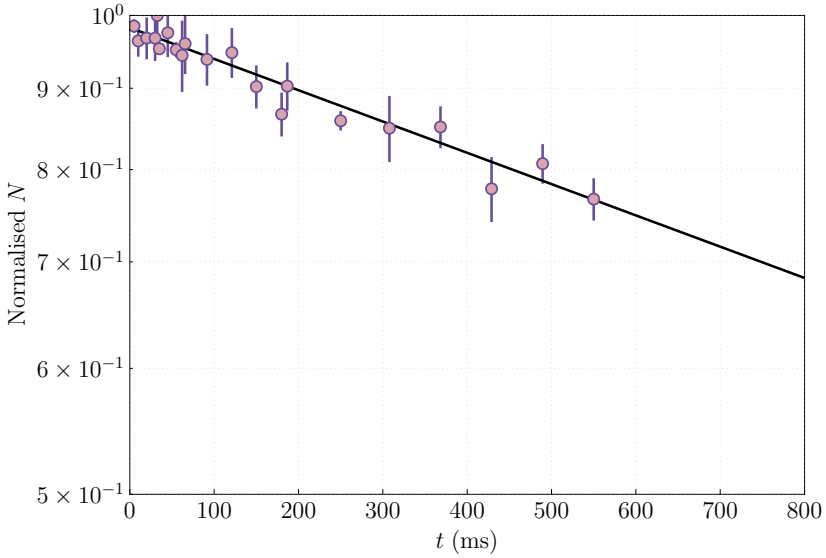

Figure 5.3: Lifetime measurement after the coupling quench. Atom number in the double well following the coupling quench. The atom number is normalised to a maximum value of 1. The y axis is plotted on a logarithmic scale, and the black solid line is an exponential fit yielding a lifetime of 2.2 s.

to release the clouds into a 16.5 ms time-of-flight (TOF), allowing the formation of a matter-wave interference pattern. The optical potential is turned off 3 ms before release to avoid the influence during expansion. To image this pattern, atoms are selectively pumped from the $F = 1$ to the $F = 2$ hyperfine state using a repumping light sheet propagating vertically (along the z-axis), with a thickness of $L_z = 4\,\mu\text{m}$ and a vertical extent much larger than the size of the atomic cloud. The interference pattern is then imaged using light resonant with the $F = 2$ state. We ensure the repumping light intersects the center of the cloud by translating the light sheet along the imaging axis and locating the position that maximizes the total absorption signal. We repeat the measurements at least 40 times at each atom number and hold time t, to obtain sufficient statistics for the analysis we describe below.

5.1.1 Image analysis for relative phase detection

The matter-wave interference pattern we observe is of the form [35]

$$\rho_x(z) = \rho_0 \exp\left(-z^2/2\sigma^2\right)\left[1 + c_0 \cos(kz + \theta(x))\right], \tag{5.1}$$

along z direction at each location x. The phase $\theta(x)$ encodes a specific realization of the fluctuations of the *in situ* local relative phase. Rather than employing the fitting method to extract the phase [140, 142], we use the discrete Fourier transform (DFT), which offers a fast and precise approach for extracting phases from the measured interference patterns (Figure 5.4). We extract the phase by computing the FFT spectrum averaged over all images and identifying the relevant spatial frequency k_0 corresponding to the matter-wave interference pattern.

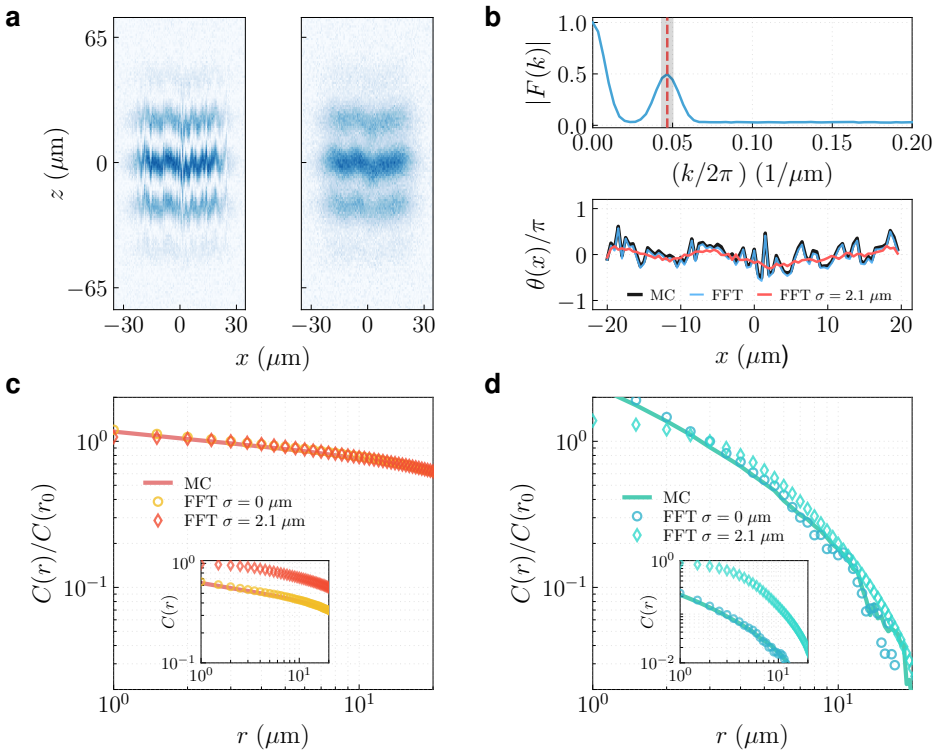

Figure 5.4: Relative-phase extraction. (**a**) Simulated interference pattern after TOF with phases generated from Monte Carlo (MC) simulation. The left displays simulated distribution and the right incorporates the effects of white noise and finite experimental resolution. (**b**) The top panel shows typical normalized Fourier spectrum of the interference pattern $|F(k)|$ along z axis, the position of peak index k_0 is marked by the red dashed line and the shaded region indicates the vicinity of the peak index, $k_0 \pm 1$. In the bottom panel, extracted relative phase $\theta(x)$ is shown alongside the input MC relative phase. (**c,d**) Phase correlation function obtained from simulated interference pattern (including shot noise of the imaging apparatus), with and without the effect of finite imaging resolution σ. We rescale the correlation function with its value at fixed distance $C(r_0 = 3\,\mu\text{m})$, to visually demonstrate that finite image resolution does not affect the long-distance behavior which is used for the quantitative analysis in this paper. Inset shows the unscaled $C(r)$. We show correlation functions obtained from the simulated interference images at different PSDs, exhibiting power-law and exponential decay for **c** and **d**, respectively.

For the analysis of the correlation function, phases are obtained by averaging several points in the vicinity of k_0, which preserves the phase difference while reducing the impact of noise. In the experiment, we calculate the averaged phase two-point correlation function $C(x, x') = \mathrm{Re}[\langle e^{i[\theta(x)-\theta(x')]}\rangle]$ from the ensemble of at least 40 images. The averaging is performed over the set of images and different positions x such that x and $x - \overline{x}$ are within the central $\sim 30\,\mu\mathrm{m}$ of the density distribution of the cloud. We then calculate $C(r)$ by averaging $C(x, x')$ over points with the same spatial separations $r = x - x'$, and fit them to both exponential and algebraic models (Figure 5.5b).

Vortices are identified in interference images acquired along the y-direction, following the procedure detailed in [23]. We detect vortices by searching for abrupt phase jumps within a two-pixel distance ($3.4\,\mu\mathrm{m}$), defined by a phase difference in the range $\pi/3 < \delta\theta < 2\pi/3$ (Figure 5.5c). The vortex density $n_v(x)$ is determined by dividing the probability of finding a vortex in each image column by the effective detection area of a single pixel column $\ell_p L_y = 6.7\,\mu\mathrm{m}^2$, where $\ell_p = 1.67\,\mu\mathrm{m}$ is the pixel size in the image plane.

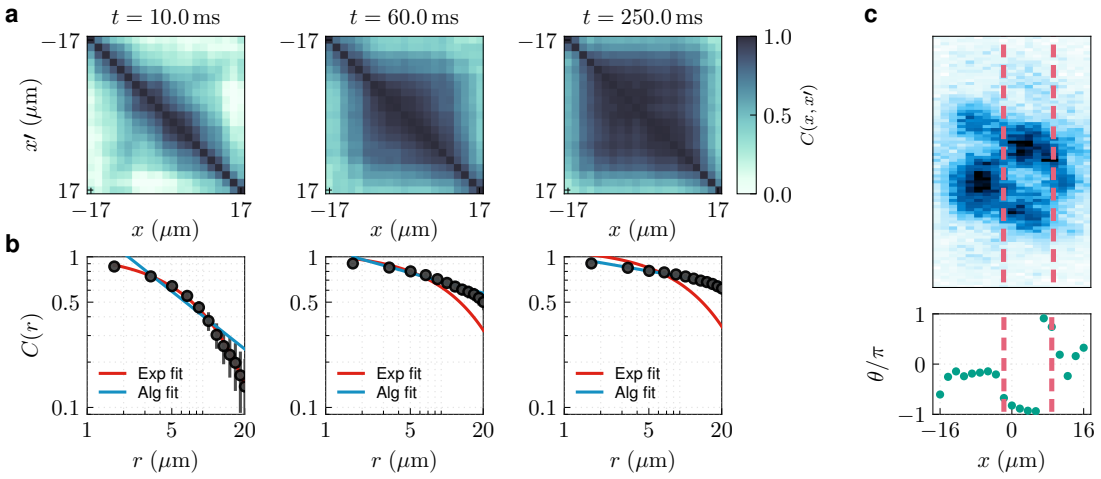

Figure 5.5: Phase correlation function analysis and vortex detection. (**a**) Averaged two point correlation $C(x, x')$ at different hold times; (**b**) Spatially averaged correlation function $C(r)$ with $r = x - x'$, fitted with exponential and power-law (algebraic) models. (**c**) Vortices are identified by abrupt phase jumps, indicated by red dashed lines. The bottom panel shows the phase profile extracted from the interference pattern.

5.2 Numerical simulations method

We simulate the many-body dynamics of bilayer 2D Bose gases using classical-field simulations within the truncated Wigner approximation [21, 22]. For numerical simulations, we discretize real space on a 2D square lattice and represent the continuous Hamiltonian using the discrete Hamiltonian, as described in Section 3.2. We choose the simulation parameters such as the interaction, phase-space density, and coupling strength according to the experiments. We consider a lattice system of 152×152 sites with a discretization length of $l = 0.3\,\mu$m. We note that for the continuum limit, l is chosen to be smaller than or comparable to the healing length and the thermal de Broglie wavelength $\lambda = h/\sqrt{2\pi m k_{\mathrm{B}} T}$, where T is the temperature, k_{B} the Boltzmann constant, and h is the Planck constant [44]. The initial axial trapping frequency is $\omega_z/(2\pi) = 1.6\,$kHz, resulting in $\tilde{g} = 0.098$ for ^{87}Rb atoms. The coupling strength between the two clouds is initially set to zero.

In the classical-field approximation, we replace the operators $\hat{\psi}$ by complex numbers ψ both in the Hamiltonian and in the equations of motion. We sample the initial states of the decoupled system within a grand-canonical ensemble having temperature T and chemical potential μ via a classical Metropolis algorithm [21, 22, 58]. We set $T = 28\,$nK and adjust μ such that the phase-space density $\mathcal{D} = n\lambda^2$ varies in the range between 7.8 and 9.3, where n is the average 2D density. Finally, each state is propagated using the equations of motion (Eq (3.40)) introduced in Section 3.3. In the time evolution, we ramp up J from 0 to 34 Hz over the duration of 15 ms. This also includes a shift of the axial trap frequency from $\omega_z/(2\pi) = 1.6\,$kHz to 1.2 kHz, resulting in the final interaction $\tilde{g} = 0.085$. We examine the resulting dynamics of the system phases $\phi_1(\mathbf{r}, t)$ and $\phi_2(\mathbf{r}, t)$ of the two clouds, which directly gives access to the relative-phase mode via $\theta(\mathbf{r}, t) = \phi_1(\mathbf{r}, t) - \phi_2(\mathbf{r}, t)$. From the phase evolution of the relative mode we compute the two-point correlation function and vortex density, following the same method as in the experiments. Finally, for each value of the phase-space density, we average the correlation function and the vortex density over the initial ensemble.

5.3 Effective low energy description

Here we show that the relative sector of the coupled bilayer system are closely related to the sine–Gordon model. We consider a many-body system consisting of a quasi-2D ultracold gas of ^{87}Rb confined in a double-well potential. The resulting tunnel-coupled 2D system is described by the Hamiltonian

$$\begin{aligned} H = \int d^2r \sum_{j=1}^{2} \Big[\frac{\hbar^2}{2m} \nabla\psi_j^\dagger \cdot \nabla\psi_j + \frac{g}{2}\psi_j^\dagger\psi_j^\dagger\psi_j\psi_j \\ + (V-\mu)\,\psi_j^\dagger\psi_j \Big] - \hbar J \int d^2r \left(\psi_1^\dagger\psi_2 + \psi_2^\dagger\psi_1\right), \end{aligned} \tag{5.2}$$

where ψ_j and $\psi_j^\dagger$ are bosonic annihilation and creation operators in jth layer, respectively, satisfying the commutation relations $[\psi_j(\boldsymbol{r}), \psi_{j'}^\dagger(\boldsymbol{r}')] = \delta_{jj'}\delta^{(2)}(\boldsymbol{r}-\boldsymbol{r}')$. $g = \tilde{g}\hbar^2/m$ is the quasi-2D interaction strength, V is the trapping potential, μ is the chemical potential, and J is the interlayer tunnel coupling strength. ∇ is the 2D gradient in the (x, y) plane. We then adopt density-phase representation

$$\psi_j(\boldsymbol{r}) = \exp\left[i\theta_j(\boldsymbol{r})\right]\sqrt{n_{\mathrm{2D}} + \delta\rho_j(\boldsymbol{r})}, \tag{5.3}$$

by assuming a box trapping potential $V = 0$. Phase $\theta_j(\boldsymbol{r})$ and density fluctuations $\delta\rho_j(\boldsymbol{r})$ obey the commutation relations $[\theta_j(\boldsymbol{r}), \delta\rho_{j'}(\boldsymbol{r}')] = -i\,\delta_{jj'}\delta^{(2)}(\boldsymbol{r}-\boldsymbol{r}')$.

For a system with equal atomic populations in each layer, the relative (anti-symmetric) mode in the low-temperature regime is effectively described by a Hamiltonian of the form:

$$H_{\mathrm{rel}} = H_{\mathrm{XY}} + H_{\mathrm{J}}, \tag{5.4a}$$

$$H_{\mathrm{XY}} = \int d^2r\, \frac{\hbar^2}{2m}\left[\frac{(\nabla\delta\rho_a)^2}{2n_{\mathrm{2D}}} + 2\tilde{g}\delta\rho_a^2 + \frac{n_{\mathrm{2D}}}{2}(\nabla\theta)^2\right], \tag{5.4b}$$

$$H_{\mathrm{J}} = -\int d^2r\, n_{\mathrm{2D}}\hbar J\left[2\cos\theta - \frac{\delta\rho_a^2}{n_{\mathrm{2D}}^2}\cos\theta + \frac{\delta\rho_s}{n_{\mathrm{2D}}}\cos\theta\right]. \tag{5.4c}$$

Here we apply canonical transformation to express the system in terms of symmetric and antisymmetric degrees of freedom, and expand the Hamiltonian to

quadratic order. $\theta(\boldsymbol{r}) = \phi_1(\boldsymbol{r}) - \phi_2(\boldsymbol{r})$ is the relative (antisymmetric) phase, and the common (symmetric) phase is defined as $\varphi(\boldsymbol{r}) = (\phi_1(\boldsymbol{r}) + \phi_2(\boldsymbol{r}))/2$. The density fluctuations in symmetric (subscript s) and antisymmetric (subscript a) are defined as $\delta\rho_s(\boldsymbol{r}) = \delta\rho_1(\boldsymbol{r}) + \delta\rho_2(\boldsymbol{r})$, $\delta\rho_a(\boldsymbol{r}) = (\delta\rho_1(\boldsymbol{r}) - \delta\rho_2(\boldsymbol{r}))/2$. Notably, the relative phase is coupled to the symmetric degrees of freedom through the tunnel coupling, which can serve as a weak dissipative bath for the relative phase [11, 143].

In the regime of a quasi-condensate with strongly suppressed density fluctuations, the Hamiltonian for the relative mode reduces to the sine-Gordon form,

$$H_{\mathrm{SG}} = \int d^2r \, \frac{\hbar^2}{2m} \left[\frac{n_{2\mathrm{D}}}{2} (\nabla\theta)^2 + 2\tilde{g}\delta\rho_a^2 \right] - 2n_{2\mathrm{D}}\hbar J \cos\theta. \tag{5.5}$$

5.4 Observation of universal phase ordering dynamics

We perform experiments with two-dimensional (2D) Bose gases prepared in the normal (disordered) phase, where free vortices are present, within a decoupled double-well potential, and then suddenly quench the tunnel coupling between the wells. For two tunnel-coupled 2D Bose gases labelled $i = 1, 2$ and each represented by bosonic field $\Psi_i(\boldsymbol{r})$, it is convenient to decompose the system into symmetric (common) and anti-symmetric (relative) degrees of freedom. In the absence of interlayer coupling, the relative and common phases undergo the well-known Berezinskii–Kosterlitz–Thouless (BKT) transition. With finite coupling, phase locking becomes energetically favorable, establishing coherence between the two layers and driving the system into the BSF phase [13, 14], as illustrated in Figure 5.6. The coupling term explicitly breaks the $U(1)$ symmetry of the relative phase, resulting in a distinct behavior from the conventional BKT transition. However, the transition in the relative phase is still expected to arise from the binding of vortex–antivortex pairs [68–70], as discussed previously for the equilibrium coupled bilayer system (Sections 2.2 and 3.2.2).

Following the quench, the interlayer coupling begins to lock the phases of the two layers. This corresponds to the emergence of a preferred relative phase that

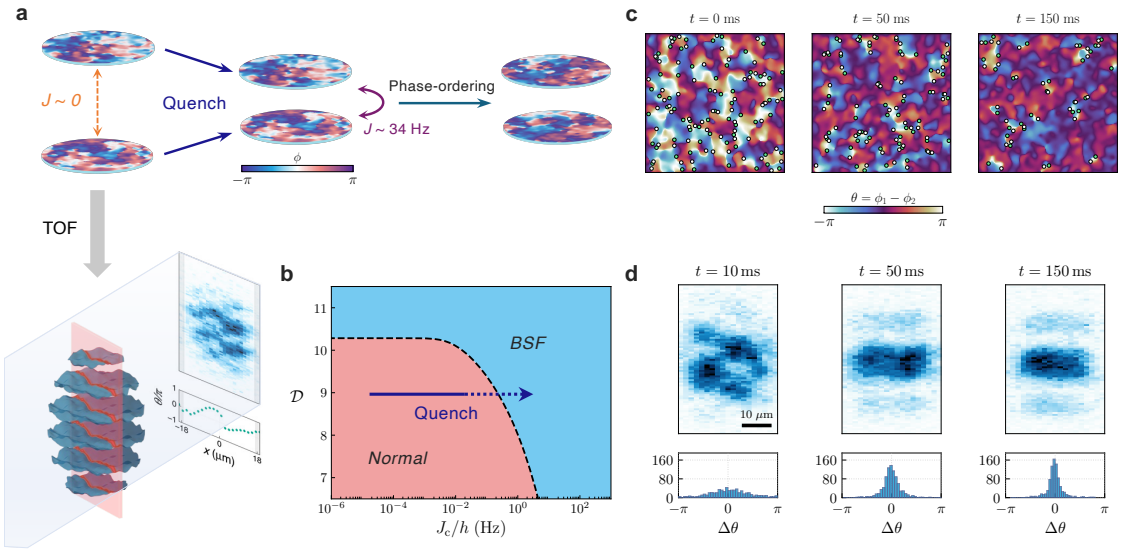

Figure 5.6: Interlayer coupling quench in bilayer 2D quantum gases. (**a**) (Top) We quench the interlayer coupling J from nearly zero to 34 Hz, driving an initially decoupled bilayer with free vortices toward a phase-locked, coherent state. (Bottom) Relaxation dynamics are monitored by matter-wave interferometry, with local fluctuations of relative phase captured by optically pumping a thin slice (red sheet) before absorption imaging. A representative pre-quench interference image is shown, with the extracted relative phase profile plotted below. (**b**) The equilibrium phase diagram for the relative-phase mode, as a function of the interlayer coupling J_c and phase-space density $\mathcal{D}$, obtained via renormalisation-group analysis [13, 14] (also see Section 2.3.7); the quench induced by the sudden increase in J drives the system to a bilayer superfluid (BSF). The dashed line indicates the critical points. (**c**) Numerical simulation of the quench dynamics shows relaxation toward a nearly phase-locked state. Vortices (open circles) and antivortices (filled circles) decay over time through dynamical pairing and annihilation. The phase-locked domains (dark blue to dark red) grow progressively. (**d**) (Top) Typical single-shot interference image at different hold times after the quench show the evolution from an initial state containing vortices (left), identifiable by sharp phase discontinuities (see Figure 5.5), to a phase-coherent state (right). (Bottom) Histogram of phase difference $\Delta\theta = \theta(x) - \theta(x')$ at fixed distance $|x - x'| = 5\,\mu\text{m}$, showing suppression of phase fluctuations over time, obtained from 40 experimental runs.

minimizes the $-\cos(\theta)$ term in the effective Hamiltonian (see Eq. (5.4)), reflecting the breaking of $U(1)$ symmetry with minima at $\theta = 2\pi n$, $n \in \mathbb{Z}$. In Figure 5.7, we show the distribution of the relative phase extracted from the matter-wave interference pattern at various hold times. The distribution is nearly uniform shortly after the quench, consistent with the initial decoupled state possessing $U(1)$ symmetry. The onset of phase locking is evidenced by the gradual development of a peak at wrapped phase $\theta = 0$ over time. To quantify the phase locking, we plot the

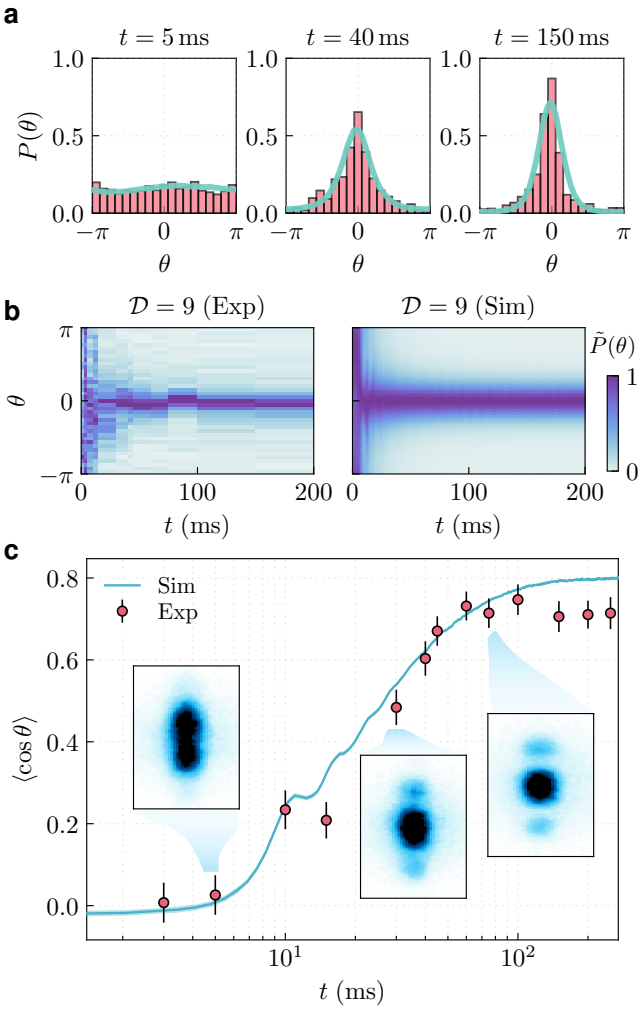

Figure 5.7: Dynamical phase-locking transition. (**a**) Probability density distribution of the relative phase, $P(\theta)$, at selected evolution times after the quench, obtained from experiments (histograms) and simulations (solid lines). (**b**) Time evolution of the normalized phase distribution, $\tilde{P}(\theta) = P(\theta)/\max(P(\theta))$, from experiments (left panel) and simulation (right panel), illustrating the emergence of phase locking. Each column represents a histogram of the phases (panel **a**) by colors. (**c**) Relative-phase order parameter $\langle\cos\theta\rangle$ plotted on a linear-log scale. Experimental data (dots) have error bars obtained via bootstrapping, while simulation results are shown as a solid line (mean) with a shaded region indicating uncertainty. The simulation exhibits a small, damped oscillation at a frequency on the order of the Josephson plasma frequency. Averaged interference patterns from over 40 experimental runs are shown for selected evolution times t (insets).

evolution of the phase order parameter $\langle\cos\theta\rangle$, which is indicative of phase-locking strength and interference contrast [11, 134].

The averaged experimental interference fringes exhibit a clear increase in interference contrast over time, and the resulting time evolution of $\langle\cos\theta\rangle$ is in good

agreement with numerical simulations that account for finite imaging resolution. The saturation of $\langle \cos\theta \rangle$ at slightly lower values than the numerical simulation arises from finite thermal populations that become more pronounced at longer evolution times.

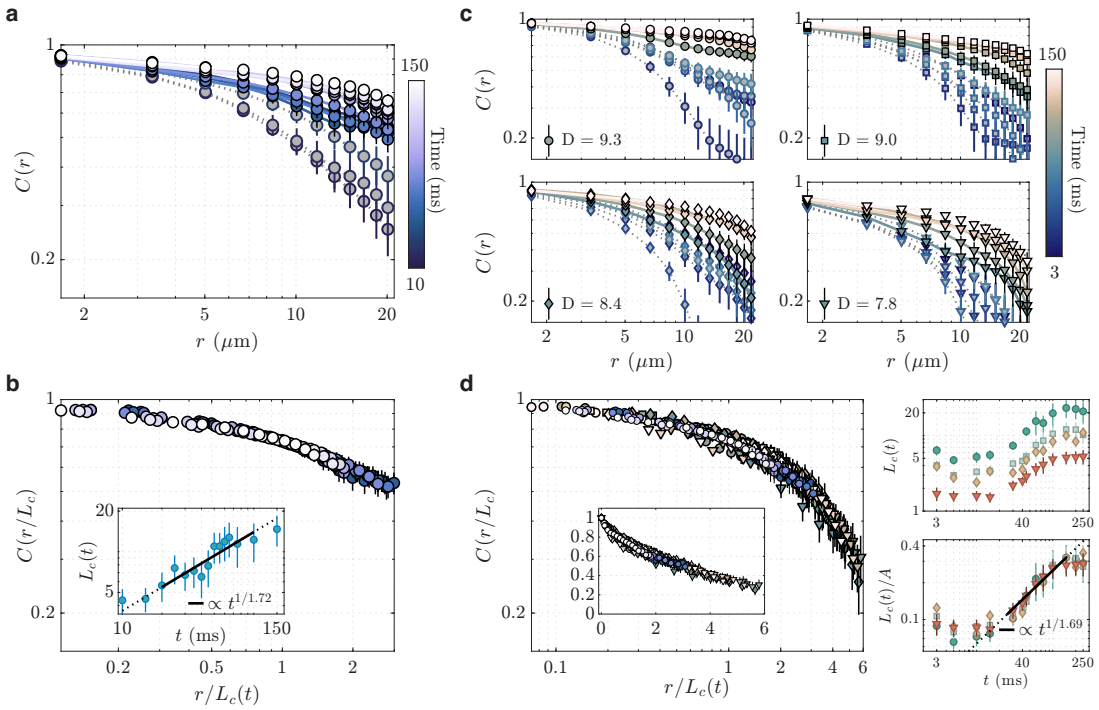

Figure 5.8: Build-up of phase coherence and the universal dynamics. (**a**) Phase correlation function $C(r,t)$ at $\mathcal{D} = 9.2$ measured at various hold times following the quench. The data are averaged over 50 independent realizations, with error bars indicating the standard error of the mean. Data corresponding to times that do not exhibit self-similar behavior are shown as gray markers connected by dotted lines. The remaining data, which display self-similar scaling, are represented by colored markers (with a gradient indicating time progression) connected by solid lines. (**b**) Correlation functions at different times collapse onto a single universal curve, shown on a log–log scale. Inset: Power-law growth of the correlation length $L_c(t)$ on a log–log plot. The black line represents a fit to the form $L_c(t) = A\, t^{1/z_{\mathrm{corr}}}$, with the solid segment indicating the scaling window used for the fit. Error bars denote the standard error. (**c**) Temporal evolution of the phase correlation function for different initial phase-space densities (PSDs). (**d**) (Left) Correlation functions for various initial states collapse onto a universal scaling curve, displayed on a log–log scale. Inset: the same data shown on a linear scale. (Right, top) Growth of the correlation length for different initial conditions. (Right, bottom) Rescaled correlation length. The black line indicates the fit, and its solid portion marks the scaling window used in the fitting procedure.

Figure 5.8 shows the equal-time phase correlation function $C(r) = C(\overline{x}) = \mathrm{Re}\left[\left\langle e^{i[\theta(x)-\theta(x-\overline{x})]}\right\rangle_x\right]$ at different times after the quench. We observe an increase in phase coherence across the system following the quench, demonstrated by the

growth of the spatial correlation functions. According to the dynamical scaling hypothesis, the correlation functions in the scaling region should evolve in terms of the dynamical scaling form $C(r,t) \sim F\left(r/L_c(t)\right)$, and the growth of the correlation length (domain size) follows $L_c(t) \sim t^{1/z}$ [15]. We determine the characteristic correlation length scale by the distance at which the correlation function satisfies $C(L_c(t),t) = \text{const.}$ [16, 18, 20, 124, 144, 145]; we select this constant value to be centered at 0.75, with resampling in the region $0.7 - 0.8$ to assess the robustness of the obtained L_c values. This methodology gives robust results whilst allowing us to compute the mean and standard deviation of L_c. The correlation functions at various times after t_c collapse onto a common curve when rescaled as $r' = r/L_c(t)$, indicating self-similar dynamics (Figure 5.8b). The extracted L_c exhibits power-law scaling in the scaling window (see Figure 5.9), with a critical exponent $z_{\text{corr}} = 1.72(11)$.

Having verified the scale-invariant dynamics, we now analyze its universal characteristics by varying the initial PSD. In Figure 5.8c, we plot correlation functions for various initial PSDs ($\mathcal{D} = 7.8$ to $\mathcal{D} = 9.3$). At short timescales ($t < 10\,\text{ms}$), we observe the system becomes more disordered. This arises from the spontaneous generation of vortices following a rapid quench, as evidenced by the initial increase in vortex number shown in Figure 5.9c. We extract the correlation length following the method described before and rescale the x axis so that the correlation functions all collapse to a single curve, as demonstrated in Figure 5.8d. The correlation lengths are fitted to a power-law form assuming a universal dynamic exponent shared across all datasets. All datasets are fitted simultaneously using a weighted least-squares regression in log–log space, enforcing a common slope while allowing dataset-specific prefactors. The weights are set by the experimental uncertainties of the correlation length. The fitted parameters are subsequently used to rescale the data, leading to a collapse onto a single curve for improved visual clarity. Uncertainties in the exponent are obtained by bootstrap resampling, in which the full joint fit across all datasets is repeated for each resampled realization, yielding $z_{\text{corr}} = 1.69(14)$ (see Fig. 5.10). This value is consistent, within uncertainties, with the exponent obtained previously.

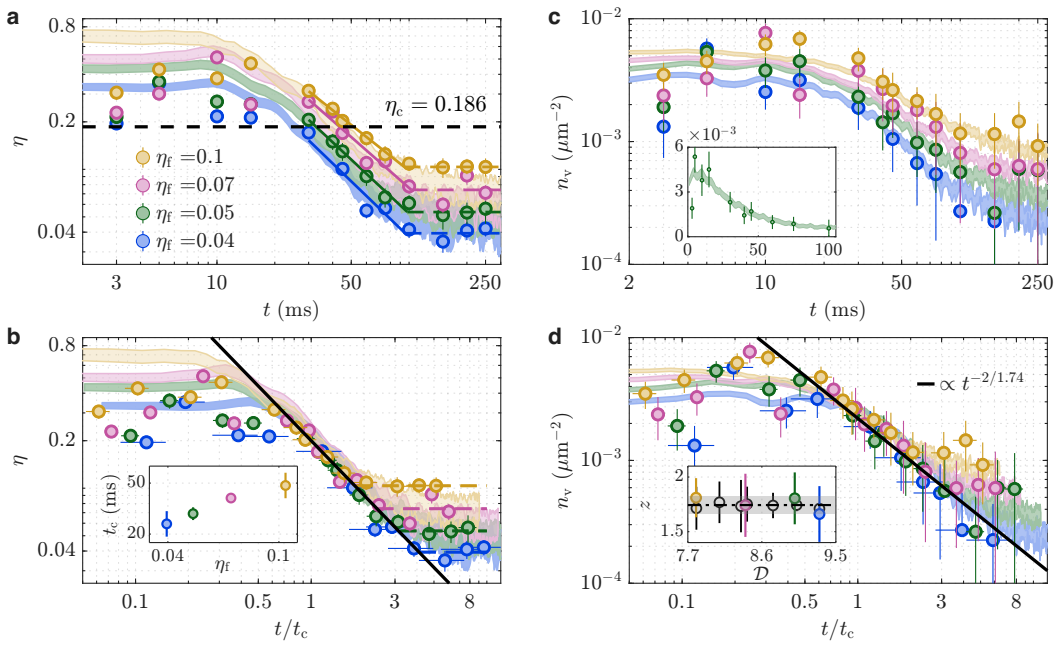

Figure 5.9: Universal scaling behavior. (**a**) Temporal evolution of $\eta(t)$, determined by fitting $C(r)$ with an algebraic model, for four different initial conditions, plotted on a log-log scale. Measurements (dots with error bars denoting fit uncertainties) are shown alongside simulations (represented by shaded regions indicating uncertainty). The horizontal dashed line marks the critical value η_c for the onset of algebraic phase coherence. The solid lines are a guide to the eye, illustrating that η follows a power-law behavior in the scaling window. (**b**) Rescaled time evolution of $\eta(t/t_c)$, demonstrating universal dynamics (indicated by the black solid line). The horizontal error bars arise from the uncertainty in t_c. The inset shows the critical time t_c for different initial conditions. (**c**) Time evolution of the vortex density $n_v(t)$ for different initial conditions on a log-log scale, with error bars indicating the standard error. For $\eta_f = 0.04$ and $t > 150$ ms, no vortices were observed in the finite dataset obtained in this work. The inset is linear plot for a selected initial condition. (**d**) Rescaled vortex density $n_v(t/t_c)$, showing universal dynamics. The solid line indicates a power-law behavior consistent with the scaling $t^{-2/1.74}$. The inset shows the fitted values of the dynamic critical exponent for different initial conditions; the dashed line indicates the mean value, and the shaded area represents the associated uncertainty. Open circles denote the exponent values extracted from simulations using the same fitting method.

We further show that the universal properties can be probed by fitting the correlation function to a power-law form, $C(r) \sim r^{-2\eta}$. Although the full correlation function does not obey a strict power-law dependence (see Fig. 5.8d), such a fit provides a effective measure of the local logarithmic slope and thereby characterizes the degree of order in the system. For a fixed spatial fitting window, the exponents extracted at different times correspond to sampling distinct segments of the same

underlying universal scaling curve. Consequently, any temporal evolution of the fitted η reflects the gradual shift of the fitting window along this universal function. Therefore we expect the extracted η from different initial conditions to converge within the scaling window toward a universal trajectory determined solely by the scaling function. At short timescales ($t < 10\,\mathrm{ms}$), we observe an increase in η, indicating that the system becomes progressively more disordered, consistent with the behavior shown in Fig. 5.8. Around $t = 30$ ms, the system begins to phase-order, and $\eta(t)$ follows a power-law decay in the scaling region, as indicated by the solid lines in Fig. 5.9a. After $\sim 150\,\mathrm{ms}$, $\eta(t)$ reaches a constant value, indicating that the relative mode has attained its steady state. To demonstrate that the evolution trajectory is universal, we rescale time by t_c, defined through the condition $\eta(t_c) = 0.186$.[1] Rescaling the hold time to $t' = t/t_c$, we find that $\eta(t)$ begins to exhibit a universal decay near the critical time $t/t_c = 1$, following a power-law scaling, as shown in Fig. 5.9b.

To demonstrate that the phase-ordering process is governed by the annihilation of topological defects, we analyze the time evolution of the vortex density for the same datasets in Figure 5.9c. We observe power-lay decay of the vortex density $n_v(t)$, indicative of dynamical vortex–antivortex pairing and annihilation. Concurrently, based on the dynamical scaling hypothesis, universal behavior should emerge around and after the critical time t_c, when the correlation length L_c becomes the dominant length scale. The growth of the correlation length $L_c(t)$ and the reduction in vortices $n_v(t)$ are consistent within this framework, predicting that $n_v(t)$ should scale as $n_v(t) \sim L_c^{-2}(t) \sim t^{-2/z}$ [18, 20]. After rescaling the hold time to $t' = t/t_c$ (Figure 5.9d), we observe the universal decay of vortex density following the scaling law $n_v(t) \sim t^{-2/z}$ as predicted by theory, which indicates the system coarsens. However, we find that the decay of free vortices does not continue indefinitely, reaching a plateau after ≈ 150 ms, consistent with the evolution of η. To determine

[1] In principle this reference value can be chosen arbitrarily. Here we determine it by comparing exponential and power-law fits to the correlation function. The time t_c is identified as the point at which the correlation function becomes better described by a power-law decay; the corresponding exponent defines the critical value $\eta_c = 0.186(4)$.

the value of z_{vort}, we employ the same fitting procedure as used for the correlation length. Fitting the data over the interval $40\,\mathrm{ms} \leq t \leq 100\,\mathrm{ms}$ yields a mean exponent $\langle z_{\mathrm{vort}} \rangle = 1.74$ with a standard error of 0.08 (see Fig. 5.10).

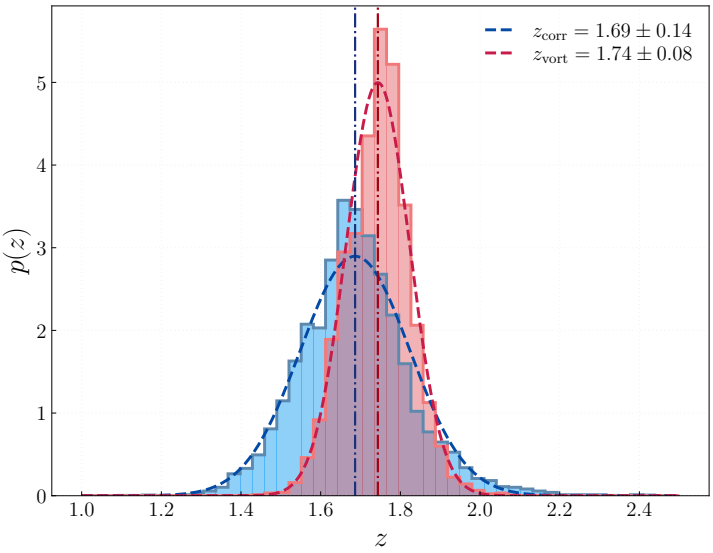

Figure 5.10: Determination of the dynamic critical exponent. Histogram of bootstrapped estimates of the exponent z, obtained from power-law fits of the form $f(t) = A\,t^{1/z_{\mathrm{corr}}}$ to the correlation length and $f(t) = B\,t^{-2/z_{\mathrm{vort}}}$ to the vortex density. The dashed curves represent Gaussian fits to the resulting probability density distributions, and the dash-dotted lines denote the corresponding mean values.

We finally combine the estimates obtained from the correlation length and the vortex density using inverse-variance weighting, yielding a final value of dynamic critical exponent $z = 1.73(7)$. It is close to the numerical results for quenched 2D Bose gas ($z \approx 1.74$ is reported in both the conservative limit and under weak dissipation in Ref. [20]. Ref. [19] finds $\beta \approx 0.56$ for near-Gaussian NTFP, corresponding to $z = 1/\beta \approx 1.79$), suggesting the coarsening dynamics in the coupled bilayer follows the diffusion-type scaling, characterized by dynamic critical exponent $z \sim 2$.

5.5 Phase coherence of states in equilibrium and steady states after the quench

Finally, we compare the phase coherence between the steady state appearing around 150 ms after the quench and the state in thermal equilibrium. To probe

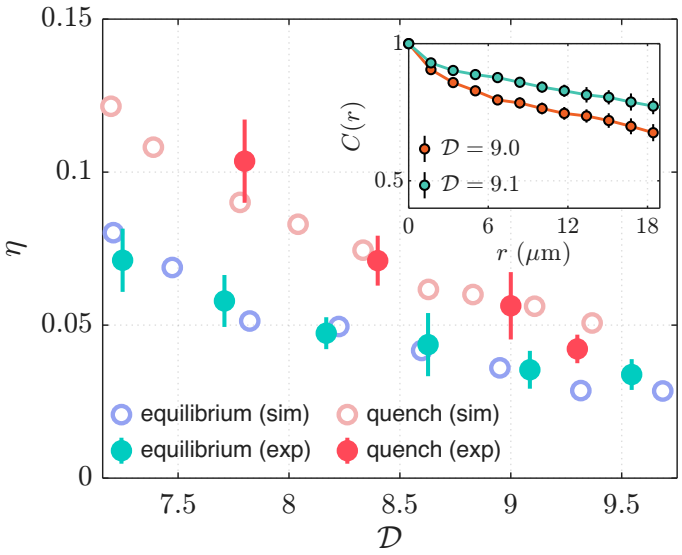

Figure 5.11: Phase coherence of equilibrium and quenched systems. Extracted algebraic decay exponent η from experiment (filled symbols) and numerical simulation (open symbols) for both the thermal equilibrium and steady states observed after the quench, plotted as a function of PSD. For the quenched systems, as in the main text, the PSD for the equilibrium system before the quench is used for this plot. The post-quench steady state is evaluated at $t = 250\,\mathrm{ms}$. Inset: Representative correlation functions from experimental data at two nearly identical PSDs for thermal equilibrium and post-quench steady state.

the system in equilibrium, two atomic clouds are adiabatically loaded into the bilayer potential with a tunnel coupling of $J_c = 34\,\mathrm{Hz}$. The clouds are prepared at the same temperature and held in the trap for a sufficiently long time to ensure equilibration. We then perform matter-wave interferometry (Figure 5.6) and obtain the correlation function of the relative phase. In Figure 5.11, we plot the algebraic exponent η for the equilibrium and steady-state samples, where the post-quench states exhibit systematically larger η than the corresponding equilibrium values. This may originate from the sudden quench projecting the initial thermal states onto excited states of the post-quench Hamiltonian, with the associated work injection raising the system's effective temperature [13, 146]. We further note from numerical simulations that, compared with the thermal equilibrium state, the common phase relaxes toward a larger η on a timescale substantially longer than the $\sim$ 150 ms relaxation of the relative phase.

5.6 Conclusion

In this chapter, we demonstrate universal phase-ordering dynamics in a coupled two-dimensional bilayer system following a coupling quench, revealing good agreement between experimental observations and classical-field simulations. We observe self-similar dynamics characterized by power-law growth of the correlation length with a measured critical exponent $z_{\mathrm{corr}} = 1.69(14)$. The coarsening occurs through vortex-antivortex annihilation, accompanied by a decay of the vortex density with exponent $z_{\mathrm{vort}} = 1.74(8)$. Combining these estimates yields a dynamic critical exponent $z = 1.73(7)$. The consistency between the two measurements indicates that the coarsening dynamics is governed by a single growing length scale and is consistent with diffusion-like behavior. The results advance the understanding of universal dynamics following an explicit symmetry breaking quench and provide a robust foundation for testing effective field theories of out-of-equilibrium systems, such as the coupled 2D XY model and 2D sine-Gordon model with defect excitations.

6 Conclusion and Outlook

Contents

6.1 Conclusion

This thesis presents both numerical and experimental studies of tunnel-coupled 2D bilayer Bose gases at finite temperatures, exploring their behaviour in and out of equilibrium. Using classical-field Monte Carlo simulations, we investigated bilayer systems with varying interlayer coupling strengths and different types of interlayer interactions. Owing to their broad applicability, classical Monte Carlo methods provide a convenient and accurate means to simulate not only current experiments but also future scenarios where quantum entanglement can be neglected. We further combined the Monte Carlo approach with the Gross–Pitaevskii equation to study the nonequilibrium dynamics of the bilayer system. In simulations of the Josephson effect, performed under experimentally realistic conditions, we observed that the formation of two-dimensional sine–Gordon solitons (domain

walls) leads to damping of the oscillations. A detailed analysis of the domain-wall dynamics is presented, including a classification of different types of linearly confined vortex–antivortex pairs.

We then experimentally investigated the relaxation dynamics of the relative sector of bilayer quasi-2D clouds following a sudden coupling quench. This was achieved through precise control of the barrier height and separation of the MRF-dressed double-well potential. The initial clouds were prepared in the normal (disordered) phase, and the system is subsequently quenched into the bilayer superfluid (BSF) phase. We studied the subsequent evolution of the phase-correlation function and the vortex dynamics, finding that the relative phase exhibits universal phase-ordering dynamics characteristic of diffusion-like coarsening. The experimental observations are further supported by numerical simulations. These results demonstrate that coarsening dynamics can occur (at least transiently) following an explicitly symmetry-breaking quench, providing the foundation and motivation for further theoretical studies of nonequilibrium dynamics in effective field theories.

6.2 Future experiments

6.2.1 Josephson effects in bilayer 2D Bose gases

The numerical simulations presented in this work reveal rich dynamics and excitations unique to 2D systems. The MRF-dressed double-well potential provides a reliable platform for experimentally exploring Josephson effects. A controlled phase difference can be imprinted by coherently splitting a single cloud into two decoupled clouds with approximately equal atom numbers, followed by the introduction of an energy bias [4, 7, 62]. The 2D domain walls formed during the dynamics can be probed via a vertical imaging system employing selective repumping after a short time of flight (TOF), as shown in Figure 6.1, enabling interference between the two clouds [107]. Matter-wave interferometry also provides a natural way of probing the dynamics of the relative phase, as demonstrated in this thesis.

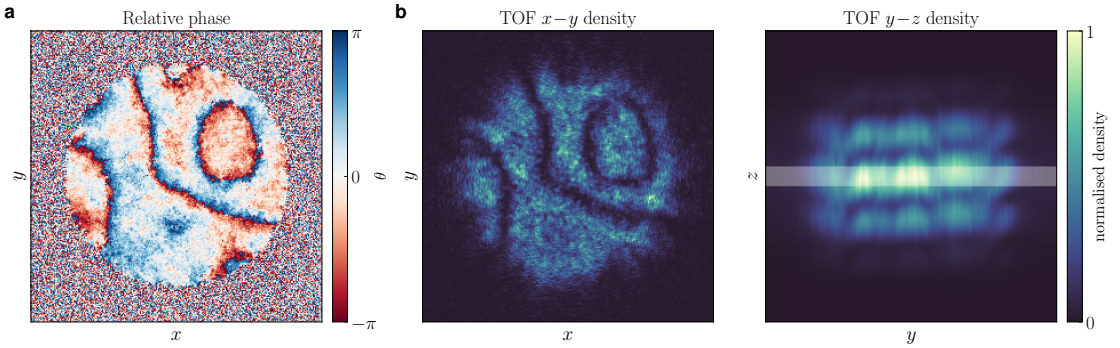

Figure 6.1: Simulation of experimental probe of 2D domain walls. (**a**) *In situ* wrapped relative phase profile. (**b**) (Left) Integrated x–y density profile, obtained by integrating along the z direction over a width of 5 μm after a time of flight (TOF) of 5 ms. (Right) Interference density pattern extracted from the same TOF distribution and integrated along the x axis; the white shaded region denotes the spatial region corresponding to the z-integration window (of width 5 μm) used to obtain the x–y density profile in the left panel.

6.2.2 Higher-order correlation

In this work, the system is characterized using the two-point correlation function. For a Gaussian system, this function provides complete information about correlations, as the state is fully determined by its first and second moments (mean and variance). According to Wick's theorem [147], all higher-order correlation functions can be factorized into products of two-point correlations, assuming a vanishing first moment. However, when the system is non-Gaussian (for example, in a tunnel-coupled bilayer system with finite interlayer coupling strength) higher-order correlation functions are required for a comprehensive description. There are two good and well-established approaches for probing such higher-order correlations: the method of full counting statistics (or full probability distributions) [148–151], and the direct calculation and decomposition of higher-order correlation functions introduced in Ref. [134]. The first method has been experimentally implemented by Abel Beregi and used to demonstrate the universality of a 2D Bose gas in the superfluid regime, as well as to analyze higher-moment statistics [63, 152]. The latter method provides a powerful approach to investigate non-Gaussianity in the system by separating the connected and disconnected parts of the spatial correlation functions. Experimentally implementing this approach in 2D systems would offer valuable

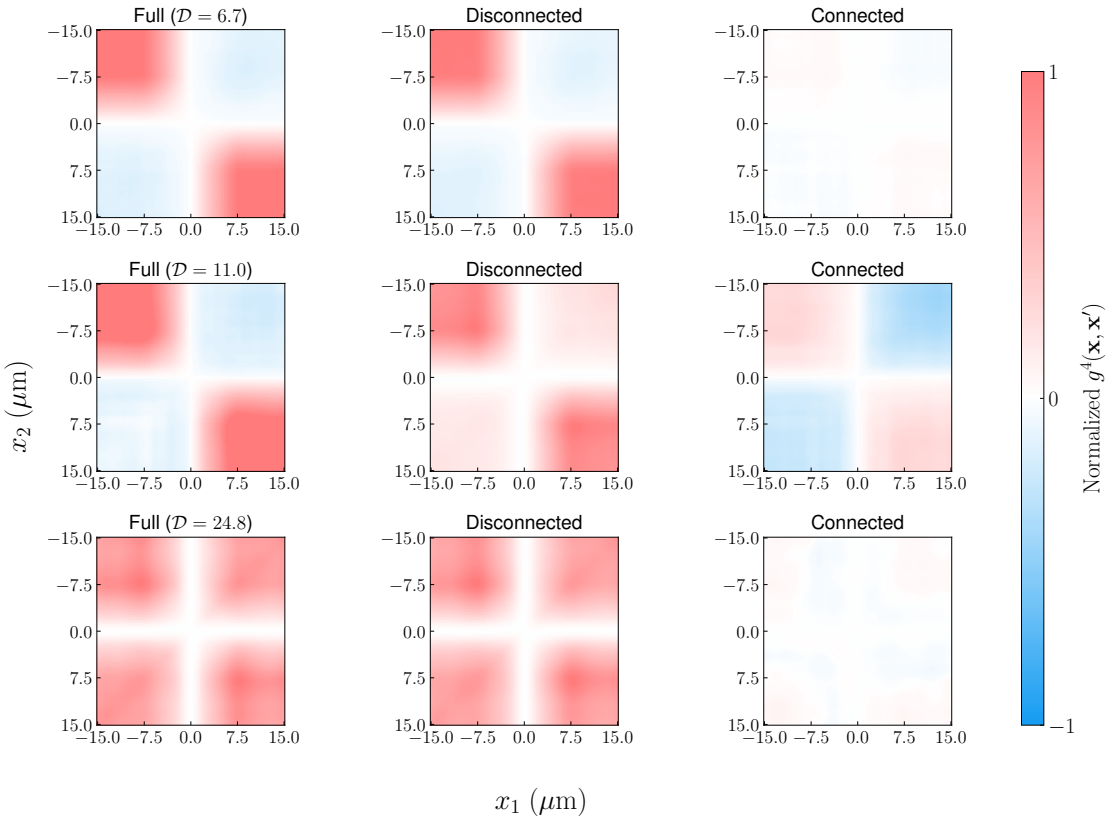

Figure 6.2: Decomposition of the fourth-order phase correlation function. The four-point phase correlation function $g^{(4)}(\mathbf{x}, \mathbf{x}')$ is shown by fixing two reference points at $x_3 = -x_4 = 7.5$ μm. The left column presents the full fourth-order correlation function, the center column shows the disconnected contribution reconstructed from products of two-point correlations, and the right column displays the connected contribution, which reflects genuine higher-order, non-Gaussian correlations. Each row corresponds to a different PSD $\mathcal{D}$, and are normalised to $[-1, 1]$.

insights into the underlying many-body correlations, both in and out of equilibrium. In Figure 6.2, we present an example of the decomposition of the fourth-order phase correlation function $g^{(4)}(\mathbf{x}, \mathbf{x}')$, obtained by analysing the simulated relative phase of a decoupled bilayer 2D Bose gas simulations. [1] We follow the definition of the fourth-order correlation function provided in Ref. [134].

[1] We find that the superfluid regime (high PSD) is well described by Gaussian correlations, consistent with the quadratic Hamiltonian (see the harmonic XY model or Eq. (2.52)). The system exhibits non-Gaussian behavior near the critical PSD $\mathcal{D}_c \approx 11$, as the vortex–antivortex pairs begin to unbind and the quadratic approximation breaks down. Interestingly, at low PSD the system again approaches Gaussian behavior. This seemingly counterintuitive trend can be explained by the central limit theorem, as fluctuations become dominated by many uncorrelated regions.

References

[1] N. D. Mermin and H. Wagner, "Absence of Ferromagnetism or Antiferromagnetism in One- or Two-Dimensional Isotropic Heisenberg Models", Physical Review Letters **17**, 1133 (1966).

[2] V. L. Berezinsky, "Destruction of long range order in one-dimensional and two-dimensional systems having a continuous symmetry group. I. Classical systems", Sov. Phys. JETP **32**, 493 (1971).

[3] J. M. Kosterlitz and D. J. Thouless, "Ordering, metastability and phase transitions in two-dimensional systems", Journal of Physics C: Solid State Physics **6**, 1181 (1973).

[4] T. Berrada, S. van Frank, R. Bücker, T. Schumm, J.-F. Schaff, and J. Schmiedmayer, "Integrated Mach–Zehnder interferometer for Bose–Einstein condensates", Nature Communications **4**, 2077 (2013).

[5] G. Spagnolli, G. Semeghini, L. Masi, G. Ferioli, A. Trenkwalder, S. Coop, M. Landini, L. Pezzè, G. Modugno, M. Inguscio, A. Smerzi, and M. Fattori, "Crossing Over from Attractive to Repulsive Interactions in a Tunneling Bosonic Josephson Junction", Physical Review Letters **118**, 230403 (2017).

[6] S. Levy, E. Lahoud, I. Shomroni, and J. Steinhauer, "The a.c. and d.c. Josephson effects in a Bose–Einstein condensate", Nature **449**, 579 (2007).

[7] M. Pigneur, T. Berrada, M. Bonneau, T. Schumm, E. Demler, and J. Schmiedmayer, "Relaxation to a Phase-Locked Equilibrium State in a One-Dimensional Bosonic Josephson Junction", Physical Review Letters **120**, 173601 (2018).

[8] N. Luick, L. Sobirey, M. Bohlen, V. P. Singh, L. Mathey, T. Lompe, and H. Moritz, "An ideal Josephson junction in an ultracold two-dimensional Fermi gas", Science **369**, 89 (2020).

[9] L. Mathey and A. Polkovnikov, "Light cone dynamics and reverse Kibble-Zurek mechanism in two-dimensional superfluids following a quantum quench", Physical Review A **81**, 033605 (2010).

[10] S. Sunami, V. P. Singh, D. Garrick, A. Beregi, A. J. Barker, K. Luksch, E. Bentine, L. Mathey, and C. J. Foot, "Universal scaling of the dynamic BKT transition in quenched 2D Bose gases", Science **382**, 443 (2023).

[11] E. G. Dalla Torre, E. Demler, and A. Polkovnikov, "Universal Rephasing Dynamics after a Quantum Quench via Sudden Coupling of Two Initially Independent Condensates", Physical Review Letters **110**, 090404 (2013).

[12] M. A. Cazalilla, A. Iucci, and T. Giamarchi, "Competition between vortex unbinding and tunneling in an optical lattice", Physical Review A **75**, 051603 (2007).

[13] L. Mathey, A. Polkovnikov, and A. H. Castro Neto, "Phase-locking transition of coupled low-dimensional superfluids", Europhysics Letters **81**, 10008 (2007).

[14] E. Rydow, V. P. Singh, A. Beregi, E. Chang, L. Mathey, C. J. Foot, and S. Sunami, "Observation of a bilayer superfluid with interlayer coherence", Nature Communications **16**, 7201 (2025).

[15] A. Bray, "Theory of phase-ordering kinetics", Advances in Physics **43**, 357 (1994).

[16] L. A. Williamson and P. B. Blakie, "Universal Coarsening Dynamics of a Quenched Ferromagnetic Spin-1 Condensate", Physical Review Letters **116**, 025301 (2016).

[17] L. A. Williamson and P. B. Blakie, "Coarsening Dynamics of an Isotropic Ferromagnetic Superfluid", Physical Review Letters **119**, 255301 (2017).

[18] P. Comaron, F. Larcher, F. Dalfovo, and N. P. Proukakis, "Quench dynamics of an ultracold two-dimensional Bose gas", Physical Review A **100**, 033618 (2019).

[19] M. Karl and T. Gasenzer, "Strongly anomalous non-thermal fixed point in a quenched two-dimensional Bose gas", New Journal of Physics **19**, 093014 (2017).

[20] A. J. Groszek, P. Comaron, N. P. Proukakis, and T. P. Billam, "Crossover in the dynamical critical exponent of a quenched two-dimensional Bose gas", Physical Review Research **3**, 013212 (2021).

[21] V. P. Singh and L. Mathey, "Sound propagation in a two-dimensional Bose gas across the superfluid transition", Physical Review Research **2**, 023336 (2020).

[22] V. P. Singh and L. Mathey, "First and second sound in a dilute Bose gas across the BKT transition", New Journal of Physics **24**, 073024 (2022).

[23] S. Sunami, V. P. Singh, D. Garrick, A. Beregi, A. J. Barker, K. Luksch, E. Bentine, L. Mathey, and C. J. Foot, "Observation of the Berezinskii-Kosterlitz-Thouless Transition in a Two-Dimensional Bose Gas via Matter-Wave Interferometry", Physical Review Letters **128**, 250402 (2022).

[24] P. M. Chaikin and T. C. Lubensky, *Principles of Condensed Matter Physics* (Cambridge University Press, Cambridge, 1995).

[25] A. Altland and B. D. Simons, *Condensed Matter Field Theory*, 2nd ed. (Cambridge University Press, Cambridge, 2010).

[26] J. M. Kosterlitz, "The critical properties of the two-dimensional xy model", Journal of Physics C: Solid State Physics **7**, 1046 (1974).

[27] X. G. Wen, *Quantum Field Theory of Many-Body Systems* (Oxford University Press, Oxford, 2007).

[28] P. Minnhagen, "The two-dimensional Coulomb gas, vortex unbinding, and superfluid-superconducting films", Reviews of Modern Physics **59**, 1001 (1987).

[29] K. G. Wilson and J. Kogut, "The renormalization group and the expansion", Physics Reports **12**, 75 (1974).

[30] L. Benfatto, C. Castellani, and T. Giamarchi, "Kosterlitz-Thouless Behavior in Layered Superconductors: The Role of the Vortex Core Energy", Physical Review Letters **98**, 117008 (2007).

[31] G. Bighin, N. Defenu, I. Nándori, L. Salasnich, and A. Trombettoni, "Berezinskii-Kosterlitz-Thouless Paired Phase in Coupled XY Models", Physical Review Letters **123**, 100601 (2019).

[32] T. Xiao, Y. Deng, and X.-Y. Dong, "Fate of the Berezinskii-Kosterlitz-Thouless paired phase in coupled XY models", Phys. Rev. B **112**, 144420.

[33] A. Masini, A. Cuccoli, A. Rettori, A. Trombettoni, and F. Cinti, "Helicity modulus in the bilayer XY model by the Monte Carlo worm algorithm", Physical Review B **111**, 094415 (2025).

[34] Z. Hadzibabic and J. Dalibard, "Two-dimensional Bose fluids: An atomic physics perspective", La Rivista del Nuovo Cimento **34**, 389 (2011).

[35] C. J. Pethick and H. Smith, *Bose–Einstein Condensation in Dilute Gases*, 2nd ed. (Cambridge University Press, Cambridge, 2008).

[36] D. S. Petrov, M. Holzmann, and G. V. Shlyapnikov, "Bose-Einstein Condensation in Quasi-2D Trapped Gases", Physical Review Letters **84**, 2551 (2000).

[37] A. Görlitz, J. M. Vogels, A. E. Leanhardt, C. Raman, T. L. Gustavson, J. R. Abo-Shaeer, A. P. Chikkatur, S. Gupta, S. Inouye, T. Rosenband, and W. Ketterle, "Realization of Bose-Einstein Condensates in Lower Dimensions", Physical Review Letters **87**, 130402 (2001).

[38] O. Zobay and B. M. Garraway, "Two-Dimensional Atom Trapping in Field-Induced Adiabatic Potentials", Physical Review Letters **86**, 1195 (2001).

[39] P. Krüger, Z. Hadzibabic, and J. Dalibard, "Critical Point of an Interacting Two-Dimensional Atomic Bose Gas", Physical Review Letters **99**, 040402 (2007).

[40] P. Cladé, C. Ryu, A. Ramanathan, K. Helmerson, and W. D. Phillips, "Observation of a 2D Bose Gas: From Thermal to Quasicondensate to Superfluid", Physical Review Letters **102**, 170401 (2009).

[41] T. Yefsah, R. Desbuquois, L. Chomaz, K. J. Günter, and J. Dalibard, "Exploring the Thermodynamics of a Two-Dimensional Bose Gas", Physical Review Letters **107**, 130401 (2011).

[42] R. Desbuquois, L. Chomaz, T. Yefsah, J. Léonard, J. Beugnon, C. Weitenberg, and J. Dalibard, "Superfluid behaviour of a two-dimensional Bose gas", Nature Physics **8**, 645 (2012).

[43] M. Holzmann and W. Krauth, "Kosterlitz-Thouless Transition of the Quasi-Two-Dimensional Trapped Bose Gas", Physical Review Letters **100**, 190402 (2008).

[44] C. Mora and Y. Castin, "Extension of Bogoliubov theory to quasicondensates", Physical Review A **67**, 053615 (2003).

[45] S. Nazarenko, M. Onorato, and D. Proment, "Bose-Einstein condensation and Berezinskii-Kosterlitz-Thouless transition in the two-dimensional nonlinear Schr\"odinger model", Physical Review A **90**, 013624 (2014).

[46] D. R. Nelson and J. M. Kosterlitz, "Universal Jump in the Superfluid Density of Two-Dimensional Superfluids", Physical Review Letters **39**, 1201 (1977).

[47] I. Boettcher and M. Holzmann, "Quasi-long-range order in trapped two-dimensional Bose gases", Physical Review A **94**, 011602 (2016).

[48] S. Klabnik and C. Nichols, *The Rust programming language*, Second edition. (No Starch Press, Inc., San Francisco, 2023).

[49] NVIDIA Corporation, *CUDA C++ Programming Guide*, Version 13.1 (2025).

[50] G. E. Uhlenbeck and L. S. Ornstein, "On the Theory of the Brownian Motion", Physical Review **36**, 823 (1930).

[51] D. T. Gillespie, "Exact numerical simulation of the Ornstein-Uhlenbeck process and its integral", Physical Review E **54**, 2084 (1996).

[52] H.-P. Stimming, N. J. Mauser, J. Schmiedmayer, and I. E. Mazets, "Fluctuations and Stochastic Processes in One-Dimensional Many-Body Quantum Systems", Physical Review Letters **105**, 015301 (2010).

[53] T. Betz, S. Manz, R. Bücker, T. Berrada, C. Koller, G. Kazakov, I. E. Mazets, H.-P. Stimming, A. Perrin, T. Schumm, and J. Schmiedmayer, "Two-Point Phase Correlations of a One-Dimensional Bosonic Josephson Junction", Physical Review Letters **106**, 020407 (2011).

[54] P. Grišins and I. E. Mazets, "Coherence and Josephson oscillations between two tunnel-coupled one-dimensional atomic quasicondensates at finite temperature", Physical Review A **87**, 013629 (2013).

[55] N. K. Whitlock and I. Bouchoule, "Relative phase fluctuations of two coupled one-dimensional condensates", Physical Review A **68**, 053609 (2003).

[56] I. E. Mazets, "Two-dimensional dynamics of expansion of a degenerate Bose gas", Physical Review A **86**, 055603 (2012).

[57] N. Prokof'ev, O. Ruebenacker, and B. Svistunov, "Critical Point of a Weakly Interacting Two-Dimensional Bose Gas", Physical Review Letters **87**, 270402 (2001).

[58] N. Metropolis, A. W. Rosenbluth, M. N. Rosenbluth, A. H. Teller, and E. Teller, "Equation of State Calculations by Fast Computing Machines", The Journal of Chemical Physics **21**, 1087 (1953).

[59] M. Patra and M. Karttunen, "Stencils with isotropic discretization error for differential operators", Numerical Methods for Partial Differential Equations **22**, 936 (2006).

[60] U. Wolff, "Critical slowing down", Nuclear Physics B - Proceedings Supplements **17**, 93 (1990).

[61] H. Weber and P. Minnhagen, "Monte Carlo determination of the critical temperature for the two-dimensional XY model", Physical Review B **37**, 5986 (1988).

[62] S. Sunami, "Non-equilibrium dynamics in two-dimensional quantum systems", PhD thesis (University of Oxford, 2021).

[63] A. Beregi, "Probing universality of 2D quantum systems with bilayer Bose gases", PhD thesis (University of Oxford, 2024).

[64] C. J. Foster, P. B. Blakie, and M. J. Davis, "Vortex pairing in two-dimensional Bose gases", Physical Review A **81**, 023623 (2010).

[65] M. Sesodia, S. Sunami, E. Chang, E. Rydow, C. J. Foot, and A. Beregi, "CNN-Based vortex detection in atomic 2D Bose gases in the presence of a phononic background", Machine Learning: Science and Technology **6**, 015067 (2025).

[66] E. Rydow, "In preparation", PhD thesis (University of Oxford).

[67] J. V. José, L. P. Kadanoff, S. Kirkpatrick, and D. R. Nelson, "Renormalization, vortices, and symmetry-breaking perturbations in the two-dimensional planar model", Physical Review B **16**, 1217 (1977).

[68] H. A. Fertig, "Deconfinement in the Two-Dimensional XY Model", Physical Review Letters **89**, 035703 (2002).

[69] H. A. Fertig and K. Majumdar, "Vortex deconfinement in the XY model with a magnetic field", Annals of Physics **305**, 190 (2003).

[70] W. Zhang and H. A. Fertig, "Vortices and dissipation in a bilayer thin film superconductor", Physical Review B **71**, 224514 (2005).

[71] J. R. Cash and A. H. Karp, "A variable order Runge-Kutta method for initial value problems with rapidly varying right-hand sides", ACM Trans. Math. Softw. **16**, 201 (1990).

[72] L. J. LeBlanc, A. B. Bardon, J. McKeever, M. H. T. Extavour, D. Jervis, J. H. Thywissen, F. Piazza, and A. Smerzi, "Dynamics of a Tunable Superfluid Junction", Physical Review Letters **106**, 025302 (2011).

[73] B. D. Josephson, "Possible new effects in superconductive tunnelling", Physics Letters **1**, 251 (1962).

[74] J. C. Davis and R. E. Packard, "Superfluid ${}^{3}\mathrm{He}$ Josephson weak links", Reviews of Modern Physics **74**, 741 (2002).

[75] M. Albiez, R. Gati, J. Fölling, S. Hunsmann, M. Cristiani, and M. K. Oberthaler, "Direct Observation of Tunneling and Nonlinear Self-Trapping in a Single Bosonic Josephson Junction", Physical Review Letters **95**, 010402 (2005).

[76] A. Smerzi, S. Fantoni, S. Giovanazzi, and S. R. Shenoy, "Quantum Coherent Atomic Tunneling between Two Trapped Bose-Einstein Condensates", Physical Review Letters **79**, 4950 (1997).

[77] D. Ananikian and T. Bergeman, "Gross-Pitaevskii equation for Bose particles in a double-well potential: Two-mode models and beyond", Physical Review A **73**, 013604 (2006).

[78] R. Gati and M. K. Oberthaler, "A bosonic Josephson junction", Journal of Physics B: Atomic, Molecular and Optical Physics **40**, R61 (2007).

[79] "Interferometry with atoms", La Rivista del Nuovo Cimento **37**, 509 (2014).

[80] A. J. Leggett, "Bose-Einstein condensation in the alkali gases: Some fundamental concepts", Reviews of Modern Physics **73**, 307 (2001).

[81] B. Rauer, S. Erne, T. Schweigler, F. Cataldini, M. Tajik, and J. Schmiedmayer, "Recurrences in an isolated quantum many-body system", Science **360**, 307 (2018).

[82] J.-F. Mennemann, I. E. Mazets, M. Pigneur, H. P. Stimming, N. J. Mauser, J. Schmiedmayer, and S. Erne, "Relaxation in an extended bosonic Josephson junction", Phys. Rev. Res. **3**, 023197 (2021).

[83] A. Burchianti, F. Scazza, A. Amico, G. Valtolina, J. A. Seman, C. Fort, M. Zaccanti, M. Inguscio, and G. Roati, "Connecting Dissipation and Phase Slips in a Josephson Junction between Fermionic Superfluids", Physical Review Letters **120**, 025302 (2018).

[84] S. Sinha and S. Sinha, "Dissipative Bose-Josephson junction coupled to bosonic baths", Physical Review E **100**, 032115 (2019).

[85] V. P. Singh, N. Luick, L. Sobirey, and L. Mathey, "Josephson junction dynamics in a two-dimensional ultracold Bose gas", Physical Review Research **2**, 033298 (2020).

[86] D. T. Son and M. A. Stephanov, "Domain walls of relative phase in two-component Bose-Einstein condensates", Phys. Rev. A **65**, 063621 (2002).

[87] M. Eto and M. Nitta, "Confinement of half-quantized vortices in coherently coupled Bose-Einstein condensates: Simulating quark confinement in a QCD-like theory", Phys. Rev. A **97**, 023613 (2018).

[88] M. Eto, K. Ikeno, and M. Nitta, "Collision dynamics and reactions of fractional vortex molecules in coherently coupled Bose-Einstein condensates", Phys. Rev. Res. **2**, 033373 (2020).

[89] A. Corney, *Atomic and laser spectroscopy* (Oxford University Press, Oct. 2006).

[90] C. Foot, *Atomic physics* (University Press, Oxford, 2005).

[91] C. Cohen-Tannoudji and S. Reynaud, "Dressed-atom description of resonance fluorescence and absorption spectra of a multi-level atom in an intense laser beam", Journal of Physics B: Atomic and Molecular Physics **10**, 345 (1977).

[92] C. Cohen-Tannoudji, J. Dupont-Roc, and G. Grynberg, *Atom-photon interactions : basic processes and applications* (Wiley-VCH, Weinheim, 2004).

[93] P. R. Berman, C. C. Lin, and E. Arimondo, *Advances in atomic, molecular, and optical physics. Volume 54* (Elsevier/Academic Press, Amsterdam ; 2007).

[94] K. Luksch, "Investigating the spectrum of atoms in multiple-radiofrequency dressed potentials for coherent splitting of quantum gases", PhD thesis (University of Oxford, 2019).

[95] J. H. Shirley, "Solution of the Schrödinger Equation with a Hamiltonian Periodic in Time", Phys. Rev. **138**, B979 (1965).

[96] T. L. Harte, E. Bentine, K. Luksch, A. J. Barker, D. Trypogeorgos, B. Yuen, and C. J. Foot, "Ultracold atoms in multiple radio-frequency dressed adiabatic potentials", Physical Review A **97**, 013616 (2018).

[97] K. Merloti, R. Dubessy, L. Longchambon, A. Perrin, P.-E. Pottie, V. Lorent, and H. Perrin, "A two-dimensional quantum gas in a magnetic trap", New Journal of Physics **15**, 033007 (2013).

[98] M. Gildemeister, "Trapping ultracold atoms in time-averaged adiabatic potentials", PhD thesis (University of Oxford, 2010).

[99] T. Harte, "Ultracold atoms in dressed potentials", PhD thesis (University of Oxford, 2017).

[100] E. Bentine, "Atomic mixtures in radiofrequency dressed potentials", PhD thesis (University of Oxford, 2018).

[101] A. Barker, "Bose gases in double-well potentials", PhD thesis (University of Oxford, 2020).

[102] D. Garrick, "Two-dimensional Bose gases in systems with pointlike disorder", PhD thesis (University of Oxford, 2022).

[103] K. I. Lee, J. A. Kim, H. R. Noh, and W. Jhe, "Single-beam atom trap in a pyramidal and conical hollow mirror", Opt. Lett. **21**, 1177 (1996).

[104] D. Steck, "Rubidium 87 D Line Data", (2003).

[105] I. Lesanovsky and W. von Klitzing, "Time-Averaged Adiabatic Potentials: Versatile Matter-Wave Guides and Atom Traps", Phys. Rev. Lett. **99**, 083001 (2007).

[106] K. Hueck, N. Luick, L. Sobirey, J. Siegl, T. Lompe, H. Moritz, L. W. Clark, and C. Chin, "Calibrating high intensity absorption imaging of ultracold atoms", Opt. Express **25**, 8670 (2017).

[107] S. Sunami, V. P. Singh, E. Rydow, A. Beregi, E. Chang, L. Mathey, and C. J. Foot, "Detecting Phase Coherence of 2D Bose Gases via Noise Correlations", Physical Review Letters **134**, 183407 (2025).

[108] R. Micha and I. I. Tkachev, "Relativistic Turbulence: A Long Way from Preheating to Equilibrium", Phys. Rev. Lett. **90**, 121301 (2003).

[109] T. W. B. Kibble, "Topology of cosmic domains and strings", Journal of Physics A: Mathematical and General **9**, 1387 (1976).

[110] W. H. Zurek, "Cosmological experiments in superfluid helium?", Nature **317**, 505 (1985).

[111] I. Chuang, R. Durrer, N. Turok, and B. Yurke, "Cosmology in the Laboratory: Defect Dynamics in Liquid Crystals", Science **251**, 1336 (1991).

[112] J. Berges, K. Boguslavski, S. Schlichting, and R. Venugopalan, "Turbulent thermalization process in heavy-ion collisions at ultrarelativistic energies", Physical Review D **89**, 074011 (2014).

[113] M. Prüfer, P. Kunkel, H. Strobel, S. Lannig, D. Linnemann, C.-M. Schmied, J. Berges, T. Gasenzer, and M. K. Oberthaler, "Observation of universal dynamics in a spinor Bose gas far from equilibrium", Nature **563**, 217 (2018).

[114] A. N. Mikheev, I. Siovitz, and T. Gasenzer, "Universal dynamics and non-thermal fixed points in quantum fluids far from equilibrium", The European Physical Journal Special Topics **232**, 3393 (2023).

[115] S. Huh, K. Mukherjee, K. Kwon, J. Seo, J. Hur, S. I. Mistakidis, H. R. Sadeghpour, and J.-y. Choi, "Universality class of a spinor Bose–Einstein condensate far from equilibrium", Nature Physics **20**, 402 (2024).

[116] A. Lamacraft, "Quantum Quenches in a Spinor Condensate", Physical Review Letters **98**, 160404 (2007).

[117] A. Bourges and P. B. Blakie, "Different growth rates for spin and superfluid order in a quenched spinor condensate", Physical Review A **95**, 023616 (2017).

[118] S. Mukerjee, C. Xu, and J. E. Moore, "Dynamical models and the phase ordering kinetics of the $s = 1$ spinor condensate", Physical Review B **76**, 104519 (2007).

[119] C.-M. Schmied, T. Gasenzer, and P. B. Blakie, "Violation of single-length-scaling dynamics via spin vortices in an isolated spin-1 Bose gas", Physical Review A **100**, 033603 (2019).

[120] J. Hofmann, S. S. Natu, and S. Das Sarma, "Coarsening Dynamics of Binary Bose Condensates", Physical Review Letters **113**, 095702 (2014).

[121] K. Fujimoto, K. Haneda, K. Kudo, and Y. Kawaguchi, "Scale-invariant relaxation dynamics in two-component Bose-Einstein condensates with large particle-number imbalance", Physical Review A **101**, 023608 (2020).

[122] V. P. Singh, L. Amico, and L. Mathey, "Thermal suppression of demixing dynamics in a binary condensate", Physical Review Research **5**, 043042 (2023).

[123] Rajat, P. Banger, and S. Gautam, "Collective excitations and universal coarsening dynamics of a spin-orbit-coupled spin-1 Bose-Einstein condensate", Physical Review A **111**, 033316 (2025).

[124] M. Kulczykowski and M. Matuszewski, "Phase ordering kinetics of a nonequilibrium exciton-polariton condensate", Physical Review B **95**, 075306 (2017).

[125] P. Comaron, G. Dagvadorj, A. Zamora, I. Carusotto, N. P. Proukakis, and M. H. Szymańska, "Dynamical Critical Exponents in Driven-Dissipative Quantum Systems", Physical Review Letters **121**, 095302 (2018).

[126] V. N. Gladilin and M. Wouters, "Multivortex states and dynamics in nonequilibrium polariton condensates", Journal of Physics A: Mathematical and Theoretical **52**, 395303 (2019).

[127] T. Manovitz, S. H. Li, S. Ebadi, R. Samajdar, A. A. Geim, S. J. Evered, D. Bluvstein, H. Zhou, N. U. Koyluoglu, J. Feldmeier, P. E. Dolgirev, N. Maskara, M. Kalinowski, S. Sachdev, D. A. Huse, M. Greiner, V. Vuletić, and M. D. Lukin, "Quantum coarsening and collective dynamics on a programmable simulator", Nature **638**, 86 (2025).

[128] M. Gazo, A. Karailiev, T. Satoor, C. Eigen, M. Gałka, and Z. Hadzibabic, "Universal coarsening in a homogeneous two-dimensional Bose gas", Science **389**, 802 (2025).

[129] A. J. Leggett, "What DO we know about high Tc?", Nature Physics **2**, 134 (2006).

[130] J.-i. Okamoto, W. Hu, A. Cavalleri, and L. Mathey, "Transiently enhanced interlayer tunneling in optically driven high-T_c superconductors", Physical Review B **96**, 144505 (2017).

[131] G. Homann, M. H. Michael, J. G. Cosme, and L. Mathey, "Dissipationless Counterflow Currents above T_c in Bilayer Superconductors", Physical Review Letters **132**, 096002 (2024).

[132] M. Kobayashi, M. Eto, and M. Nitta, "Berezinskii-kosterlitz-thouless transition of two-component bose mixtures with intercomponent josephson coupling", Physical Review Letters **123**, 075303 (2019).

[133] M. Tylutki, L. P. Pitaevskii, A. Recati, and S. Stringari, "Confinement and precession of vortex pairs in coherently coupled Bose-Einstein condensates", Physical Review A **93**, 043623 (2016).

[134] T. Schweigler, V. Kasper, S. Erne, I. Mazets, B. Rauer, F. Cataldini, T. Langen, T. Gasenzer, J. Berges, and J. Schmiedmayer, "Experimental characterization of a quantum many-body system via higher-order correlations", Nature **545**, 323 (2017).

[135] D. X. Horváth, I. Lovas, M. Kormos, G. Takács, and G. Zaránd, "Nonequilibrium time evolution and rephasing in the quantum sine-Gordon model", Physical Review A **100**, 013613 (2019).

[136] A. Tononi, F. Toigo, S. Wimberger, A. Cappellaro, and L. Salasnich, "Dephasing–rephasing dynamics of one-dimensional tunneling quasicondensates", New Journal of Physics **22**, 073020 (2020).

[137] A. Bastianello, "Sine-Gordon model from coupled condensates: A generalized hydrodynamics viewpoint", Physical Review B **109**, 035118 (2024).

[138] D. Szász-Schagrin, I. Lovas, and G. Takács, "Nonequilibrium time evolution in the sine-Gordon model", Physical Review B **109**, 014308 (2024).

[139] P. Heinen, A. N. Mikheev, and T. Gasenzer, "Anomalous scaling at nonthermal fixed points of the sine-Gordon model", Physical Review A **107**, 043303 (2023).

[140] A. J. Barker, S. Sunami, D. Garrick, A. Beregi, K. Luksch, E. Bentine, and C. J. Foot, "Coherent splitting of two-dimensional Bose gases in magnetic potentials", New Journal of Physics **22**, 103040 (2020).

[141] A. Beregi, C. Foot, and S. Sunami, "Quantum simulations with bilayer 2D Bose gases in multiple-RF-dressed potentials", AVS Quantum Science **6**, 030501 (2024).

[142] Z. Hadzibabic, P. Krüger, M. Cheneau, B. Battelier, and J. Dalibard, "Berezinskii–Kosterlitz–Thouless crossover in a trapped atomic gas", Nature **441**, 1118 (2006).

[143] Y. D. van Nieuwkerk and F. Essler, "On the low-energy description for tunnel-coupled one-dimensional Bose gases", SciPost Physics **9**, 025 (2020).

[144] A. Jelić and L. F. Cugliandolo, "Quench dynamics of the 2d XY model", Journal of Statistical Mechanics: Theory and Experiment **2011**, P02032 (2011).

[145] K. Nam, W.-B. Baek, B. Kim, and S. J. Lee, "Coarsening of two-dimensional XY model with Hamiltonian dynamics: logarithmically divergent vortex mobility", Journal of Statistical Mechanics: Theory and Experiment **2012**, P11023 (2012).

[146] F. A. Bayocboc, M. J. Davis, and K. V. Kheruntsyan, "Dynamics of thermalization of two tunnel-coupled one-dimensional quasicondensates", Physical Review A **106**, 023320 (2022).

[147] G. C. Wick, "The Evaluation of the Collision Matrix", Phys. Rev. **80**, 268 (1950).

[148] A. Imambekov, V. Gritsev, and E. Demler, "Mapping of Coulomb gases and sine-Gordon models to statistics of random surfaces", Phys. Rev. A **77**, 063606 (2008).

[149] S. Hofferberth, I. Lesanovsky, T. Schumm, A. Imambekov, V. Gritsev, E. Demler, and J. Schmiedmayer, "Probing Quantum and Thermal Noise in an Interacting Many-Body System", Nature Physics **4**, 489 (2008).

[150] S. P. Rath and W. Zwerger, "Full counting statistics of the interference contrast from independent Bose-Einstein condensates", Phys. Rev. A **82**, 053622 (2010).

[151] M. Gring, M. Kuhnert, T. Langen, T. Kitagawa, B. Rauer, M. Schreitl, I. Mazets, D. A. Smith, E. Demler, and J. Schmiedmayer, "Relaxation and Prethermalization in an Isolated Quantum System", Science **337**, 1318 (2012).

[152] A. Beregi, E. Chang, E. Rydow, F. Essler, C. J. Foot, and S. Sunami, "Probing the Universality of 2D Quantum Gases Beyond the Two-Point Correlations", In preparation (2025).